DESIGN OF A VISION-BASED THREE-AXIS ATTITUDE ESTIMATION ALGORITHM FOR SMALL SATELLITES

A THESIS SUBMITTED TO
THE GRADUATE SCHOOL OF NATURAL AND APPLIED SCIENCES
OF
MIDDLE EAST TECHNICAL UNIVERSITY

BY

MEHMET BURAK GÜZEL

IN PARTIAL FULFILLMENT OF THE REQUIREMENTS
FOR
THE DEGREE OF MASTER OF SCIENCE
IN
AEROSPACE ENGINEERING

FEBRUARY 2021

Approval of the thesis:

DESIGN OF A VISION-BASED THREE-AXIS ATTITUDE ESTIMATION ALGORITHM FOR SMALL SATELLITES

submitted by **MEHMET BURAK GÜZEL** in partial fulfillment of the requirements for the degree of **Master of Science in Aerospace Engineering Department, Middle East Technical University** by,

Prof. Dr. Halil Kalıpçılar
Dean, Graduate School of **Natural and Applied Sciences** _____

Prof. Dr. İsmail Hakkı Tuncer
Head of Department, **Aerospace Engineering** _____

Prof. Dr. Ozan Tekinalp
Supervisor, **Aerospace Engineering, METU** _____

Assist. Prof. Dr. Halil Ersin Söken
Co-supervisor, **Aerospace Engineering, METU** _____

Examining Committee Members:

Prof. Dr. Kemal Leblebicioğlu
Electrical-Electronics Engineering, METU _____

Prof. Dr. Ozan Tekinalp
Aerospace Engineering, METU _____

Assist. Prof. Dr. Halil Ersin Söken
Aerospace Engineering, METU _____

Assist. Prof. Dr. Ali Türker Kutay
Aerospace Engineering, METU _____

Assist. Prof. Dr. Yakup Özkazanç
Electrical-Electronics Engineering, Hacettepe University _____

Date:08.02.2021

I hereby declare that all information in this document has been obtained and presented in accordance with academic rules and ethical conduct. I also declare that, as required by these rules and conduct, I have fully cited and referenced all material and results that are not original to this work.

Name, Surname: Mehmet Burak Güzel

Signature :

ABSTRACT

DESIGN OF A VISION-BASED THREE-AXIS ATTITUDE ESTIMATION ALGORITHM FOR SMALL SATELLITES

Güzel, Mehmet Burak
M.S., Department of Aerospace Engineering
Supervisor: Prof. Dr. Ozan Tekinalp
Co-Supervisor: Assist. Prof. Dr. Halil Ersin Söken

February 2021, 105 pages

Equipment and budget limitations of satellite missions encourages researchers to use on-board equipment for multiple tasks. Camera stands out as an ideal equipment that can be used for multiple purposes in satellites making Earth observation. In this thesis, an attitude estimation algorithm is designed to aid the coarse attitude estimates with the attitude information obtained from Earth images. Attitude information is extracted from Earth images according to perspective geometry laws. This estimated attitude is fed into a multiplicative extended Kalman filter (MEKF). Coarse attitude information is obtained by pre-processing magnetometer and sun sensor measurements within the QUEST algorithm and also used in the measurement update process of the filter to ensure the sustainability of the attitude estimates. The algorithm is tested for a hypothetical nano satellite in different scenarios depending on the availability of Earth images at different times.

Keywords: small satellites, imaging-based attitude estimation, camera, Earth images,

MEKF

ÖZ

KÜÇÜK UYDULARDA GÖRÜŞ TABANLI ÜÇ EKSENLİ YÖNELİM TAHMİN ALGORİTMASININ TASARIMI

Güzel, Mehmet Burak
Yüksek Lisans, Havacılık ve Uzay Mühendisliği Bölümü
Tez Yöneticisi: Prof. Dr. Ozan Tekinalp
Ortak Tez Yöneticisi: Dr. Öğr. Üyesi. Halil Ersin Söken

Şubat 2021 , 105 sayfa

Küçük uydu görevleri için alan, ekipman ve bütçe sınırlamaları, araştırmacıları birçok görev için uydu üzerinde halihazırda bulunmakta olan ekipmanı kullanmaya teşvik eder. Kamera, yer gözlemi yapan uydularda çok amaçlı kullanılabilecek bir ekipman olarak öne çıkar. Bu tezde, Dünya görüntülerinden elde edilen yönelim bilgileriyle kaba yönelim tahminlerinin desteklendiği bir yönelim tahmin algoritması tasarlanmıştır. Yönelim bilgisi, Dünya görüntülerinden perspektif geometrisi kuralları kullanılarak çıkartılır. Tahmin edilen yönelim bilgisi, çarpımsal genişletilmiş Kalman filtresine (ÇGKF) beslenir. Kaba yönelim bilgisi QUEST algoritması içinde manyetometre ve güneş sensörü ölçümlerinin ön işlemden geçirilmesiyle elde edilir ve ayrıca yönelim tahminlerinin sürdürülebilirliğini sağlamak için filtrenin ölçüm güncelleme işleminde kullanılır. Algoritma, farklı zamanlarda Dünya görüntülerinin kullanılabilirliğine bağlı olarak farklı senaryolarda test edilmektedir.

Anahtar Kelimeler: küçük uydular, görüntü tabanlı yönelim tahmini, kamera, ÇGKF

To my family.

ACKNOWLEDGMENTS

First of all, I would like to express my deepest gratitude to my advisor, Dr. Halil Ersin Söken, for his support, patience and guidance. He always encouraged me when I was pessimistic, and his door was always open to me. He is a great role model for me with his academic and personal life. I also would like to thank Prof. Dr. Ozan Tekinalp for sharing his valuable knowledge with me. I am thankful to the rest of thesis committee for their insightful questions and comments which encourage me to expand my thesis research from various perspectives.

I sincerely thank to all my colleagues, who makes METU Aerospace Department a peaceful place to work, for their academic support. I especially would like to thank Serhat Onur Çakmak, Harun Levent Şahin and my roommate Battal Gencer for making this difficult time fun with their friendship.

I am grateful to all my friends who always supports me and makes my life easier. But I am especially grateful to Hüseyin Kafalı, Mehmet Can İşeri, Gökhan Soydemir, Mustafa Demircan, Rasim Eriş and Mert Boz who have been my friends since high school and who are now like my family, for standing by me throughout all these times. Life becomes more livable with our fun conversations and friendship.

I must signify that, I am grateful to my precious family, who always believe in me, for their support in every stage of my life with their endless love. I feel blessed with being their son and brother. My beloved mother, whose presence I always feel by my side, has contributed at least as much as me to all the success that I have achieved. I send my love to my nephew Demir Uraz, who is the new member of our family, for making our life cheerful with his smiles.

Lastly but most importantly, I would like to express my deepest thanks to my wife Gönül for her patience, support, and love. The road to gain M.S. degree has many ups and downs. She was always there to keep me on my feet in difficult times.

TABLE OF CONTENTS

LIST OF TABLES

TABLES

LIST OF FIGURES

FIGURES

LIST OF ABBREVIATIONS

ABBREVIATIONS

MEKF	Multiplicative Extended Kalman Filter
QUEST	Quaternion Estimation
EKF	Extended Kalman Filter
UKF	Unscented Kalman Filter
FOV	Field of View
LEO	Low Earth Orbit
DCM	Direction Cosine Matrix
2D	2 Dimensional
3D	3 Dimensional
ECI	Earth-Centered inertial
ECEF	Earth-Centered Earth fixed
LLF	Local-Level Frame
ENU	East North Up
NED	North East Down
IGRF	International Geomagnetic Reference Field
CCD	Charge Coupled Device
RLG	Ring Laser Gyroscopes
FOG	Fiber Obtic Gyroscopes
HRG	Hemispherical Resonator Gyroscope
MEMS	Micro-Electromechanical Systems
SVD	Singular Value Decomposition
KF	Kalman Filters
DEFM	Direct Ellipse Fitting Method

GEFM	Guaranteed Ellipse Fitting Method

CHAPTER 1

INTRODUCTION

1.1 Motivation of Thesis

The number of small satellites in orbit is rapidly increasing due to their short production time, ability to launch multiple of them together, mass production capability, low cost and low financial risk of small satellite missions [1]. Mission of small satellites varies, from Earth observation, atmospheric research, education to technology demonstration. Despite the fact that each satellite is launched for different purposes, accurate attitude determination has vital importance for all missions. While small satellites have many advantages; size, mass, and power limitations prevent designers from using several sensors or actuators on small satellites. As a result, sensors and actuators with multiple functions attract many researchers' interest. In this vein, using any of the mission payloads for different functions has become an active research topic.

Due to the rapid development in imaging technology, high resolution pictures can now be taken with small cameras. Moreover, current microprocessor technology enables us to perform edge detection and image processing like rather computationally heavy tasks in real time. Both volume and mass are saved provided that the camera, which should be present at almost all Earth observing satellites, is used for attitude determination. Furthermore, a significant budget may also be saved by using an Earth observation camera in place of a star tracker. In case the camera operates as an attitude sensor, apart from the traditional attitude sensors (e.g. magnetometers, Sun sensors), different celestial objects can be retrieved as reference for attitude determination, such as stars and Sun.

Main problem for image-based attitude determination, no matter which celestial object is retrieved as reference, is that attitude cannot be determined continuously. Frequency of the camera measurements is pretty low that only few measurements can be gathered per orbital period. This is also because of the fact that main task of the camera in such mission is observation and it cannot be used for attitude estimation all the time. Therefore, spacecraft should continue most of its in orbit operation with coarse attitude measurements or without attitude information at all.

In this thesis, an integrated attitude filtering algorithm is proposed where Earth image-based measurements and coarse attitude measurements are used together to estimate the fine attitude throughout the entire period of the orbit. The algorithm is tested in different scenarios that Earth image-based attitude measurements are gathered for few times per orbital period. Besides, vision-based attitude determination measurements are assumed to be provided continuously in the last scenario. However, the satellite needs to have an additional camera for this scenario since satellites camera has other duties such as Earth observation. Image-based attitude measurements are integrated with coarse attitude measurements in a MEKF designed for attitude estimation. At the measurement update process of the filter, attitude measurements obtained by camera are used whenever they are available; for the rest coarse attitude measurements are used. Coarse attitude is obtained by pre-processing magnetometer and Sun sensor measurements in a QUEST algorithm block. For the time update step of the filter, a gyroscope-based propagation scheme is implemented and angular velocity measurements by the gyroscopes are used for attitude propagation, once they are corrected with the estimated bias. Corrective effect of image-based measurements are visualised in simulations with a hypothetical small satellite.

1.2 Literature Review

Jensen van Vuuren [2] conducted a study on 42 small satellites, and his study showed that 90% of the satellites had a magnetometer on-board and this number was 80% for Sun sensors, 40% for gyroscopes, 35% for star trackers and 10% for Earth sensors. Clearly using rather bulky sensors as star tracker and Earth sensor is not that popular in small satellite missions. Vision based attitude determination helps us to get rid of

using some of those sensors on satellite. Therefore, different types of vision based attitude determination studies are found in the literature.

1.2.1 On-board Attitude Determination Systems

Attitude determination system of Radio Aurora Explorer satellite has mainly three components; magnetometers, Sun sensors(photodides) and rate gyroscopes [3]. Measurements of these sensors are processed in MEKF to estimate attitude. This low cost system provides accurate enough estimations to succeed mission of studying space weather. ESTCube-1 satellite's attitude determination system contains same sensors, however UKF is the estimation algorithm [4]. ESTCube-1 has also a image based attitude determination system which uses on-board camera. This system estimates the orientation by taking into account the points in the image coordinate system and their equivalents in the geographic coordinate system. Difference between attitude determination system and image-based attitude is less than 1.7° and meets with the requirements of mission. UWE-3 is a small satellite launched to test attitude determination and control techniques on orbit [5]. Results indicate that at high spin rates a low cost Sun sensor can not provide correct measurements. Nakasuka et al [6] discuss on attitude determination and control system of 5 small satellites. Advices, about designing such systems, to inexperienced researchers are given in the study.

1.2.2 Vision Based Attitude Determination

Detecting 2-axis nadir direction first and determining 3-axis attitude by using land pattern matching after that is suggested as a method for incorporating the information from Earth images for attitude estimation in [7]. Angular velocity estimation is another concern of this research. Different features in the taken image such as land, sea, cloud and space are references to determine attitude. Also, a deep learning algorithm is designed for same purposes [8]. The fact of high computational time and low accuracy compared to the star trackers are obstacles to the implementation of these studies. On the other hand, Amartuvshin and Asami [9], Kikuya and Matunaga [10] determined relative attitude by matching image patterns taken at different

times. While the first study propagates the relative attitude with gyroscope measurements in an unscented Kalman filter (UKF), second study feeds relative attitude into a Kalman filter. An image based attitude control algorithm is presented in [11]. Feedback attitude information determined by matching the reference image and actual image gathered by satellite camera. Matching the points between expected image and image taken by the satellite is interest of [12]. In case the weather is cloudy or foggy, matching the features in between the pictures is not possible.Wu [13] proposed an algorithm to determine the attitude by matching points but the reference celestial object is asteroid in their research.

Angular velocity estimation based on stellar movements in the images collected by the satellite camera is another method in this field [14, 15]. Attitude is calculated by the propagation of the estimated angular velocity. Gathering star images and using the camera as a star tracker to determine the attitude is interest of different researches [16, 17]. Kim et al. [17] developed an algorithm to detect angular velocity from star observations, made by the camera, instead of star trackers and used this angular velocity in extended Kalman filter (EKF). Angular velocity estimations improved the accuracy of coarse attitude determined by Sun sensor and magnetometer. Although camera aided estimations are better for all three studies, in practice it is hard to get continuous measurements from images taken by camera, unless it is solely used for this purpose.

Modenini et al. [18, 19] presented an image based attitude sensor, however experimental results in this study shows although the proposed method can determine roll and pitch angles pretty accurately, it cannot estimate the yaw angle with same accuracy especially for high latitudes. Since sensor is designed with three different cameras because of the low field of view (FOV) of cameras, this system also violates the area and budget limitations of image-based attitude determination methods. Shimmin [20] tried to determine the attitude with a smart phone camera, but the results show that the method is far from providing accurate attitude estimates.

Small satellites are mostly launched to low Earth orbit (LEO). So that, camera based attitude determination needs cameras with large FOV. An infra-red Earth sensor with large FOV, which provides direction vector to the Earth center, is proposed but this

sensor provides only 2-axis attitude [21].

1.3 Main Contributions of the Thesis

The contributions of this thesis to literature may be summarized as:

- Design of a vision based attitude determination algorithm which is able to provide attitude measurements few times in per orbital period.
- Designing a novel attitude estimation filter that combines vision based attitude determination algorithm (obtained by using on-board camera of a small satellite), coarse attitude measurements (determined by using magnetometer and Sun sensor measurements in a QUEST algorithm) and gyroscope measurements utilized to propagate attitude.

1.4 The Outline of the Thesis

Chapter 1 is consist of thesis's motivation and literature review.

In Chapter 2, attitude representations are discussed. Some useful reference frames and transformation between them are introduced. Geometric concepts are presented that make this thesis easier to understand.

In Chapter 3, sensors which are used to determine attitude on satellites are given with details. Attitude determination methods and equations are mentioned.

In Chapter 4, an integrated attitude determination algorithm is proposed. Edge detection and ellipse fitting subjects are explained in detail. Determining the attitude of spacecraft by using image of a known ellipsoid is studied. The integration of the obtained attitude and coarse attitude in MEKF is explained together with the equations.

In Chapter 5, demonstration of the proposed algorithm with a hypothetical satellite is presented. Results of the four different scenarios are given and discussed.

In Chapter 6, conclusion and future work of the study may be found.

CHAPTER 2

ATTITUDE REPRESENTATIONS, REFERENCE FRAMES AND GEOMETRIC CONCEPTS

The purpose of this chapter is to provide an introduction to attitude representations, reference frames and geometric concepts in order to form a basis for the main algorithms introduced in the next chapters. This chapter begins with a discussion on attitude representations in Section 2.1. This section consists of well known representations of attitude such as direction cosine matrices, Euler angles and quaternions. Giving a brief introduction to especially Euler angles and quaternions will help one to understand what is done in Chapter 4.

The geometry of reference frames are given in Section 2.2. It is fundamental to understand this geometry to conceive the attitude in 3D space. Transformation between these reference frames is discussed in Section 2.3. Transformation in between the frames in relation with the attitude described as well.

In Section 2.4 main geometric concepts that are used in this thesis are introduced. These concepts will greatly assist readers in understanding the vision-based attitude determination algorithm proposed in Section 4.1.3.

2.1 Attitude Representations

Attitude refers to the relationship between two different coordinate frames. In case we are talking about attitude of satellites, the attitude expresses the relationship between the selected reference frame (i.e. Earth centred inertial frame) and the satellite body coordinate frame. There are different methods to express the attitude such as direction

cosine matrix, Euler angles and quaternions. [22, 23].

2.1.1 Direction Cosine Matrix

Let's define a reference frame *A* which has orthogonal unit vectors $\{\vec{\mathbf{a}}_x, \vec{\mathbf{a}}_y, \vec{\mathbf{a}}_z\}$ and another reference frame *B* which has orthogonal unit vectors $\{\vec{\mathbf{b}}_x, \vec{\mathbf{b}}_y, \vec{\mathbf{b}}_z\}$. To write basis vectors $\{\vec{\mathbf{b}}_x, \vec{\mathbf{b}}_y, \vec{\mathbf{b}}_z\}$ in terms of basis vectors $\{\vec{\mathbf{a}}_x, \vec{\mathbf{a}}_y, \vec{\mathbf{a}}_z\}$, following equation is used:

$$\begin{bmatrix} \vec{\mathbf{b}}_x \\ \vec{\mathbf{b}}_y \\ \vec{\mathbf{b}}_z \end{bmatrix} = \begin{bmatrix} \vec{\mathbf{b}}_x \\ \vec{\mathbf{b}}_y \\ \vec{\mathbf{b}}_z \end{bmatrix} \begin{bmatrix} \vec{\mathbf{a}}_x & \vec{\mathbf{a}}_y & \vec{\mathbf{a}}_z \end{bmatrix} \begin{bmatrix} \vec{\mathbf{a}}_x \\ \vec{\mathbf{a}}_y \\ \vec{\mathbf{a}}_z \end{bmatrix} \tag{2.1}$$

$$\begin{bmatrix} \vec{\mathbf{b}}_x \\ \vec{\mathbf{b}}_y \\ \vec{\mathbf{b}}_z \end{bmatrix} = \underbrace{\begin{bmatrix} \vec{\mathbf{b}}_x\vec{\mathbf{a}}_x & \vec{\mathbf{b}}_x\vec{\mathbf{a}}_y & \vec{\mathbf{b}}_x\vec{\mathbf{a}}_z \\ \vec{\mathbf{b}}_y\vec{\mathbf{a}}_x & \vec{\mathbf{b}}_y\vec{\mathbf{a}}_y & \vec{\mathbf{b}}_y\vec{\mathbf{a}}_z \\ \vec{\mathbf{b}}_z\vec{\mathbf{a}}_x & \vec{\mathbf{b}}_z\vec{\mathbf{a}}_y & \vec{\mathbf{b}}_z\vec{\mathbf{a}}_z \end{bmatrix}}_{C} \begin{bmatrix} \vec{\mathbf{a}}_x \\ \vec{\mathbf{a}}_y \\ \vec{\mathbf{a}}_z \end{bmatrix} \tag{2.2}$$

where $\vec{\mathbf{b}}_x\vec{\mathbf{a}}_x = |\vec{\mathbf{b}}_x| \cdot |\vec{\mathbf{a}}_x| \cos\theta$ and *C* is the DCM. Since vectors $\{\vec{\mathbf{a}}_x, \vec{\mathbf{a}}_y, \vec{\mathbf{a}}_z\}$ and $\{\vec{\mathbf{b}}_x, \vec{\mathbf{b}}_y, \vec{\mathbf{b}}_z\}$ are unit vectors, multiplication of their norms is equal to 1. So that, each element of the matrix *C* actually represents cosine of angle between related vectors. Eq. (2.2) can be written in matrix notation:

$$\begin{bmatrix} \vec{\mathbf{b}}_x \\ \vec{\mathbf{b}}_y \\ \vec{\mathbf{b}}_z \end{bmatrix} = \begin{bmatrix} C_{11} & C_{12} & C_{13} \\ C_{21} & C_{22} & C_{23} \\ C_{31} & C_{32} & C_{33} \end{bmatrix} \begin{bmatrix} \vec{\mathbf{a}}_x \\ \vec{\mathbf{a}}_y \\ \vec{\mathbf{a}}_z \end{bmatrix} = C_{BA} \begin{bmatrix} \vec{\mathbf{a}}_x \\ \vec{\mathbf{a}}_y \\ \vec{\mathbf{a}}_z \end{bmatrix} \tag{2.3}$$

One may find in literature that matrix C_{BA} is also called as coordinate transformation matrix and rotation matrix. C_{BA} is an orthogonal matrix that means its inverse equals to its transpose:

$$C_{BA}^{-1} = C_{BA}^{T} \tag{2.4}$$

In order to transform a vector which is defined in frame A to frame B, a successive rotation sequence about x,y and z axes may be followed as shown:

$$C_x(\theta_x) = \begin{bmatrix} 1 & 0 & 0 \\ 0 & \cos\theta_x & \sin\theta_x \\ 0 & -\sin\theta_x & \cos\theta_x \end{bmatrix} \tag{2.5a}$$

$$C_y(\theta_y) = \begin{bmatrix} \cos\theta_y & 0 & -\sin\theta_y \\ 0 & 1 & 0 \\ \sin\theta_y & 0 & \cos\theta_y \end{bmatrix} \tag{2.5b}$$

$$C_z(\theta_z) = \begin{bmatrix} \cos\theta_z & \sin\theta_z & 0 \\ -\sin\theta_z & \cos\theta_z & 0 \\ 0 & 0 & 1 \end{bmatrix} \tag{2.5c}$$

where C_x, C_y and C_z are direction cosine matrix of rotation around x,y and z axis respectively, while θ_x, θ_y and θ_z are rotation angles for the corresponding angles.

2.1.2 Euler Angles

As mentioned in the previous section, in order to transform a vector from one frame to another, successive three rotations are needed. Depending to frames' orientation one or two rotations may be enough as well. Consider the worst scenario that three rotations are required. Any axis can be chosen to rotate around first. The second rotation must be around one of the other two axis. The third rotation may be around the either the first axis or around the other not used third axis. Three different angles used to rotate around each axis are called Euler angles. There are 12 different sets of Euler angles depending on the sequence of rotation used. Resulting rotation matrix of each sequence is different than the other rotation matrices [24].

Let's call back reference frames A and B defined in previous section. Suppose three rotations are required to transform a vector from frame A to frame B. 3-2-1 sequence is chosen in 12 different sequences to carry out this process. The leftmost number denotes the first rotation axis while rightmost represents the last rotation axis. Trans-

formation is completed depending on chosen sequence as:

$$C_3(\theta_3) : A \rightarrow A' \tag{2.6a}$$

$$C_2(\theta_2) : A' \rightarrow A'' \tag{2.6b}$$

$$C_1(\theta_1) : A'' \rightarrow B \tag{2.6c}$$

$$\begin{bmatrix} \vec{\mathbf{a}}_1' \\ \vec{\mathbf{a}}_2' \\ \vec{\mathbf{a}}_3' \end{bmatrix} = \begin{bmatrix} \cos\theta_3 & \sin\theta_3 & 0 \\ -\sin\theta_3 & \cos\theta_3 & 0 \\ 0 & 0 & 1 \end{bmatrix} \begin{bmatrix} \vec{\mathbf{a}}_1 \\ \vec{\mathbf{a}}_2 \\ \vec{\mathbf{a}}_3 \end{bmatrix} = C_3(\theta_3) \begin{bmatrix} \vec{\mathbf{a}}_1 \\ \vec{\mathbf{a}}_2 \\ \vec{\mathbf{a}}_3 \end{bmatrix} \tag{2.7a}$$

$$\begin{bmatrix} \vec{\mathbf{a}}_1'' \\ \vec{\mathbf{a}}_2'' \\ \vec{\mathbf{a}}_3'' \end{bmatrix} = \begin{bmatrix} \cos\theta_2 & 0 & -\sin\theta_2 \\ 0 & 1 & 0 \\ \sin\theta_2 & 0 & \cos\theta_2 \end{bmatrix} \begin{bmatrix} \vec{\mathbf{a}}_1' \\ \vec{\mathbf{a}}_2' \\ \vec{\mathbf{a}}_3' \end{bmatrix} = C_2(\theta_2) \begin{bmatrix} \vec{\mathbf{a}}_1' \\ \vec{\mathbf{a}}_2' \\ \vec{\mathbf{a}}_3' \end{bmatrix} \tag{2.7b}$$

$$\begin{bmatrix} \vec{\mathbf{b}}_1 \\ \vec{\mathbf{b}}_2 \\ \vec{\mathbf{b}}_3 \end{bmatrix} = \begin{bmatrix} 1 & 0 & 0 \\ 0 & \cos\theta_1 & \sin\theta_1 \\ 0 & -\sin\theta_1 & \cos\theta_1 \end{bmatrix} \begin{bmatrix} \vec{\mathbf{a}}_1'' \\ \vec{\mathbf{a}}_2'' \\ \vec{\mathbf{a}}_3'' \end{bmatrix} = C_2(\theta_2) \begin{bmatrix} \vec{\mathbf{a}}_1'' \\ \vec{\mathbf{a}}_2'' \\ \vec{\mathbf{a}}_3'' \end{bmatrix} \tag{2.7c}$$

where A', A'' are intermediate frames and θ_1, θ_2 and θ_3 are Euler angles. The direction cosine matrix of B with respect to A, defined in previous section, is written as:

$$C_{BA} = C_1(\theta_1)C_2(\theta_2)C_3(\theta_3) \tag{2.8}$$

$$C_{BA} = \begin{bmatrix} c\theta_2 c\theta_3 & c\theta_2 s\theta_3 & -s\theta_2 \\ s\theta_1 s\theta_2 c\theta_3 - c\theta_1 s\theta_3 & s\theta_1 s\theta_2 s\theta_3 + c\theta_1 c\theta_3 & c\theta_2 s\theta_1 \\ c\theta_1 s\theta_2 c\theta_3 + s\theta_1 s\theta_3 & c\theta_1 s\theta_2 s\theta_3 - s\theta_1 c\theta_3 & c\theta_1 c\theta_2 \end{bmatrix} \tag{2.9}$$

where $c\theta$ and $s\theta$ refers to $\cos\theta$ and $\sin\theta$ respectively. Small angle theorem allows us to redefine Eq. (2.9) as:

$$C_{BA} = \begin{bmatrix} 1 & \theta_3 & -\theta_2 \\ -\theta_3 & 1 & \theta_1 \\ \theta_2 & -\theta_1 & 1 \end{bmatrix} \tag{2.10}$$

Although the 3-dimensional Euler angles are dimensionally smaller than both DCM and quaternions, the singularity limits their applications in practice. Also trigonometric functions break linearity in Euler angles' differential equations. This is another limitation for their real life applications [25].

2.1.3 Quaternions

Euler rotation theorem indicates that a DCM actually rotates a vector around a unit vector $\vec{\mathbf{e}}$ by the angle of ϕ as shown in Figure 2.1. This axis and angle are called as Euler axis and Euler angle respectively. The unit vector $\vec{\mathbf{e}}$ is formulated with help of two reference frames defined in previous section:

$$\begin{aligned} \vec{\mathbf{e}} &= e_1\vec{\mathbf{a}}_1 + e_2\vec{\mathbf{a}}_2 + e_3\vec{\mathbf{a}}_3 \\ \vec{\mathbf{e}} &= e_1\vec{\mathbf{b}}_1 + e_2\vec{\mathbf{b}}_2 + e_3\vec{\mathbf{b}}_3 \end{aligned} \tag{2.11}$$

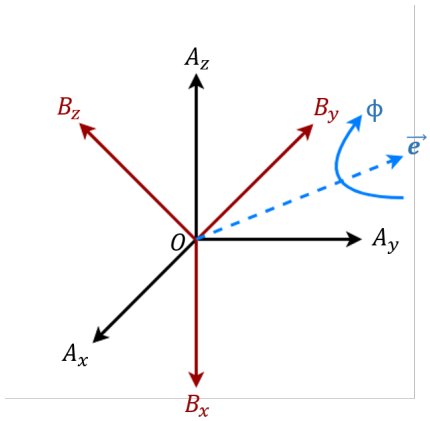

Figure 2.1: Euler axis and Euler angle

Quaternions have similarities with Euler axis and Euler angle definition of rotation. The idea behind quaternions is that transformation between reference frames may be done with a single rotation around the vector $\vec{\mathbf{e}}$ with a rotation of angle ϕ. Quaternions

has four elements that three of them form a vector and other one is a scalar:

$$q_1 = e_1 \sin(\phi/2) \tag{2.12a}$$

$$q_2 = e_2 \sin(\phi/2) \tag{2.12b}$$

$$q_3 = e_3 \sin(\phi/2) \tag{2.12c}$$

$$q_4 = \cos(\phi/2) \tag{2.12d}$$

Since $\vec{\mathbf{e}}$ is a vector, first three terms of quaternion may be defined as vector as well. These equations imply as well that the norm of quaternions must be equal to 1 ($q_1^2 + q_2^2 + q_3^2 + q_4^2 = 1$). In order to provide notational simplicity quaternions will be defined as follows:

$$\bar{\mathbf{q}} = \begin{bmatrix} \vec{\mathbf{q}} \\ q_4 \end{bmatrix} \quad \text{where} \quad \vec{\mathbf{q}} = \begin{bmatrix} q_1 \\ q_2 \\ q_3 \end{bmatrix} \tag{2.13}$$

Another way of expressing quaternions is treating them as a complex number with one real element q_4 and three imaginary elements q_1, q_2 and q_3:

$$\bar{\mathbf{q}} = q_4 + q_1 i + q_2 j + q_3 k = q_4 + \vec{\mathbf{q}} \tag{2.14}$$

$$\bar{\mathbf{q}} = \cos(\frac{\phi}{2}) + \vec{\mathbf{e}} \sin(\frac{\phi}{2}) \tag{2.15}$$

where i, j and k obey the rules $i^2 = j^2 = k^2 = -1,\ ij = -ji = k,\ jk = -kj = i,\ ki = -ik = j$. Therefore quaternion multiplication may be expressed as follows:

$$\bar{\mathbf{p}} \otimes \bar{\mathbf{q}} = (p_4 + \vec{\mathbf{p}}) \otimes (q_4 + \vec{\mathbf{q}}) = (p_4 q_4 - \vec{\mathbf{p}} \cdot \vec{\mathbf{q}}) + (p_4 \vec{\mathbf{q}} + q_4 \vec{\mathbf{p}} + \vec{\mathbf{p}} \times \vec{\mathbf{q}}) \tag{2.16}$$

Although this type of quaternion multiplication is easy to understand mathematically, in attitude analysis the multiplying quaternions with the formulas below are more

useful [23]:

$$\bar{\mathbf{p}} \otimes \bar{\mathbf{q}} = \begin{bmatrix} q_4\vec{\mathbf{p}} + p_4\vec{\mathbf{q}} - \vec{\mathbf{p}} \times \vec{\mathbf{q}} \\ p_4 q_4 - \vec{\mathbf{p}} \cdot \vec{\mathbf{q}} \end{bmatrix} \tag{2.17a}$$

$$\bar{\mathbf{p}} \odot \bar{\mathbf{q}} = \begin{bmatrix} q_4\vec{\mathbf{p}} + p_4\vec{\mathbf{q}} + \vec{\mathbf{p}} \times \vec{\mathbf{q}} \\ p_4 q_4 - \vec{\mathbf{p}} \cdot \vec{\mathbf{q}} \end{bmatrix} \tag{2.17b}$$

$$\bar{\mathbf{p}} \otimes \bar{\mathbf{q}} = \bar{\mathbf{q}} \odot \bar{\mathbf{p}} \tag{2.17c}$$

Similar to DCM, the multiplication of quaternions represents sequential rotations. Assume $\bar{\mathbf{p}} = \cos(\frac{\beta}{2}) + \hat{\mathbf{e}}\sin(\frac{\beta}{2})$ and $\bar{\mathbf{q}} = \cos(\frac{\alpha}{2}) + \hat{\mathbf{e}}\sin(\frac{\alpha}{2})$ where $\hat{\mathbf{e}}$ is the unit length rotational axis, β and α are the rotational angles:

$$\begin{aligned} \bar{\mathbf{r}} = \bar{\mathbf{p}} \otimes \bar{\mathbf{q}} &= \left(\cos\left(\frac{\beta}{2}\right) + \hat{\mathbf{e}}\sin\left(\frac{\beta}{2}\right)\right) \otimes \left(\cos\left(\frac{\alpha}{2}\right) + \hat{\mathbf{e}}\sin\left(\frac{\alpha}{2}\right)\right) \\ \bar{\mathbf{r}} &= \left(\cos\left(\frac{\beta+\alpha}{2}\right) + \hat{\mathbf{e}}\sin\left(\frac{\beta+\alpha}{2}\right)\right) \end{aligned} \tag{2.18}$$

Therefore two sequential rotations are represented as product of two quaternions. Furthermore, it is necessary to define the product of a vector and quaternion to be able to apply these rotations to the vector [26]. A vector may be expressed as a pure quaternion in which the vector part is $\vec{\mathbf{v}}$ and scalar element is zero ($\bar{\mathbf{v}} = \vec{\mathbf{v}} + 0$). Multiplication of a quaternion with a vector is given as:

$$\bar{\mathbf{q}} \otimes \bar{\mathbf{v}} = (q_4 + \vec{\mathbf{q}}) \otimes (0 + \vec{\mathbf{v}}) = -\vec{\mathbf{q}} \cdot \vec{\mathbf{v}} + q_4\vec{\mathbf{v}} + \vec{\mathbf{q}} \times \vec{\mathbf{v}}) \tag{2.19}$$

A quaternion is expected to rotate a vector $\bar{\mathbf{v}}$ into another vector $\bar{\mathbf{w}}$ which is also a pure quaternion. Neither $\bar{\mathbf{w}} = \bar{\mathbf{q}} \otimes \bar{\mathbf{v}}$, nor $\bar{\mathbf{w}} = \bar{\mathbf{v}} \otimes \bar{\mathbf{q}}$ yields a pure quaternion. Since the rotated vector needs to be expressed as a pure quaternion, following equation is used to rotate a vector with quaternions:

$$\bar{\mathbf{w}} = \bar{\mathbf{q}} \otimes \bar{\mathbf{v}} \otimes \bar{\mathbf{q}}^* \tag{2.20}$$

where $\bar{\mathbf{q}}^*$ is complex conjugate and also inverse of a quaternion which is equal to:

$$\bar{\mathbf{q}}^* = \bar{\mathbf{q}}^{-1} = -\vec{\mathbf{q}} + q_4 = -q_1 i - q_2 j - q_3 k + q_4 \tag{2.21}$$

The DCM can be written in terms of quaternions as:

$$C_{BA} = \begin{bmatrix} 1 - 2(q_2^2 + q_3^2) & 2(q_1 q_2 + q_3 q_4) & 2(q_1 q_3 - q_2 q_4) \\ 2(q_2 q_1 - q_3 q_4) & 1 - 2(q_1^1 + q_3^2) & 2(q_2 q_3 + q_1 q_4) \\ 2(q_3 q_1 + q_2 q_4) & 2(q_3 q_2 - q_1 q_4) & 1 - 2(q_1^2 + q_2^2) \end{bmatrix} \tag{2.22}$$

Similarly, the reverse of this operation, that is, converting from DCM C_{BA} to quaternion $\bar{\mathbf{q}}$ can also be written as:

$$q_4 = \frac{1}{2}\left(1 + C_{11} + C_{22} + C_{33}\right)^{\frac{1}{2}} \quad \text{for} \quad 0 \leq \phi \leq \pi \tag{2.23}$$

$$\vec{\mathbf{q}} = \frac{1}{4q_4} \begin{bmatrix} C_{23} - C_{32} \\ C_{31} - C_{13} \\ C_{12} - C_{21} \end{bmatrix} \quad \text{if} \quad q_4 \neq 0 \tag{2.24}$$

One needs to know quaternion kinematics to know how the quaternions vary in time. This is an information we use as a part of attitude filter design. Also, angular velocity $\vec{\boldsymbol{\omega}}$ is required to be taken into account during propagation. Kinematic differential equation of quaternion is given as follows:

$$\dot{q}_4 = -\frac{1}{2}\vec{\boldsymbol{\omega}}^T \vec{\mathbf{q}} \tag{2.25a}$$

$$\dot{\vec{\mathbf{q}}} = \frac{1}{2}\left(q_4 \vec{\boldsymbol{\omega}} - \vec{\boldsymbol{\omega}} \times \vec{\mathbf{q}}\right) \tag{2.25b}$$

2.2 Reference Frames

Reference frames are used to express the attitude and position of a rigid body with respect to some reference. Some useful reference frames relevant to attitude determi-

nation and transformations in between them are discussed in this section.

2.2.1 Spacecraft Body Frame

The spacecraft body frame is vehicle-carried which means its moving and rotating with the body of the spacecraft. Origin of the frame is at the center of the mass of the spacecraft. Sensors (i.e. gyroscopes, sun sensors, magnetometers) are mounted aligned to the body reference frame during spacecraft assembly [27]. Therefore, measurements of these sensors are resolved in the body frame. The body frame used in this thesis is given in Figure 2.2 and defined as:

- The z-axis is nadir pointing. It is called yaw axis, since the yaw angle represents rotation about this axis according to right hand rule.
- The y-axis points towards up. It is called pitch axis, since the pitch angle represents rotation about this axis according to right hand rule.
- The x-axis completes orthogonal frame which is defined right handed. It is called roll axis, since the roll angle represents rotation about this axis according to right hand rule.
- Origin of the spacecraft body frame coincides with center of gravity of the spacecraft.

2.2.2 Earth Centered Inertial Frame

A frame which is not moving or is moving with constant velocity without rotation is called as inertial frame. Sensors produce measurements with respect to these inertial frames. Newton's laws are only able to be used in inertial frames. The Earth centered inertial(ECI) frame is the reference frame for near-Earth applications. ECI frame is shown in Figure 2.3 with X_I, Y_I, Z_I axes and defined as:

- The z-axis points toward the Earth's north pole.

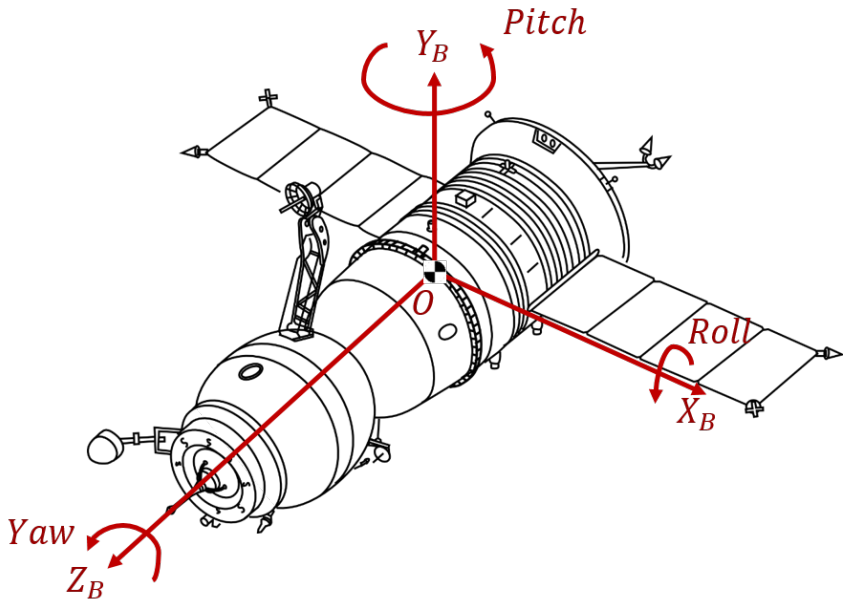

Figure 2.2: Spacecraft body frame

- The x-axis is through the vernal equinox.
- The y-axis completes orthogonal frame which is defined right handed.
- Origin of the ECI frame coincides with center of mass of the Earth.

2.2.3 Earth Centered Earth Fixed Frame

Although Earth centered Earth fixed (ECEF) frame has same origin and z-axis with ECI frame, it rotates with the Earth and has angular velocity $\vec{\omega}_E$. in other words, $\vec{\omega}_E$ is the angular velocity of the Earth with respect to ECI resolved in ECEF. X_E, Y_E, Z_E axes represents ECEF in Figure (2.3):

- The z-axis points in the direction of the Earth's north pole.
- The x-axis points through the intersection of Greenwich meridian and equator plane.
- The y-axis completes the defined right handed system.
- Origin of the ECEF frame coincides with center of mass of the Earth.

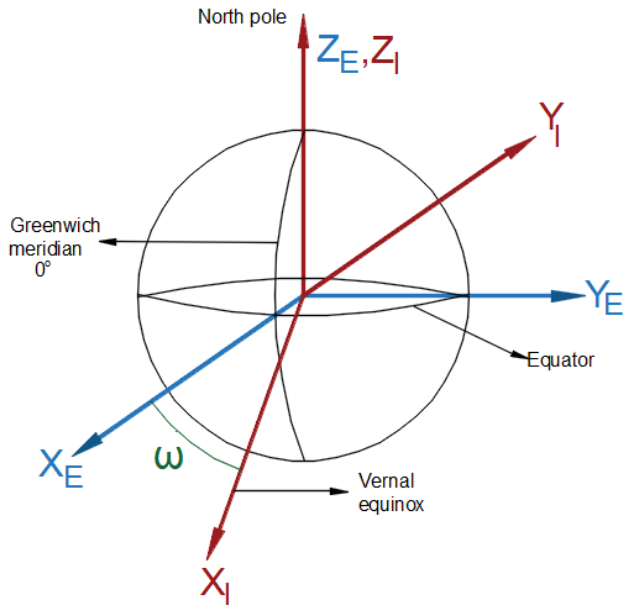

Figure 2.3: Earth centered inertial frame and Earth centered Earth fixed frame

2.2.4 Orbital (Local Vertical - Local Horizontal) Frame

Orbital frame is another reference frame considered moves with the spacecraft on the orbit of spacecraft. In some cases (especially for nadir pointing satellites) attitude may be defined with respect to orbital frame. Orbital frames' origin is located at the mass center of the satellite as shown in Figure 2.4.

- The z-axis points towards nadir direction parallel to the position vector of satellite.
- The y-axis is tangential to the orbit. This fact implies that is aligned with the velocity vector of the satellite in case the satellite is on a circular orbit.
- The x-axis completes the defined right handed system.
- Origin of the ECEF frame coincides with center of mass of the Earth.

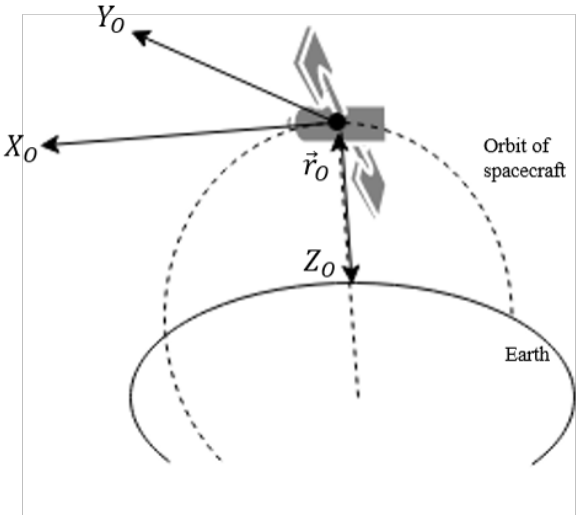

Figure 2.4: Orbital frame

2.3 Reference Frame Transformation

While transforming a vector from one frame of reference to another, DCM, Euler angles or quaternions may be used as mentioned earlier. All these techniques result with a rotation matrix and is expressed as C_{TC} where the first letter of subscript represents target frame and second is the current frame in which the vector is resolved.

2.3.1 ECEF to ECI

In order to transform a vector resolved in ECI frame to ECEF, rotation matrix which is given in Eq. (2.5c) should be used:

$$C_{EI} = \begin{bmatrix} \cos(\theta_{G0}) & \sin(\theta_{G0}) & 0 \\ -\sin(\theta_{G0}) & \cos(\theta_{G0}) & 0 \\ 0 & 0 & 1 \end{bmatrix} \tag{2.26}$$

where θ_{G0} is the Greenwich sidereal time. θ_{G0} is a function of year, month, day, hour, minute and second. Calculation of θ_{G0} may be found at [28], pages 258-261. Owing to rotation matrices are orthogonal, transformation matrix from ECEF to ECI may be found as follows:

$$C_{IE} = C_{EI}^{-1} = C_{EI}^{T} = \begin{bmatrix} \cos(\theta_{G0}) & -\sin(\theta_{G0}) & 0 \\ \sin(\theta_{G0}) & \cos(\theta_{G0}) & 0 \\ 0 & 0 & 1 \end{bmatrix} \tag{2.27}$$

2.3.2 Orbital Frame to ECI

The rotation matrix which transform orbital frame to ECI frame is calculated using position $\vec{\mathbf{r}}_I$ and velocity $\vec{\mathbf{v}}_I$ vector of the satellite expressed in ECI frame:

$$\vec{\mathbf{o_3}} = \frac{\vec{\mathbf{r}}_I}{\|\vec{\mathbf{r}}_I\|} \tag{2.28a}$$

$$\vec{\mathbf{o_2}} = -\frac{\vec{\mathbf{r}}_I \times \vec{\mathbf{v}}_I}{\|\vec{\mathbf{r}}_I \times \vec{\mathbf{v}}_I\|} \tag{2.28b}$$

$$\vec{\mathbf{o_1}} = \vec{\mathbf{o}}_2 \times \vec{\mathbf{o}}_3 \tag{2.28c}$$

$$C_{IO} = \begin{bmatrix} \vec{\mathbf{o_1}} & \vec{\mathbf{o_2}} & \vec{\mathbf{o_3}} \end{bmatrix} \tag{2.28d}$$

2.4 Geometric Concepts

To understand vision based attitude determination given in Section (4.1.3), one should first understand the geometric concepts discussed in this section. The vision based attitude determination method is basically a transformation between frames depending on the rules of perspective geometry. In this context, introducing a few basic geometric concepts will aid the comprehension of future topics.

2.4.1 Camera Frame and Image Frame

Camera frame can be considered the same as the spacecraft body frame. But unlike spacecraft body frame, the camera frame origin is at the focal point of the optical system. An illustration of camera frame is given in Figure 2.5. It is obvious that X_C, Y_C, Z_C represent orthogonal axes of the camera frame. Z_C is aligned with the

principle axis of the optical system. Y_C points upwards and X_C axis completes a right handed orthogonal coordinate system.

Unlike the other frames described thus far, the image frame is a two-dimensional frame. As it is seen in Figure 2.5, X_{Im} and Y_{Im} are two orthogonal axis of the frame. Its X_{Im} axis points to the right and its Y_{Im} axis points down. Its origin is at the upper left corner of the image plane.

2.4.2 Focal Length

Focal length is the distance between origin of the camera frame and image plane and symbolized by f. Focal length is also shown in Figure (2.5). In the same figure, O_P represents principle point on the image plane. Coordinates of this point in image frame are p_x and p_y.

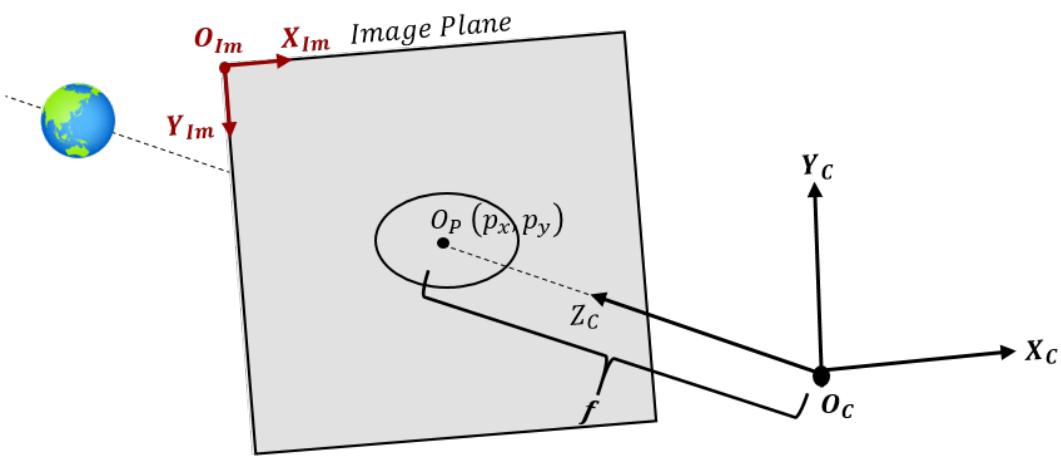

Figure 2.5: Illustration of camera frame and image frame

2.4.3 Basic Pinhole Camera Model

According to pinhole camera model given in Figure 2.6, position vector $\vec{\mathbf{r}}_C$ of a point in space can be mapped to a 2D vector $\vec{\mathbf{r}}_{Im}$ in image plane. This process is defined as

follows [29]:

$$\vec{\mathbf{r}}_C = \{r_{Cx}, r_{Cy}, r_{Cz}\}^T \quad \rightarrow \quad \vec{\mathbf{r}}_{Im} = \{\frac{f r_{Cx}}{r_{Cz}} + p_x, \frac{f r_{Cy}}{r_{Cz}} + p_y\}^T \tag{2.29}$$

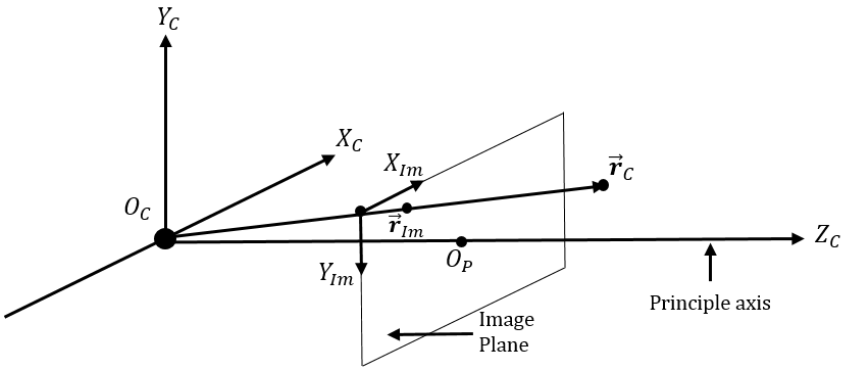

Figure 2.6: Pinhole camera model

This process is actually a linear transformation called central projection mapping from world to image frames. The centre of projection is the origin of the camera frame. Consider that both vectors resolved in camera frame and image frame are expressed with homogeneous coordinates. Transformation from camera frame to image frame is done by using the following equation:

$$\vec{\mathbf{r}}_{Im} = \underbrace{\begin{bmatrix} f & 0 & p_x & 0 \\ 0 & f & p_y & 0 \\ 0 & 0 & 1 & 0 \end{bmatrix}}_{K_{cam}} \begin{bmatrix} r_{Cx} \\ r_{Cy} \\ r_{Cz} \\ 1 \end{bmatrix} \tag{2.30}$$

where K_{cam} is the camera intrinsic matrix. In case the position vector is resolved in ECI frame, then this vector must be transformed to the camera frame first. After that transformation from camera frame to image frame may be done. Let's define a rotation matrix that transforms vectors from ECI frame to camera frame as C_{CI} and position of camera resolved in ECI frame is $\vec{\mathbf{R}}_{cam_I}$. Vector $\vec{\mathbf{r}}_I$ can be transformed

from ECI frame to image frame as follows:

$$\text{ECI to camera frame} \quad \rightarrow \quad \vec{\mathbf{r}}_C = \begin{bmatrix} C_{CI} & -C_{CI}\vec{\mathbf{R}}_{cam_I} \\ 0 & 1 \end{bmatrix} \begin{bmatrix} \vec{\mathbf{r}}_I \\ 1 \end{bmatrix} \tag{2.31}$$

$$\text{Camera frame to image frame} \quad \rightarrow \quad \vec{\mathbf{r}}_{Im} = K_{cam} \begin{bmatrix} \vec{\mathbf{r}}_C \\ 1 \end{bmatrix} \tag{2.32}$$

Substituting Eq. (2.31) into Eq. (2.32) yields:

$$\text{ECI to image frame} \quad \rightarrow \quad \vec{\mathbf{r}}_{Im} = K_{cam} \begin{bmatrix} C_{CI} & -C_{CI}\vec{\mathbf{R}}_{cam_I} \\ 0 & 1 \end{bmatrix} \begin{bmatrix} \vec{\mathbf{r}}_I \\ 1 \end{bmatrix} \tag{2.33}$$

2.4.4 Conics, Quadrics and Their Projection

Conic is a curve in the plane defined by a quadratic (second-degree) equation:

$$ax^2 + bxy + cy^2 + dx + ey + f = 0 \tag{2.34}$$

when homogeneous coordinates ($x \rightarrow x_1/x_3, y \rightarrow x_2/x_3$) substituted in Eq. (2.34):

$$ax_1^2 + bx_1x_2 + cx_2^2 + dx_1x_3 + ex_2x_3 + fx_3^2 = 0 \tag{2.35}$$

The matrix form of Eq. (2.35) may be written as follows:

$$x^T E x = 0 \tag{2.36}$$

where E consists of conic equation's coefficients.

$$E = \begin{bmatrix} a & \frac{b}{2} & \frac{d}{2} \\ \frac{b}{2} & c & \frac{e}{2} \\ \frac{d}{2} & \frac{e}{2} & f \end{bmatrix} \tag{2.37}$$

A conic is non-degenerate in case determinant of matrix E is not equal to zero. A non-degenerate conic may be an ellipse, a parabola or a hyperbola. Degenerate conics are beyond the scope of this study. On the other hand, a quadric is defined as a 3D smooth surface such as sphere, ellipsoid and expressed with this equation:

$$Ax^2 + By^2 + Cz^2 + 2Dyz + 2Fzx + 2Gxy + 2Hx + 2Py + 2Rz + S = 0 \quad (2.38)$$

Again the matrix form of Eq. (2.38) may be written as follows:

$$x^T Q x = 0 \quad (2.39)$$

where matrix Q contains conic equation's coefficients.

$$Q = \begin{bmatrix} A & G & P & H \\ G & B & D & P \\ F & D & C & R \\ H & P & R & S \end{bmatrix} \quad (2.40)$$

Like conics, in case the matrix Q is not singular, quadric is non-degenerate. Dual of the quadric Q^* represents tangent planes to quadric Q, where $Q^* = adjoint(Q)$. $Q^* = Q^{-1}$ when Q is not singular.

Assume a picture is taken of a quadric by a camera. The resulting shape on image plane will be a conic. This conic consists of points where imaginary lines emanating from the origin of the camera frame tangent to the quadric surface. This phenomenon enables the matrix E^* ($E^* = E^{-1}$ when E is not singular) to be calculated from the quadric matrix Q with the help of perspective projection rules:

$$E^* = K_{cam} Q^* K_{cam}^T \quad (2.41)$$

Let's repeat the same projection for a more specific case. Assume a picture is taken of an ellipsoid, which is a quadric, by a camera. The resulting shape on image plane

will be an ellipse, which is a conic. The quadric equation of ellipsoid is given as:

$$\frac{1}{a^2}x^2 + \frac{1}{b^2}y^2 + \frac{1}{c^2}z^2 - 1 = 0 \tag{2.42}$$

Thus, quadric matrix Q will be:

$$Q = \begin{bmatrix} \frac{1}{a^2} & 0 & 0 & 0 \\ 0 & \frac{1}{b^2} & 0 & 0 \\ 0 & 0 & \frac{1}{c^2} & 0 \\ 0 & 0 & 0 & -1 \end{bmatrix} \tag{2.43}$$

where a, b and c are semi axes of the ellipsoid.

CHAPTER 3

ATTITUDE DETERMINATION TOOLS, METHODS AND ESTIMATION FILTERS

This chapter gives a brief information about attitude determination tools, methods and attitude estimation filters. It begins with a discussion on attitude determination tools in Section 3.1. Since magnetometers and Sun sensors are part of the algorithm proposed in this thesis, having sufficient knowledge about these sensors will make the algorithms easier to understand.

In Section 3.2, attitude determination methods are discussed. This section consists of well known attitude determination tools such as TRIAD method, Davenport's Q method, QUEST method and SVD Method. Magnetometer and Sun sensor data are pre-processed in QUEST method to determine coarse attitude which is introduced in Chapter 4. In Section 3.3, first a brief introduction to KF may be found. Next, design of EKF for attitude estimation and MEKF, which was developed to use EKF with quaternions, are explained in detail.

3.1 Attitude Determination Tools

Attitude measurement sensors provide measurements that can be eventually used to determine the attitude of the satellite with respect to a reference frame (i.e ECI frame, LLF). The attitude determination system must contain sufficient number of sensors to ensure that accuracy of the attitude measurement is enough for the mission requirements and to send attitude measurements continuously. The product of attitude determination system may be quaternions, Euler angles or DCM. Attitude sensors are separated in two categories and these two categories of sensors are used to comple-

ment each other [30]:

- **Reference attitude sensors:** Provide 2-axis or 3-axis direction of a celestial object such as the Earth, the Sun or stars. Drawback of such sensors is that they can not provide attitude measurements continuously because of eclipse, interruption or low frequency of the sensor.

- **Inertial attitude sensors:** Apart from reference attitude sensors, these sensors provides change in attitude (i.e angular velocity). They are not effected from eclipse so they can send attitude measurements continuously. Since they measure change in attitude, attitude must be calculated by propagating these measurements. This process causes drifts and attitude error increases with time. Therefore, calibration is required for inertial attitude sensors.

In general attitude determination system includes both reference and inertial attitude sensors. Despite reference attitude sensors are used to calibrate inertial attitude sensors, these sensors are not able to provide measurements continuously in some special cases that are discussed in detail at upcoming sections. Magnetometer is an exception for this statement but their measurements are not accurate as much as other reference sensors. Inertial attitude sensors, on the other hand, can provide measurements to propagate the attitude during those special cases where reference attitude sensors cannot determine the orientation. So, these sensors must cooperate to determine attitude. Attitude estimate filters such as Kalman filter, integrates these two different measurements to provide accurate attitude continuously in orbit. Frequently used attitude determination sensors and their important features are given in Table 3.1 [31]:

Table 3.1: Attitude sensors and their features for small satellites

Sensors	Mass Range [kg]	Output	Accuracy [°]
Sun sensors	0.1 - 2	direction vector of Sun	0.005 - 3
Star trackers	2 - 5	position vectors to different stars	0.0003 - 0.01
Earth sensors	0.5 - 4	direction vector of the Earth center	0.1 - 1
Gyroscopes	1 - 15	angular velocity	0.003 - 1 [°/s]

3.1.1 Sun Sensors

Although they can only measure attitude in 2-axis, one of the most preferred sensors for determining the attitude in satellites is the Sun sensor. There are two reasons of this statement [32]:

1. No planet except the Earth, and star can affect luminosity of the Sun.
2. The Sun is the brightest reference for a satellite orbiting around the Earth. So, it is easy to find a vector pointing towards the Sun.

There are two types of Sun sensors, analog and digital. Despite of their expensiveness, digital Sun sensors gives more accurate measurements compared to analog Sun sensors. However, analog Sun sensors can fulfil requirements of many missions as well.

Analog Solar sensors have a photocell inside and measure the angle between the normal of the photocell and the sunlight entering the sensor as shown in Figure 3.1. Sensor's output is the current that changes depending on that angle and may be found as follows:

$$I(\theta) = I_0 + \cos(\theta) \tag{3.1}$$

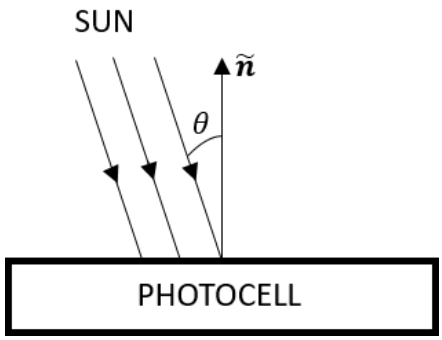

Figure 3.1: Angle between normal of the photocell and rays of Sun

Although the output current is modelled as in Eq. (3.1), when θ is close to $\pm 90°$ the output current does not obey cosine law exactly. Because of this constraint, analog

Sun sensors generally operate between ±85°. That means range of the field of view of sun sensors are 170° at most. A Sun sensor with one photocell can only measure the angle, it can not give any information about the direction of the Sun. In order to determine one-axis direction of the Sun, two photocells must be used. A Sun sensor design with two photocells is shown in Figure 3.2

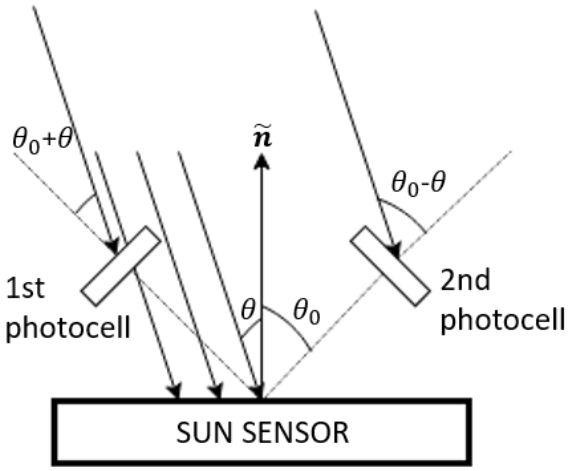

Figure 3.2: Sun sensor with two photocells

Both photocells are placed at an angle θ_0 between the sensor's normal axis $\tilde{\mathbf{n}}$. The sun rays are assumed to come with angle θ with respect to $\tilde{\mathbf{n}}$. Therefore, output current may be found using equation:

$$\begin{aligned} \Delta I = I_2 - I_1 &= K\cos(\theta_0 - \theta) - K\cos(\theta_0 + \theta) \\ &= 2K\sin(\theta_0)\sin(\theta) = C\sin(\theta) \end{aligned} \tag{3.2}$$

where C is a constant depending on properties of photocells. The greater inclination of the Sun (θ) is , the greater measurement error.

To determine the direction of the Sun vector in 2-axis, two single axis Sun sensors are required to be placed perpendicular to each other. Since a single axis Sun sensor has two photocells as mentioned, one sensor with four photocells placed properly can detect direction of the Sun in 2-axis.

Similar to analog Sun sensors, 2-axis digital sun sensors also consist of 2 single axis

digital sun sensors placed perpendicular to each other. But unlike analog sensors, these sensors allow sunlight to pass through the in-line holes on them. A digital signal is created in each detector for the sunlight coming through the holes. These signals are combined to form a gray code. This gray code is solved in a processor to express direction vector of the Sun in body fixed reference frame [32].

3.1.2 Magnetometers

Magnetometers measure direction and magnitude of the magnetic field vector of the Earth in the body reference frame. Thanks to their low weight, low power consumption and low price, they are often preferred in attitude determination systems of small satellites [33]. Also, they can operate during eclipse while Sun sensor can not. Nevertheless magnetometer can only provide 2-axis attitude at an instant, thus attitude determinations systems need another additional sensor to determine 3-axis attitude of the satellite. One other handicap of the magnetometers is that they can only provide measurements in LEO as the magnitude of the Earth's magnetic field decreases with the cube of the distance.

Attitude determination methods, which will be introduced in Section 3.2, need the same vector resolved in both the body reference frame and the ECI frame to determine attitude of body frame with respect to ECI frame. Magnetometers can measure the direction of Earth's magnetic field vector only in body reference frame. Hence, the same vector resolved in ECI frame must be known to determine attitude. The magnetic field vector in ECI frame corresponding to the position of the satellite can be found using International Geomagnetic Reference Field (IGRF) model. This model must be updated every 5 years due to change on Earth's magnetic field. The latest version of the magnetic field map of the Earth is generated in 2020 [34]. As well as the inherent sensor errors, the errors in the modelled magnetic field, which may introduce errors up to 0.5° to the estimated attitude, makes using magnetic field as the reference for attitude estimation a rather coarse method. Magnetometer measurement model is defined as follows [35]:

$$\vec{\mathbf{B}}_B = C_{BI}\vec{\mathbf{B}}_I + \vec{\mathbf{b}} + \vec{\boldsymbol{\nu}} \tag{3.3}$$

where $\vec{\mathbf{B}}_B$ is the magnetometer measurement in body frame, C_{BI} is the rotation matrix from ECI frame to body frame. $\vec{\mathbf{B}}_I$ is the direction of the magnetic field vector corresponding to position of the satellite, $\vec{\mathbf{b}}$ is the bias vector and $\vec{\boldsymbol{\nu}}$ is the Gaussian zero-mean measurement noise. Magnetometers are required to be calibrated to minimize the effects of bias and other possible errors such as scaling.

3.1.3 Earth Sensors

Earth sensors measure attitude of a satellite with respect to the Earth. There are two types of Earth sensors based on their operating principle:

1. Horizon crossing Earth sensors determines crossing points while Earth's horizon moving in sensor's field of view. Sensor has mechanisms to rotate itself and scan wider areas.
2. Static sensors are on a fixed direction and does not rotate.

Infra-red radiation sensing sensors gives most accurate results for horizon sensing [32]. This is because energy emitted by Earth's surface is much more homogeneous between ranges of infra-red sensors. Thus, Earth's horizon can be detected more consistently. Infra-red sensors basically senses infra-red radiation which is the total thermal radiation of the Earth.

Another important design concern of Earth sensors is defining the shape of the Earth. A model is developed for attitude determination in 1977 [36]. According to this model, shape of the Earth is accepted as an ellipsoid rotating around its minor axis. Earth's mean equatorial radios and polar radios are defined as $R_e = 6,378.14kg$ and $R_p = 6,356.75kg$ respectively. Flattening may be calculated as:

$$f = \frac{R_e - R_p}{R_e} \approx 0.00335281 \tag{3.4}$$

3.1.3.1 Horizon Crossing Earth Sensors

Horizon crossing sensors has four main parts:

- **Scanning mechanism:** A rotating mechanism allows the sensor to expand its angle of view. So that, the sensor can scan wider area.
- **Optical system:** It has a filter that prevents sensor to detect CO_2 out of the range between 14-16 μm and a lens that focuses the Earth image.
- **Radiance detector:** Senses the presence of the Earth in the sensors field of view.
- **Signal processing system:** This electronic box processes signals coming from optical system. Moreover it provides power to the components in the other three parts.

Scanning mechanism of horizon crossing Earth sensors can be adjusted to make single cone scanning or dual cone scanning. In case sensor makes single scanning, altitude of the satellite must be known to determine attitude. For dual scanning case, altitude info is not needed.

Single cone scanning geometry is given in Figure 3.3. Roll and yaw angles for small deviations from the nadir direction is calculated with the help of this geometry. X_B and Y_B are the body axis of the satellite. Scanning mechanism can rotate about Y_B axis. γ represents deflection angle.

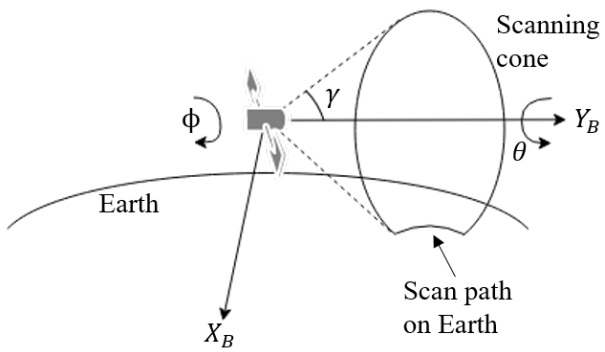

Figure 3.3: Single cone scanning

A vertical reference is fixed to the optical head as shown in Figure 3.4. This reference axis is necessary to calculate the pitch angle. Let's define two phase angles as δ_1 and δ_2 for the scanning cone intersecting with the horizon of the Earth. While the scanning cone starts to enter the Earth atmosphere at point 1, below part of the cone

goes out of the atmosphere at point 2. The phase angle difference between two points is calculated as:

$$E = \delta_2 - \delta_1 \tag{3.5}$$

where E is phase angle difference between two points and it depends on the altitude of the satellite and the deflection angle γ. Roll angle is calculated using the following equation:

$$\phi = \frac{\delta_2 - \delta_1}{C_1} - E_0 \tag{3.6}$$

where E_0 is a normalizing function, which depends on altitude of the satellite, and C_1 is a parameter depending on the physical character of the sensor.

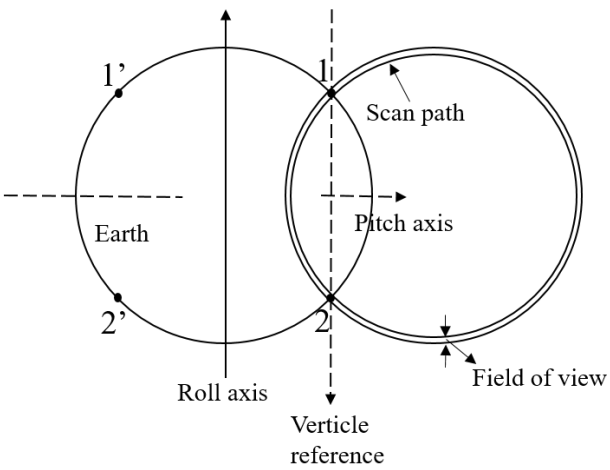

Figure 3.4: Calculation of pitch and yaw angle

In case y-axis of body frame Y_B is aligned with the y-axis of the orbit frame Y_O, intersection points of the scanning cone with Earth horizon must be on reference axis. But if there is a pitch angle between Y_B and Y_O pitch angle is determined as follows:

$$\theta = \frac{-(\delta_2 + \delta_1)}{2C_2} + \frac{90 + C_3}{C_2} + C_r\phi \tag{3.7}$$

where C_2, C_3, and C_r are constants. It is obvious that pitch angle coupled with roll angle for large roll deviations.

The only difference between dual conic scanning sensors and single conic scanning sensors is that by using two fixed mirrors dual conic scanning sensors scan two different parts of the Earth surface. Although they are more accurate than single conic scanning sensors, their measurement range is less than single conic scanning sensor. Moreover, in case satellite rotates around roll axis, only one scanning path can see the globe and sensor operates as a single conic scanning sensor. While viewing two different parts of the Earth, another bright celestial object such as the Sun or the Moon may go into sensor's field of view. One should use ephemeris data to overcome this problem. Obtaining 4 vectors by using two mirrors makes dual conic scanning sensors an overdetermined system since three vectors are enough to determine attitude angles. The extra vector also does not have any positive effect on the attitude accuracy.

3.1.3.2 Static Earth Sensors

Static Earth sensors determine 2-axis attitude by using fixed infra-red thermopiles. Static Earth sensors do not have a scanning mechanism so they are fixed on a direction. As it is seen in Figure 3.5, it has various number of infra-red radiance detectors. Similar to horizon crossing Earth sensors, they has a filter to detect CO_2 that only has wavelength between 14-16 μm and a lens to take projection of the Earth's horizon on thermopile detectors. Thermopiles which are on the projected Earth image has same sensing characteristics. D_e and D_t represent infra-red Earth diameter for the corresponding altitude and diameter of an imaginary circle tangent to thermopiles.

Static Earth sensors usualy consists of four thermopiles. For the sensor given in Figure 3.5, grey thermopiles are mounted for redundancy. Static Earth sensors should be designed to detect attitude accurately even if seasonal radiation variations occurs. For this, a mechanism should be provided to reposition the thermopiles if necessary.

Static Earth horizon sensors can measure attitude angles more accurately than horizon crossing Earth sensors owing to no part is moving. But their measurement range is

quite low compared to horizon crossing Earth sensors. The well known drawback of static Earth sensors is that they can operate in a small range of altitude. Therefore, they are calibrated for a specific range of altitude and cannot provide any reasonable measurements that can be used for attitude estimation.

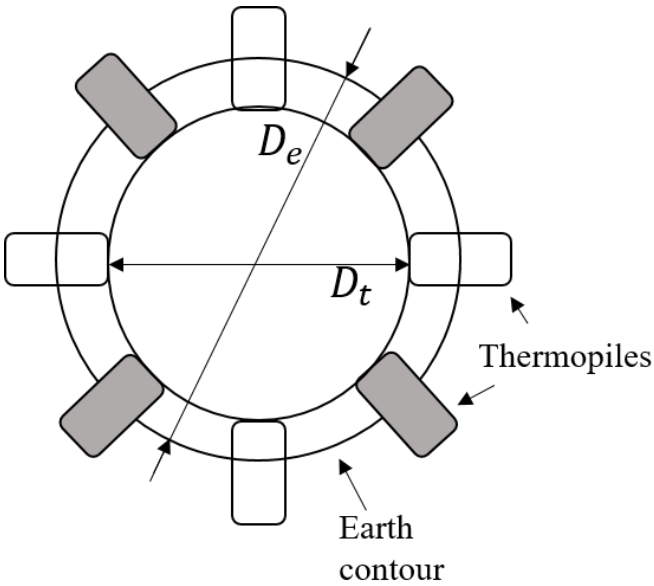

Figure 3.5: Static Earth sensor

3.1.4 Star Trackers

Star trackers are the most accurate attitude determination sensors because the stars are inertially fixed and they form almost a dot in the image frame when image is taken from solar system. These features of the stars allow one to determine attitude with error in arc second order. However, star trackers are expensive especially for small satellite budgets. They are also heavy compared to weight limit of small satellites. Since star tracker assemblies vary depending on the missions, star sensors must be designed according to requirements for each mission individually [32].

Stars can be categorised according to their emission spectra. There are seven spectral categories, which are O, B, A, F, G, K, and M. These categories also divided into ten groups, from 0 to 9 [32]. This categorisation plays important role on designing a star tracker for a specific mission due to the fact that each star tracker detects stars only within a limited spectral range. Calibrating star tracker for a special spectral range

prevents sensor to detect stars that are not chosen as reference. Although it is important to discriminate useful stars from others, to determine attitude continuously star trackers should be optimized to use as many star as they can. Unlike horizon crossing Earth sensor extra star direction vectors increases the accuracy of the determined attitude.

Star trackers detects position vector of a star in body reference frame. However, it is required to know their position vector in ECI frame to determine attitude of body frame with respect to ECI frame. Therefore, star catalogues have been published to provide position vectors of stars in ECI frame. Because of small rotation rate of vernal equinox axis, star catalogues have been updated for different time intervals. This catalogue is uploaded to on-board computer of satellites before launch. The latest catalogue was published in 1990 by Hirshfeld and Sinnott [37].

Attitude estimation diagram of star trackers is given in Figure 3.6. First, star catalogue is uploaded to the on-board computer of the spacecraft before launch. Then, star is identified by using geometries defined in catalogue. Next, position vector of the identified star is measured in body reference frame. After that, corresponding position vector resolved in ECI frame is found. Finally, by using both measured and corresponding reference catalogue vectors and an attitude determination algorithm (e.g. QUEST) attitude is determined. Star tracking assemblies of star trackers operates in three different principles. First one is called star scanners and designed for spinning satellites. They determine spin axis' attitude of the satellite. Second one is fixed-head star trackers and build for three-axis stabilized satellites. Fixed-head star trackers provide more accurate results than other two types. Last one is gimbaled star trackers. This type is designed to scan wider area in space and able to use more amount of stars to determine attitude. Nonetheless, this design type reduces the accuracy of the attitude.

Star trackerss consist of three components as shown in Figure 3.7 :

- **Optical system:** It has a lens to project stars light onto focus of optical system and a light shield to filter sunlight.

- **Starlight Detectors:** The most sophisticated detector is called charge coupled

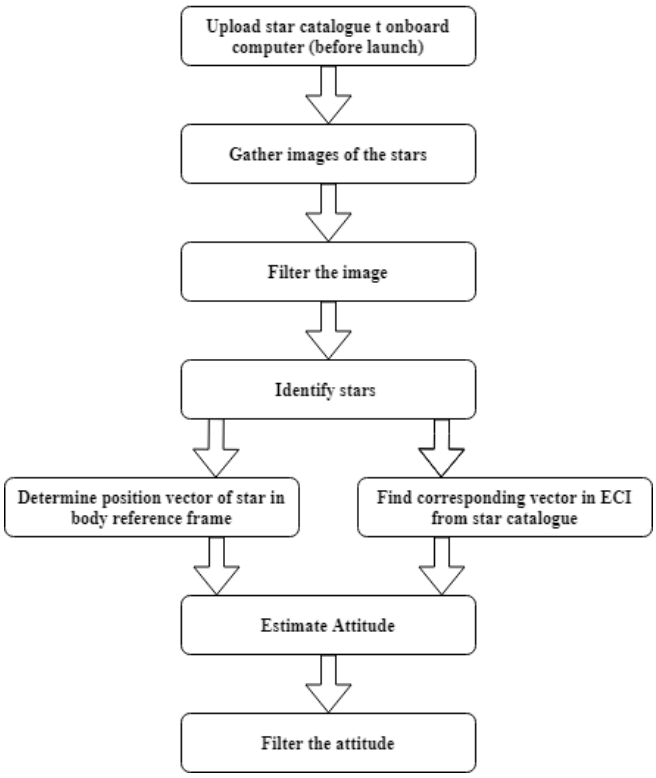

Figure 3.6: Attitude estimation diagram of star trackers

device (CCD) [32]. A CCD consists of light-sensitive semiconductors called pixels in a matrix pattern. The CCD also allows designers to limit the light spectrum of the sensors to certain ranges, to detect only stars of the desired spectrum. Position of the projected image on the CCD matrix can be determined from digital output of the CCD. Decreasing pixel size increases the attitude accuracy. But in case pixel size is decreased, a bigger matrix with more amount of semiconductors is needed to scan the same size FOV. Therefore, CCD matrix should be designed according to requirements of the missions [38, 39].

- **Processor:** Processors have two main tasks. First one is identification of stars by using star catalogue. Second one is determining attitude using the CCD output and star catalogue. Depending on the attitude determination system design, attitude rates may be calculated as well.

It is obvious that obtaining position vector in body reference frame of a star without identifying the star in the star catalogue is pointless regarding to attitude determi-

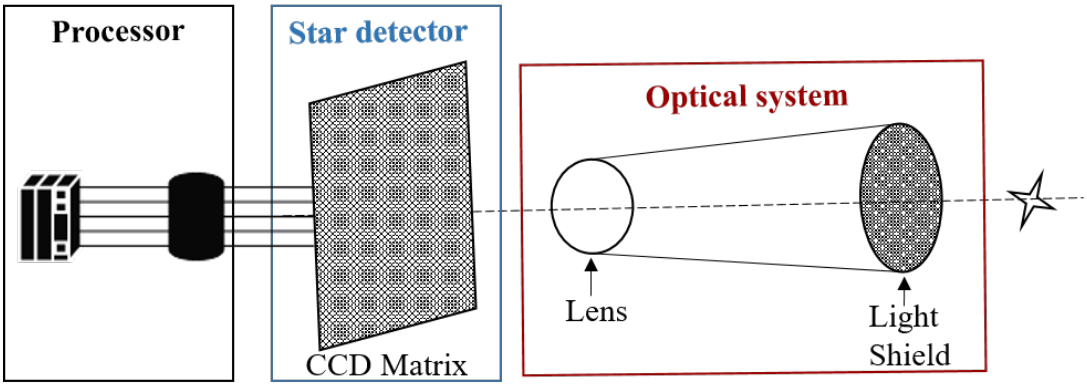

Figure 3.7: Star tracker design

nation. Star identification algorithms can be separated in two categories: First category is called as lost in space algorithms, in which no attitude information history is required. Second one is the recursive algorithms, in which an initial attitude information is needed to determine attitude recursively. In order to distinguish stars both categories uses angles between stars and/or brightness of stars. Details of star identification techniques is introduced in [40].

3.1.5 Gyroscopes

Gyroscopes are the sensors which measures angular velocity or angular displacement of a satellite. While rate gyroscopes measures 3-axis angular velocity $\{\omega_x,\ \omega_y,\ \omega_z\}$ of the spacecraft relative to ECI frame, rate-integrating gyroscopes provide angular displacement which is integrated angular velocity. With the developments in technology , different types of gyroscopes are invented. The gyroscopes most commonly used in small satellites can be summarized as follows: [30]

- **Ring Laser Gyroscopes (RLG):** This type of gyroscopes consist of three triangle shaped prisms orthogonal to each other to determine the angular rate on each axis. Inside structure of prisms is shown in Figure 3.8 [41]. While there is a laser detector at the one corner of the prisms, two mirrors is placed at other corners of prisms. There is a laser light source, which produce two laser lights in opposite directions, between two mirrors. In case of a rotation of this triangle

prism, length of the path that is taken by laser lights varies. This phenomenon causes two laser beams traveling in opposite directions to reach the detector at different times. RLG is able to obtain angular velocity owing to this time difference.

- **Fiber Obtic Gyroscopes (FOG):** FOGs uses the same principle with RLGs, except that FOGs have long fibre optic coils (in kilometer order) instead of prisms. Because fiber optic coils are in the range of kilometres, these sensors are considerably larger compared to RLGs.

- **Hemispherical Resonator Gyroscopes (HRG):** These sensors operates based on the fact that a Coriolis force which is generated by rotation causes mechanical surfaces to resonate. This resonance produces waves whose rate is dependent to angular velocity. HRGs measure angular velocity by using the relation between rate of wave and angular velocity.

- **Micro-electromechanical Systems Gyroscopes (MEMS):** MEMS gyroscopes are developed after the invention of silicon semiconductors like all other integrated circuits. Owing to cheap mass production of MEMS gyroscopes, they have become popular in both inertial navigation and attitude determination applications. There are several different mechanisms for MEMS gyroscopes to detect angular velocity, such as vibrating wheels, tuning folks, and masses that resonate with various types of designs.

Using gyroscopes in satellite attitude determination systems allows one to propagate attitude by integrating angular velocity measurements in case reference attitude sensors can not provide measurements. Gyroscope measurement model is defined as follows [42]:

$$\tilde{\omega} = \vec{\omega} + \vec{\mathrm{b}} + \vec{\nu} \tag{3.8}$$

where $\tilde{\omega}$ is the measurement of the gyroscopes. $\vec{\omega}$ is the the true angular velocity vector, $\vec{\mathrm{b}}$ represents gyroscope drifts vector and $\vec{\nu}$ is the Gaussian zero-mean measurement noise. Integrating angular velocity measurements of gyroscopes by time, causes

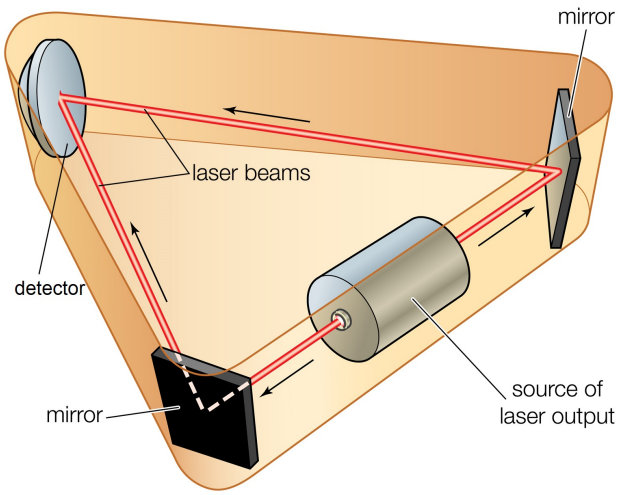

Figure 3.8: Ring laser gyroscopes

gyroscope drift to increase. Therefore, attitude determination systems includes attitude filters which cooperates gyroscope and reference attitude sensors measurements to determine attitude continuously.

3.2 Attitude Determination Methods

Attitude of a spacecraft must be known for all kind of space missions. Moreover, most of the tasks in space can be performed by controlling the spacecraft's attitude. Therefore, accurate attitude determination plays an important role to accomplish missions in space. Attitude information not only provides orientation of spacecraft to ground station but also tells how much torque required to bring spacecraft into the desired orientation.

Attitude determination is basically obtaining the rotation matrix that transforms a vector from a reference frame to body reference frame. The reference frame is generally considered to be an inertial frame, however it does not have to be. In satellite applications reference frame is usually taken as ECI frame or orbit frame. In Section 3.1, it is indicated that attitude determination sensors can provide a vector in body frame and and corresponding reference vector in ECI frame may be found from the models (e. g. IGRF). Hence, for any ith vector measurement there are versions of the same

vector resolved in reference frame $\vec{\mathbf{r}}_i$ and body frame $\vec{\mathbf{b}}_i$. These two vectors can be transformed to each other by using rotation matrix C_{BR} and for number of n sensors equation becomes:

$$\vec{\mathbf{b}}_i = C_{BI}\vec{\mathbf{r}}_i \quad \text{for} \quad i = 1, 2, ..., n \tag{3.9}$$

It is obvious from the Eq. (2.9) that rotation matrices are obtained by using three Euler angles between two frames. So, there are three independent variables to obtain a rotation matrix. On the other hand, it is mentioned before that reference sensors such as Sun sensor or magnetometer are able to provide attitude only in 2-axis at an instant. In case a vector couple consisting of a measured and reference vector are substituted into Eq. (3.9), system of equations becomes an under-determined system which has fewer equations than unknowns. Under-determined systems has infinite solutions, so one reference sensor is not sufficient to determine attitude. However, if two sensors are used to determine attitude, system of equations turns into an overdetermined system with three unknowns and four equations. Overdetermined systems have a non unique solution. Besides rotation matrix can not be uniquely obtained provided that either vectors measured by two different sensors in body frame $\vec{\mathbf{b}}_1$ and $\vec{\mathbf{b}}_2$ or corresponding vectors in reference frame $\vec{\mathbf{r}}_1$ and $\vec{\mathbf{r}}_2$ are parallel or anti-parallel (anti-parallel unit vector of a unit vector is basically obtained by multiplying the vector by (-1)) as shown in Figure 3.9. Since length of a vector does not avail to attitude determination, normalized unit vectors are used in attitude determination algorithms [43].

3.2.1 TRIAD Method

First applicable method of determining the attitude matrix from two measured and reference vector couples is TRIAD method published in 1964 [44]. TRIAD method is designed to use measurements of only two sensors. It fails to obtain orientation in case more than two sensors are available in attitude determination system. In TRIAD method, attitude matrix is obtained by multiplying two matrices consists of orthogonal right handed triad of vectors $\{\vec{\mathbf{w}}_1, \vec{\mathbf{w}}_2, \vec{\mathbf{w}}_3\}$ in the body frame and corresponding

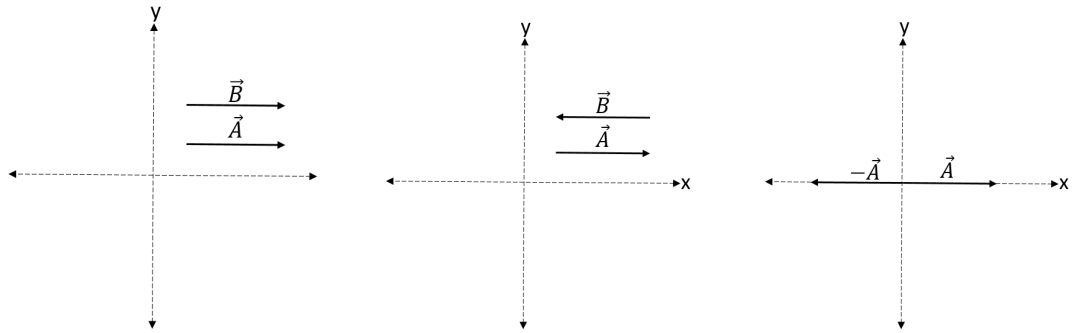

(a) Two parallel vectors (b) Two anti-parallel vectors (c) Anti-parallel unit vectors

Figure 3.9: Parallel and anti-parallel vectors

triad $\{\vec{\mathbf{v}}_1, \vec{\mathbf{v}}_2, \vec{\mathbf{v}}_3\}$ in the reference frame respectively:

$$C = \underbrace{\begin{bmatrix} \vec{\mathbf{w}}_1 & \vdots & \vec{\mathbf{w}}_2 & \vdots & \vec{\mathbf{w}}_3 \end{bmatrix}}_{bodyframe} \underbrace{\begin{bmatrix} \vec{\mathbf{v}}_1 & \vdots & \vec{\mathbf{v}}_2 & \vdots & \vec{\mathbf{v}}_3 \end{bmatrix}}_{referenceframe} = \vec{\mathbf{w}}_1\vec{\mathbf{v}}_1^{\mathsf{T}} + \vec{\mathbf{w}}_2\vec{\mathbf{v}}_2^{\mathsf{T}} + \vec{\mathbf{w}}_3\vec{\mathbf{v}}_3^{\mathsf{T}} \tag{3.10}$$

where vector triads $\{\vec{\mathbf{w}}_1, \vec{\mathbf{w}}_2, \vec{\mathbf{w}}_3\}$ and $\{\vec{\mathbf{v}}_1, \vec{\mathbf{v}}_2, \vec{\mathbf{v}}_3\}$ are determined by the following equations:

$$\vec{\mathbf{w}}_1 = \vec{\mathbf{b}}_1 \quad \text{and} \quad \vec{\mathbf{v}}_1 = \vec{\mathbf{r}}_1 \tag{3.11a}$$

$$\vec{\mathbf{w}}_2 = \frac{\vec{\mathbf{b}}_1 \times \vec{\mathbf{b}}_2}{\|\vec{\mathbf{b}}_1 \times \vec{\mathbf{b}}_2\|} \quad \text{and} \quad \vec{\mathbf{v}}_2 = \frac{\vec{\mathbf{r}}_1 \times \vec{\mathbf{r}}_2}{\|\vec{\mathbf{r}}_1 \times \vec{\mathbf{r}}_2\|} \tag{3.11b}$$

$$\vec{\mathbf{w}}_3 = \vec{\mathbf{b}}_1 \times \vec{\mathbf{w}}_2 \quad \text{and} \quad \vec{\mathbf{v}}_3 = \vec{\mathbf{r}}_1 \times \vec{\mathbf{v}}_2 \tag{3.11c}$$

Eq. (3.11b) is the proof of the fact mentioned above; vectors $\vec{\mathbf{w}}_2$ and $\vec{\mathbf{v}}_2$ becomes undefined in case either measured vectors $\{\vec{\mathbf{b}}_1, \vec{\mathbf{b}}_2\}$ or reference vectors $\{\vec{\mathbf{r}}_1, \vec{\mathbf{r}}_2\}$ are parallel to each other. Also, Eq. (3.11a) indicates that the measurement of the first sensor is assigned to the first vector of the TRIAD, thus the first sensor must be the most reliable sensor for more accurate attitude estimation. Estimated attitude matrix

with TRIAD method is defined as:

$$\hat{C}_{TRIAD} = \vec{\mathbf{b}}_1\vec{\mathbf{r}}_1^{\intercal} + (\vec{\mathbf{b}}_1 \times \vec{\mathbf{w}}_2)(\vec{\mathbf{r}}_1 \times \vec{\mathbf{v}}_2)^{\intercal} + \vec{\mathbf{w}}_2\vec{\mathbf{v}}_2^{\intercal} \tag{3.12}$$

3.2.2 Wahba's Problem and Orthogonal Procrustes Problem

TRIAD method is needed to be improved in two ways. First, by defining an arbitrary weighting scalar, effect of the reliable sensors to calculation may be increased. Second, more than two sensor measurements may be taken into account. Grace Wahba defined a problem, which is called as "Wahba's problem" in literature, to overcome these disadvantages of TRIAD method in 1965 [45]. Definition of Wahba's problem can be summarized as finding an orthogonal matrix C with determinant $(+1)$ that minimizes loss function L and this loss function forms the basis of the most attitude determination methods:

$$L(C) \equiv \frac{1}{2}\sum_{i}^{n} a_i|\vec{\mathbf{b}}_i - C\vec{\mathbf{r}}_i|^2 \tag{3.13}$$

where $\vec{\mathbf{b}}_i$ is the measured vector by a ith sensor in body frame and $\vec{\mathbf{r}}_i$ is the corresponding reference vector in reference frame. a_i is the non-negative weighting scalar and n is the number of sensors that provides measurements. It is possible to modify the loss function in Eq. (3.13) and write it as:

$$L(C) = \sum_{i}^{n} a_i - tr(CB^{\intercal}) \quad \text{where} \quad B \equiv \sum_{i}^{n} a_i\vec{\mathbf{b}}_i\vec{\mathbf{r}}_i^{\intercal} \tag{3.14}$$

This form of the equation shows that when $tr(CB^{\intercal})$ is maximized, loss function $L(C)$ becomes minimum.

Special case of Wahba's problem is named "Orthogonal procrustes problem". This problem is to find an orthogonal matrix which maps a set of points closest to another set of points. Apart from Wahba's problem weights are identical. Furthermore, while Wahba's problem tries to find a proper rotation matrix, orthogonal procrustes problem

tries to find only an orthogonal matrix. The loss function of the orthogonal procrustes problem is defined as follows [46]

$$\|M\|_F^2 \equiv \sum_{ij} M_{ij}^2 = tr(MM^\intercal) \tag{3.15}$$

3.2.3 Davenport's Q Method

The first applicable solution of Wahba's problem is published by Paul Davenport in 1965 [47]. Attitude matrix C can be represented by quaternions as mentioned in Section 2.1.3:

$$C = (q_4^2 - |\vec{\mathbf{q}}|^2)I + 2\vec{\mathbf{q}}\vec{\mathbf{q}}^\intercal - 2q_4[\vec{\mathbf{q}}\times] \tag{3.16}$$

where $[\vec{\mathbf{q}}\times]$ represents a skew-symmetric cross-product matrix:

$$[\vec{\mathbf{q}}\times] = \begin{bmatrix} 0 & -q_3 & q_2 \\ q_3 & 0 & -q_1 \\ -q_2 & q_1 & 0 \end{bmatrix} \tag{3.17}$$

Eq. (3.17) is equivalent to the quadric function of $\bar{\mathbf{q}}$ as shown in Eq. (2.36):

$$tr(CB^\intercal) = \bar{\mathbf{q}}^\intercal K \bar{\mathbf{q}} \tag{3.18}$$

where K is a matrix with 4x4 dimensions and defined as:

$$K \equiv \begin{bmatrix} S - Itr(B) & \vec{\mathbf{z}} \\ \vec{\mathbf{z}}^\intercal & tr(B) \end{bmatrix} \quad \text{for} \quad S \equiv B + B^\intercal \tag{3.19}$$

and elements that forms the matrix K are expressed as:

$$S \equiv B + B^{\mathsf{T}} \tag{3.20a}$$

$$\vec{\mathbf{z}} \equiv \begin{bmatrix} B_{23} - B_{32} \\ B_{31} - B_{13} \\ B_{12} - B_{21} \end{bmatrix} \tag{3.20b}$$

$$B = \sum_{i}^{n} a_i \vec{\mathbf{b}}_i \times \vec{\mathbf{r}}_i \tag{3.20c}$$

At this point by substituting Lagrange multiplier λ for the quaternion norm constraint $\|\bar{\mathbf{q}}\| = 1$, Wahba's problem becomes Davenport's problem:

$$K\bar{\mathbf{q}} = \lambda\bar{\mathbf{q}} \tag{3.21}$$

Normalized eigenvector of matrix K corresponding to largest eigenvalue is the solution of the Eq. (3.21) and equals to the optimal attitude represented with quaternions. Davenport's q method is the most robust algorithm to solve Wahba's problem. Davenport's q method can not determine attitude in case two largest eigenvalues of matrix K are same. However, this is not this method's fault, it shows that measured data is not sufficient to determine attitude.

3.2.4 QUEST Method

Despite Davenport's q method is considered as the most robust estimator, its computational load was high at 1980s. So computationally less burdensome QUEST method was developed in 1981 [48]. Instead of computing the largest eigenvalue and its corresponding eigenvector, the characteristic polynomial of the matrix K is formulated

analytically by using Cayley-Hamilton theorem as:

$$f(\lambda) = \lambda^4 - (a+b)\lambda^2 - c\lambda + d = 0 \quad \text{where} \tag{3.22a}$$

$$a = tr(B)^2 - tr(ads(S)) \tag{3.22b}$$

$$b = tr(B)^2 + \vec{\mathbf{z}}^{\intercal}\vec{\mathbf{z}} \tag{3.22c}$$

$$c = det(S) + \vec{\mathbf{z}}^{\intercal}S\vec{\mathbf{z}} \tag{3.22d}$$

$$d = ab + ctr(B) - \vec{\mathbf{z}}^{\intercal}S^2\vec{\mathbf{z}} \tag{3.22e}$$

This equation may be solved by using Newton-Raphson method with a initial guess $\lambda_0 = 1$ since the largest eigenvalue of matrix K is usually close to 1. After calculating the λ_{max}, parameters below are computed to obtain quaternion solution:

$$\alpha = \lambda_{max}^2 - tr(B)^2 + tr(adj(S)) \tag{3.23a}$$

$$\beta = \lambda_{max} - tr(B) \tag{3.23b}$$

$$\gamma = \alpha(\lambda_{max} + tr(B)) - det(S) \tag{3.23c}$$

$$\vec{\mathbf{x}} = (\alpha I + \beta S + S^2)\vec{\mathbf{z}} \tag{3.23d}$$

Finally optimal quaternion representation of attitude is obtained by using equation below:

$$\bar{\mathbf{q}}_{opt} = \frac{1}{\sqrt{\gamma^2 + |\vec{\mathbf{x}}|^2}} \begin{bmatrix} \vec{\mathbf{x}} \\ \gamma \end{bmatrix} \tag{3.24}$$

Since solving characteristic equation numerically to find eigenvalues increases estimation error of attitude, Davenport's q method is more robust than QUEST method. But owing to less computational time and providing more frequent attitude data, QUEST was the attitude determination method that was used in the MAGSAT mission and in many other mission since then [49].

3.2.5 Singular Value Decomposition Method

Singular Value Decomposition (SVD) method is another robust algorithm but its computational time is even longer than Davenport's q method. This method is based on finding the right and left singular values of matrix B by using singular value decomposition [50]:

$$B = U\Sigma V^{\intercal} = U \begin{bmatrix} \Sigma_{11} & 0 & 0 \\ 0 & \Sigma_{22} & 0 \\ 0 & 0 & \Sigma_{33} \end{bmatrix} V^{\intercal} \tag{3.25}$$

where U and V are orthogonal matrices representing left and right singular values respectively. Attitude may be estimated using these matrices with the formula:

$$U_{+} = U \begin{bmatrix} 1 & 0 & 0 \\ 0 & 1 & 0 \\ 0 & 0 & det(U) \end{bmatrix} \tag{3.26a}$$

$$V_{+} = V \begin{bmatrix} 1 & 0 & 0 \\ 0 & 1 & 0 \\ 0 & 0 & det(V) \end{bmatrix} \tag{3.26b}$$

$$C_{opt} = U_{+}V_{+}^{\intercal} \tag{3.26c}$$

3.3 Attitude Estimation Filters

Attitude estimation filters basically tries to estimate current attitude state of a system from measurements. This state estimation is made using both dynamic mathematical model and measurements of the sensors. Because sensor measurements are utilized not only in dynamic mathematical model but also in measurement model, both are contaminated by random noise. The state vector consists of the variables which are desired to be estimated. In addition to attitude components, other variables may be

defined. For example in Section 4.2, it will be shown that coarse attitude information obtained by Sun sensor and magnetometer measurements can be used together with a kinematic model in which attitude is propagated by the help of gyroscope measurements. But it is a known fact that gyroscope measurements are corrupted with drift and also coarse attitude information is not error free. Therefore, by adding gyroscope drifts to states as a additional states to be estimated, the ill effect of gyroscope drift to the estimated attitude may be reduced. On the other hand, kinematic model may increase the accuracy of sensor measurements. That is why this type of filters are called complementary filters. Since filters are recursive methods which uses past estimates, they estimates attitude more accurate compared to static methods [23].

The most popular filter which is used to estimate attitude is Kalman filters (KF). KF yields a new state estimate with the intent of minimizing state's error covariance by bringing both linear state models (mathematical models of dynamic systems) and measurement models together. The first implementation of KF to the attitude estimation problem is published in 1964 [51]. Nonetheless, this trial failed to succeed because of the wrong modelling of the torques on the satellite. Researchers became interested in the use of quaternions for orientation representation in the early 1980s. One of the cornerstones of humankind's adventure in space is the inclusion of Kalman filter with a quaternion approach in the attitude estimation process [52]. The main advantage of representing attitude with quaternions is that it decreases computational burden. Nevertheless, quaternion unit constraint prevents adding or subtracting them each other to calculate state estimate error. Attitude dynamics and kinematics of a satellite are non-linear like many other systems. Therefore, EKF is presented to apply Kalman filter to non-linear systems [53]. However, linearisation affects filter performance in a bad manner especially for the cases that time step is not small enough.

Since the additive error correction violates the quaternion norm constraint, a multiplicative error representation is proposed in order to propagate quaternions in MEKF [54]. MEKF runs seven states, four of which are quaternions and 3 of which are gyroscope bias (or angular velocities in the absence of gyroscopes). Angular velocity measurements of gyroscopes are utilized in mathematical model to propagate attitude in time update part. On the other hand, quaternion multiplication is used to compute

attitude error in measurement update part of the filter. Different than EKF, MEKF reduces dimension of covariances to six. Owing to these features MEKF is considered to be the most robust version of EKF. MEKF constitutes the attitude estimation system of most satellites today [54, 55, 56]. Mohinder et al. [57] introduces briefly the applications of Kalman filtering in aerospace from 1960 to 2010.

3.3.1 Kalman Filters

KF is developed with the intent of estimating states of linear continuous systems. Since the kinematic model and in some cases even the measurement model is nonlinear, KF can not be used as an attitude estimation filter. However, the EKF and MEKF are developed based on the KF. So it is convenient to introduce the KF to help the reader for understanding the basics of the MEKF as an attitude filter. Since the sensors in attitude determination systems provide discrete measurements, only the discrete Kalman filter will be discussed in this section. The discrete Kalman filter is modelled assuming that both sensor measurements that used in both the mathematical model and measurement model are discrete measurements. Since these sensor measurements are also corrupted with noise, the discrete Kalman filter is modelled as:

$$\mathbf{x}_{k+1} = \Phi_k \mathbf{x}_k + \Gamma_k \mathbf{u}_k + \Upsilon \mathbf{w}_k \tag{3.27a}$$

$$\tilde{\mathbf{y}}_k = H_k \mathbf{x}_k + \mathbf{v}_k \tag{3.27b}$$

where $\mathbf{x}_k$ is the state vector, Φ_k is the system dynamics matrix, Γ_k is the input distribution matrix, $\mathbf{u}_k$ is the input vector, Υ_k is the transition matrix of system process noise, $\mathbf{w}_k$ is the white Gaussian system process noise, $\mathbf{z}_k$ is the measurement vector, $H(k)$ is the measurement matrix and $\mathbf{v}_k$is the white Gaussian measurement noise.

The stochastic elements of both system process $\mathbf{w}_k$ and measurements $\mathbf{v}_k$ are:

$$E\{\mathbf{w}_k\mathbf{w}_j^\intercal\} = \begin{cases} 0 & \text{for} \quad k \neq j \\ Q_k & \text{for} \quad k = j \end{cases} \tag{3.28a}$$

$$E\{\mathbf{v}_k\mathbf{v}_j^\intercal\} = \begin{cases} 0 & \text{for} \quad k \neq j \\ R_k & \text{for} \quad k = j \end{cases} \tag{3.28b}$$

While Q_k represents the process noise covariance matrix, R_k is defined as measurement noise covariance matrix. The discrete KF starts with an initialization of states and error covariance P_0 which is the expectation of the deviation of the estimated states from true states:

$$P_0 = E\{\tilde{\mathbf{x}}(t_0)\tilde{\mathbf{x}}^\intercal(t_0)\} \tag{3.29a}$$

$$\hat{\mathbf{x}}(t_0) = \hat{\mathbf{x}}_0 \tag{3.29b}$$

After the initialization system process update (time update) begins. This part is basically propagating states by using differential equations of system mathematical model until a attitude measurement comes from sensors:

$$\hat{\mathbf{x}}_k^- = \Phi_{k-1}\mathbf{x}_{k-1}^+ + \Gamma_{k-1}\mathbf{u}_{k-1} \tag{3.30a}$$

$$P_k^- = \Phi_{k-1}P_{k-1}^+\Phi_{k-1}^\intercal + \Upsilon_{k-1}Q_{k-1}\Upsilon_{k-1}^\intercal \tag{3.30b}$$

These are the *a priori* state estimate and error covariance, represented by $\hat{\mathbf{x}}_k^-$ and P_k^- respectively. $\hat{\mathbf{x}}_k^-$ and P_k^- are used as the initial state and error covariance for next time update until a measurement comes. At this point Kalman gain is calculated as:

$$K_k = P_k^- H_k^\intercal [H_k P_k^- H_k^\intercal + R_k]^{-1} \tag{3.31}$$

When a measurement comes from sensors, measurement update step of the filter begins. Using *a priori* state estimate $\hat{\mathbf{x}}_k^-$ and error covariance P_k^-, *a posteriori* state estimate $\hat{\mathbf{x}}_k^+$ and error covariance P_k^+ are computed as follows:

$$\hat{\mathbf{x}}_k^+ = \hat{\mathbf{x}}_k^- + K_k[\tilde{\mathbf{y}}_k - H_k\hat{\mathbf{x}}_k^-] \tag{3.32a}$$

$$\hat{P}_k^+ = [I - K_k H_k]\hat{P}_k^- \tag{3.32b}$$

An illustration of how the KF works is shown in Figure 3.10. The states are propagated in system process (time update) step of the filter until a measurement comes at time t_1. At this point a discrete state update is progressed in measurement update step of the filter, thus the final estimate of states is $\hat{\mathbf{x}}_1^+$. $\hat{\mathbf{x}}_1^-$ is the *a priori* state estimated which is calculated in system process step by using system mathematical model. $\hat{\mathbf{x}}_1^+$ is used as the initial condition for the next system process step and also it is propagated until a measurement comes again at time t_2. The time passed between two measurements (i.e t_1 and t_2) does not have to be constant. Filter can be designed to have measurement update whenever a measurement is available.

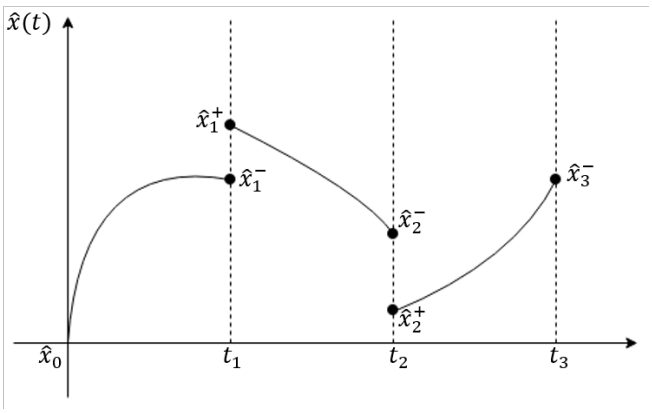

Figure 3.10: Illustration of a Kalman filter

3.3.2 Extended Kalman Filters

Many mathematical models are not linear like attitude kinematics. The EKF is developed based on KF introduced above for models whose system process or/and mea-

surement models are non-linear. Eq. (3.27a) may be written for non-linear systems as follows:

$$\dot{\mathbf{x}} = f(\mathbf{x}(t), \mathbf{u}(t), t) + \mathbf{w} \tag{3.33a}$$

$$\mathbf{z} = h(\mathbf{x}(t), t) + \mathbf{v} \tag{3.33b}$$

where $\mathbf{x}(t)$ is the state vector, $f(x,t)$ is the system dynamics matrix of non-linear systems, $\mathbf{w}(t)$ is the white Gaussian system process noise, $\mathbf{z}$ is the measurement vector, $h(x,t)$ is the measurement matrix and $\mathbf{v}$ is the white Gaussian measurement noise. Functions $f(x,t)$ and $h(x,t)$ must be linearised in order to be available to used in the KF by using first order Taylor series expansion:

$$f(\mathbf{x}(t), \mathbf{u}(t), t) \approx f(\bar{\mathbf{x}}(t), \mathbf{u}(t), t) + \left.\frac{\partial f}{\partial x}\right|_{\bar{\mathbf{x}}(t), \mathbf{u}(t)} \delta\mathbf{x} \tag{3.34a}$$

$$h(\mathbf{x}(t), t) \approx h(\bar{\mathbf{x}}(t), t) + \left.\frac{\partial h}{\partial x}\right|_{\bar{\mathbf{x}}(t)} \delta\mathbf{x} \tag{3.34b}$$

$$F(t) \equiv \left.\frac{\partial f}{\partial x}\right|_{\bar{\mathbf{x}}(t), \mathbf{u}(t)} \tag{3.34c}$$

$$H(t) \equiv \left.\frac{\partial h}{\partial x}\right|_{\bar{\mathbf{x}}(t)} \tag{3.34d}$$

Discrete time versions of those matrices are calculated as :

$$F_k = I + F\Delta t \tag{3.35a}$$

$$H_k = I + H\Delta t \tag{3.35b}$$

After substituting linearised F and H matrices into the Eq (3.27a) and Eq (3.27b), the same process steps should be followed with the KF. The only difference from the KF is that functions $f(x,t)$ and $h(x,t)$ must be linearised at the beginning of each step with the change of estimated states.

3.3.3 Multiplicative Extended Kalman Filter

There are different ways to represent attitude as discussed in Section 2.1. Since Euler angles have only three variables, they may be considered as the best choice for representing the attitude in a filter. However, Euler angles have discontinuities and singularities and these singularities may cause trouble to filter designer. Euler angles have been usually used for nadir pointing spacecraft when the attitude is defined with respect to the orbit frame due to small deviations in the angles.

There are two options remaining: DCM and quaternions. Using quaternion to represent the attitude strengthens our hand in three ways. First, quaternion has four components while direction cosine matrix (DCM) has nine. Secondly, in case quaternion norm deviates from unity, it is straightforward to normalize the quaternions. Nonetheless, correction on orthogonality of DCM is not that easy. Next, quaternion is the lowest-dimensional representation that does not have any singularities.

Quaternion unit norm constraint is a problem to overcome during designing an attitude filter. If quaternion error is modelled additively as given in Eq. (3.36), this problem becomes pretty challenging to overcome:

$$\bar{\mathbf{q}}^{true} \equiv \Delta\bar{\mathbf{q}} + \hat{\mathbf{q}} \tag{3.36}$$

But this true quaternion can also be defined by multiplication of error vector and estimated quaternion as follows:

$$\bar{\mathbf{q}}^{true} \equiv \boldsymbol{\delta}\bar{\mathbf{q}} \otimes \hat{\mathbf{q}} \tag{3.37}$$

Error vector $\boldsymbol{\delta}\bar{\mathbf{q}}$ is written on the left hand side intentionally; it shows that error vector is defined in body reference frame. This filter is called multiplicative extended Kalman filter because of the multiplicative error calculation [23].

The MEKF consists of three steps; initialisation, system process update (also called time update or propagation step) and measurement update. Initialisation part only runs at the first iteration of the filter, after the first iteration only system process update

and measurement update are applied recursively. [23].

Initial parameters may be obtained by using a batch filter on the measurements that are just collected. Initialization starts with defining the initial values of quaternions, gyroscope bias, angular velocity and error quaternion:

$$\hat{\mathbf{q}}_0 = \begin{bmatrix} q_1 \\ q_2 \\ q_3 \\ q_4 \end{bmatrix} \tag{3.38a}$$

$$\vec{\boldsymbol{\beta}}_{\mathbf{0}} = \begin{bmatrix} \beta_x \\ \beta_y \\ \beta_z \end{bmatrix} \tag{3.38b}$$

$$\vec{\boldsymbol{\omega}}_{\mathbf{0}} - \vec{\boldsymbol{\beta}}_{\mathbf{0}} = \begin{bmatrix} \omega_x \\ \omega_y \\ \omega_z \end{bmatrix} - \begin{bmatrix} \beta_x \\ \beta_y \\ \beta_z \end{bmatrix} \tag{3.38c}$$

$$\boldsymbol{\delta}\bar{\mathbf{q}} \equiv \bar{\mathbf{q}} \otimes \hat{\mathbf{q}}^{-1} \tag{3.38d}$$

At this point, states of the MEKF should be defined with small angle assumption. This assumption is that due to spacecraft's rotation is very small between two steps of the filter, states can be defined as Euler angles which are equals to two times of first three elements of quaternion representation. By making this assumption number of states are reduced to six that involves three Euler angles estimates $\boldsymbol{\delta\alpha}$ and three gyroscope bias estimates $\vec{\boldsymbol{\beta}}_{\mathbf{0}}$ [23]:

$$\boldsymbol{\delta\alpha} = 2\boldsymbol{\delta}\vec{\mathbf{q}} \tag{3.39a}$$

$$\boldsymbol{\delta x}_{\mathbf{0}} = \begin{bmatrix} \boldsymbol{\delta\alpha} \\ \vec{\boldsymbol{\beta}}_{\mathbf{0}} \end{bmatrix} \tag{3.39b}$$

Initialization step is finalised with defining the initial error covariance:

$$P_0 = E\{\boldsymbol{\delta x_0} \boldsymbol{\delta x_0}^{\intercal}\} \tag{3.40}$$

After initialization step, system process update step begins. This step is basically propagation of quaternions using gyroscope measurements as mentioned before. Quaternion based attitude is propagated according to well known formula:

$$\dot{\bar{\mathbf{q}}} = \frac{\mathbf{1}}{\mathbf{2}} \begin{bmatrix} \omega_x \\ \omega_y \\ \omega_z \\ 0 \end{bmatrix} \otimes \bar{\mathbf{q}} \tag{3.41a}$$

$$\dot{\bar{\mathbf{q}}} = \frac{\mathbf{1}}{\mathbf{2}} \begin{bmatrix} \vec{\boldsymbol{\omega}} \\ 0 \end{bmatrix} \otimes \bar{\mathbf{q}} \tag{3.41b}$$

where $\vec{\boldsymbol{\omega}}$ is the angular velocity vector in body reference measured by gyroscopes on satellite (and corrected using the estimated bias terms). This statement may cause some confusion because a measured parameter has not been used in measurement update state. The MEKF is designed to use measured attitude information (obtained by using attitude sensors such as magnetometer, Sun sensors or star trackers) in measurement update step, while gyroscope measurements are used to propagate attitude in system process step. Therefore, gyroscopes should also be modelled to substitute into kinematic equations [58]:

$$\vec{\boldsymbol{\omega}} = \tilde{\boldsymbol{\omega}} - \vec{\boldsymbol{\beta}} - \boldsymbol{\eta}_v \tag{3.42a}$$

$$\dot{\boldsymbol{\beta}} = \boldsymbol{\eta}_u \tag{3.42b}$$

where $\vec{\boldsymbol{\omega}}$ is the true angular velocity, $\tilde{\boldsymbol{\omega}}$ is the output of the gyroscopes, $\boldsymbol{\beta}$ represents the gyroscope bias and $\boldsymbol{\eta}_v$ and $\boldsymbol{\eta}_u$ are the Gaussian white noise. The expectation of

these stochastic noise variables can be estimated using equations below:

$$E\{\boldsymbol{\eta}_v(t)\boldsymbol{\eta}_v(\tau)^\intercal\} = \sigma_v^2\delta(t-\tau)I \tag{3.43a}$$

$$E\{\boldsymbol{\eta}_u(t)\boldsymbol{\eta}_u(\tau)^\intercal\} = \sigma_u^2\delta(t-\tau)I \tag{3.43b}$$

$$E\{\boldsymbol{\eta}_v(t)\boldsymbol{\eta}_u(t)^\intercal\} = \begin{bmatrix} 0 & 0 & 0 \\ 0 & 0 & 0 \\ 0 & 0 & 0 \end{bmatrix} \tag{3.43c}$$

σ_v and σ_u are the standard deviations of gyroscope sensor and should be provided by manufacturer of the sensor. The gyroscope model to be used in he attitude filter are:

$$\hat{\boldsymbol{\omega}} = \tilde{\boldsymbol{\omega}} - \hat{\boldsymbol{\beta}} \tag{3.44a}$$

$$\dot{\hat{\boldsymbol{\beta}}} = 0 \tag{3.44b}$$

Let's go back to attitude quaternion propagation. If derivative of Eq. (3.37) is taken, it becomes:

$$\dot{\bar{\boldsymbol{q}}}^{true} = \boldsymbol{\delta}\dot{\bar{\mathrm{q}}} \otimes \hat{\mathrm{q}} + \boldsymbol{\delta}\bar{\mathrm{q}} \otimes \dot{\hat{\mathrm{q}}} \tag{3.45}$$

Substituting Eq. (3.41a) and Eq. (3.44a) into Eq.(3.45) yields:

$$\boldsymbol{\delta}\dot{\bar{\boldsymbol{q}}} = -\begin{bmatrix} \hat{\boldsymbol{\omega}} \times \boldsymbol{\delta}\vec{\boldsymbol{q}} \\ 0 \end{bmatrix} + \frac{1}{2}\begin{bmatrix} \boldsymbol{\delta}\vec{\boldsymbol{\omega}} \\ 0 \end{bmatrix} \otimes (\boldsymbol{\delta}\bar{\boldsymbol{q}} - \boldsymbol{q}_I + \boldsymbol{q}_I) \tag{3.46}$$

where $\delta\vec{\omega}$ is the angular velocity error and $\boldsymbol{q}_I$ is the identity quaternion expressed as:

$$\vec{\omega} = \hat{\omega} + \delta\vec{\omega} \tag{3.47a}$$

$$\boldsymbol{q}_I = \begin{bmatrix} 0 \\ 0 \\ 0 \\ 1 \end{bmatrix} \tag{3.47b}$$

Eq. (3.46) is the non-linear kinematic equation of attitude quaternions. In order to linearise the equation last term on the right hand side of the equation is removed since this multiplication has really small effect on the results. The linearised kinematic equation of attitude quaternion is given below:

$$\delta\dot{\vec{q}} = -\begin{bmatrix} \hat{\omega} \times \delta\vec{q} \\ 0 \end{bmatrix} + \frac{1}{2}\begin{bmatrix} \delta\vec{\omega} \\ 0 \end{bmatrix} \tag{3.48}$$

Gyroscope error may be written in terms of gyroscope bias and Gaussian white noise as follows:

$$\delta\vec{\omega} = \vec{\omega} - \hat{\omega} = -(\delta\vec{\beta} + \boldsymbol{\eta}_v) \tag{3.49}$$

The final attitude quaternion kinematic equations are obtained by substituting Eq. (3.49) into Eq. (3.48):

$$\delta\dot{\vec{q}} = -\hat{\omega} \times \delta\vec{q} - \frac{1}{2}(\delta\vec{\beta} + \boldsymbol{\eta}_v) \tag{3.50a}$$

$$\delta\dot{q}_4 = 0 \tag{3.50b}$$

Here, small angle assumption in which quaternion vector equals to the half of the Euler angles for small rotations is made to calculate Euler angles from obtained attitude

quaternions:

$$\boldsymbol{\delta\dot{\alpha}} = -\hat{\boldsymbol{\omega}} \times \boldsymbol{\delta\alpha} - (\boldsymbol{\delta\vec{\beta}} + \boldsymbol{\eta}_v) \tag{3.51}$$

Thus, error state equations may be defined as:

$$\boldsymbol{\delta\dot{x}}(t) = F(t)\boldsymbol{\delta x}(t) + G(t)\boldsymbol{w}(t) \quad \text{where} \tag{3.52a}$$

$$\boldsymbol{\delta x} \equiv \begin{bmatrix} \boldsymbol{\delta\alpha} \\ \boldsymbol{\delta\beta} \end{bmatrix} \tag{3.52b}$$

$$\boldsymbol{\delta w}(t) \equiv \begin{bmatrix} \boldsymbol{\eta}_v \\ \boldsymbol{\eta}_u \end{bmatrix} \tag{3.52c}$$

$$F(t) = \begin{bmatrix} -[\hat{\boldsymbol{\omega}}\times] & -I \\ 0_{3\times3} & 0_{3\times3} \end{bmatrix} \tag{3.52d}$$

$$G(t) = \begin{bmatrix} -I & 0_{3\times3} \\ 0_{3\times3} & I \end{bmatrix} \tag{3.52e}$$

In addition to attitude quaternions, error covariance P is also propagated at system process step of the MEKF:

$$\dot{P} = FP + PF^{\intercal} + GQG^{\intercal} \quad \text{where} \tag{3.53a}$$

$$Q = \begin{bmatrix} \sigma_v^2 I & 0_{3\times3} \\ 0_{3\times3} & \sigma_u^2 I \end{bmatrix} \tag{3.53b}$$

After system process update is completed, measurement update step begins to update states with the attitude obtained by reference attitude sensors such as star trackers, magnetometers, sun sensors and Earth sensors. As discussed in Section (3.2), two or more reference sensors are required to determine attitude. Shuster [59] developed a model that combines QUEST method with errors caused by white Gaussian noise of

the sensors:

$$\vec{\mathbf{b}}_i = C_{BR}\vec{\mathbf{r}}_i + \boldsymbol{\upsilon}_i \quad \text{for} \quad i = 1, 2, ..., n \tag{3.54a}$$

$$\boldsymbol{\upsilon}_i^{\intercal} C_{BR} \boldsymbol{\upsilon}_i = 0 \tag{3.54b}$$

where $\vec{\mathbf{b}}_i$ represents measurements of each sensor in body frame, $\vec{\mathbf{r}}_i$ is the corresponding vector of these measurements in reference frame and C_{BR} is the transformation matrix that transforms a vector from reference frame to body frame. It is assumed that υ_i is zero-mean Gaussian noise and each sensor's noise is independent from each other. The measurement noise covariance matrix for this model is expressed as:

$$E\{\boldsymbol{\upsilon}_i \boldsymbol{\upsilon}_i^{\intercal}\} = \delta_i \sigma_i^2 [I - (C_{BR}\vec{\mathbf{r}}_i)(C_{BR}\vec{\mathbf{r}}_i)^{\intercal}] \tag{3.55a}$$

$$R_k = diag[\sigma_1^2 I \quad \sigma_2^2 I \quad \cdots \quad \sigma_n^2 I] \tag{3.55b}$$

The measurement in body frame may be defined as function of the states. Determination of the sensitivity matrix $H_k(\hat{\mathbf{x}}^-)$ is the next step of the filter. Discrete measurement model of sensors are defined in Eq. (3.54). Then, the measurement update of n sensors may be modelled as:

$$\tilde{\boldsymbol{z}}_k = \boldsymbol{h}_k(\hat{\mathbf{x}}_k) + \boldsymbol{\upsilon}_k \tag{3.56a}$$

$$\tilde{\boldsymbol{z}}_k = \begin{bmatrix} C_{BR}(\bar{\boldsymbol{q}})\boldsymbol{r}_1 \\ C_{BR}(\bar{\boldsymbol{q}})\boldsymbol{r}_2 \\ \vdots \\ C_{BR}(\bar{\boldsymbol{q}})\boldsymbol{r}_n \end{bmatrix}_{tk} + \begin{bmatrix} \boldsymbol{\upsilon}_1 \\ \boldsymbol{\upsilon}_2 \\ \vdots \\ \boldsymbol{\upsilon}_n \end{bmatrix}_{tk} \tag{3.56b}$$

The true attitude matrix is defined by multiplication of error attitude matrix and estimated attitude matrix. These matrices are obtained from related quaternions accord-

ing to the Eq. (2.2):

$$C_{BR}(\bar{\boldsymbol{q}}) = C_{BR}(\boldsymbol{\delta}\bar{\boldsymbol{q}})C_{BR}(\hat{\boldsymbol{q}}^{-}) \tag{3.57}$$

Error attitude matrix may be defined with the small angle assumption as:

$$A(\boldsymbol{\delta}\bar{\boldsymbol{q}}) \approx I - [\boldsymbol{\delta\alpha}\times] \tag{3.58}$$

The estimated and true measurements in body frame are $\mathbf{b} = C_{BR}(\bar{\boldsymbol{q}})\mathbf{r}$ and $\hat{\mathbf{b}}^{-} = C_{BR}(\hat{\boldsymbol{q}}^{-})\mathbf{r}$. Substituting these equations into Eq. (3.57) is resulting with the equation below:

$$\Delta\mathbf{b} = [C_{BR}(\hat{\boldsymbol{q}}^{-})\mathbf{r}\times]\boldsymbol{\delta\alpha} \tag{3.59}$$

Thus sensitivity matrix is determined as [60]:

$$H_k(\hat{\mathbf{x}}_k^{-}) = \begin{bmatrix} [C_{BR}(\hat{\boldsymbol{q}}^{-})\boldsymbol{r}_1\times] & 0_{3\times3} \\ [C_{BR}(\hat{\boldsymbol{q}}^{-})\boldsymbol{r}_2\times] & 0_{3\times3} \\ \vdots & \vdots \\ [C_{BR}(\hat{\boldsymbol{q}}^{-})\boldsymbol{r}_n\times] & 0_{3\times3} \end{bmatrix}_{tk} \tag{3.60}$$

Before updating quaternions and gyroscope bias, Kalman gain should be calculated:

$$K_k = P_k^{-}H_k^{\intercal}(\hat{\mathbf{x}}_k^{-})[H_k(\hat{\mathbf{x}}_k^{-})P_k^{-}H_k^{\intercal}(\hat{\mathbf{x}}_k^{-}) + R]^{-1} \tag{3.61}$$

States that involves Euler angles errors and gyroscope bias is updated with the help

of Kalman gain:

$$\boldsymbol{\delta}\hat{\mathbf{x}}_k^+ \equiv \begin{bmatrix} \boldsymbol{\delta}\hat{\boldsymbol{\alpha}}_k^+ \\ \boldsymbol{\delta}\hat{\boldsymbol{\beta}}_k^+ \end{bmatrix} = K_k[\mathbf{z}_k - \mathbf{h}_k(\hat{\mathbf{x}}_k^-)] \quad \text{where} \tag{3.62a}$$

$$\mathbf{h}_k(\hat{\mathbf{x}}_k^-) = \begin{bmatrix} C_{BR}(\hat{\boldsymbol{q}}^-)\boldsymbol{r}_1 \\ C_{BR}(\hat{\boldsymbol{q}}^-)\boldsymbol{r}_2 \\ \vdots \\ C_{BR}(\hat{\boldsymbol{q}}^-)\boldsymbol{r}_n \end{bmatrix}_{tk} \tag{3.62b}$$

The gyroscope bias is corrected with the estimated gyroscope bias:

$$\hat{\boldsymbol{\beta}}_k^+ = \hat{\boldsymbol{\beta}}_k^- + \delta\hat{\boldsymbol{\beta}}_k^+ \tag{3.63}$$

Next, quaternion update should be completed:

$$\hat{\mathbf{q}}_k^+ = \hat{\mathbf{q}}_k^- + \frac{1}{2}\Xi(\hat{\mathbf{q}}_k^-)\boldsymbol{\delta}\hat{\boldsymbol{\alpha}}_k^+ \quad \text{where} \tag{3.64a}$$

$$\Xi(\bar{\mathbf{q}}) = \begin{bmatrix} q_4 I + [\vec{\mathbf{q}}\times] \\ -\vec{\mathbf{q}}^\intercal \end{bmatrix} \tag{3.64b}$$

Measurement update step is finalized by updating error covariance:

$$P_k^+ = [I - K_k H_k(\hat{\mathbf{x}}_k^-)]P_k^- \tag{3.65}$$

A MEKF algorithm with continuous system process step and discrete measurement step is illustrated in Table 3.2 from beginning to end.

The algorithm given in Table 3.2 consists of a continuous system process update and discrete measurement update. This algorithm is designed assuming that frequency of gyroscope measurements are higher than the reference attitude sensors. However, in case both gyroscopes and reference attitude sensors has the same frequency, system

process update step should also contains discrete time equations. Actually, discrete time systems are standard in most dynamic system modelling, estimation or control algorithms because sensors provides discrete data. Output of the micro-controllers used to control dynamic systems is also discrete. Obtaining the discrete time version of a continuous time system is done with a series expansion process. To make this calculation easy, the sampling time is checked. First four elements of the expansion is enough to obtain discrete time system matrix unless the sampling time is higher than the Nyquist's upper limit. Discrete MEKF is introduced briefly in [60]. Discrete MEKF algorithm is given in Table 3.3.

Table 3.2: A MEKF algorithm with continuous system process update and discrete measurement update [23]

Initialization	$\hat{\mathbf{q}}_0 = \begin{bmatrix} q_1 & q_2 & q_3 & q_4 \end{bmatrix}^\intercal$ $\vec{\boldsymbol{\beta}}_{\mathbf{0}} = \begin{bmatrix} \beta_x & \beta_y & \beta_z \end{bmatrix}^\intercal$ $\hat{\boldsymbol{\omega}}_{\mathbf{0}} = \tilde{\boldsymbol{\omega}}_{\mathbf{0}} - \vec{\boldsymbol{\beta}}_{\mathbf{0}}$ $\boldsymbol{\delta}\bar{\mathbf{q}} \equiv \bar{\mathbf{q}} \otimes \hat{\mathbf{q}}^{-1}$ $\boldsymbol{\delta\alpha} = 2\boldsymbol{\delta}\vec{\mathbf{q}}$ $\boldsymbol{\delta}\mathbf{x}_0 = \begin{bmatrix} \boldsymbol{\delta\alpha} \\ \vec{\boldsymbol{\beta}}_{\mathbf{0}} \end{bmatrix}$ $P_0 = E\{\boldsymbol{\delta}\mathbf{x}_0 \boldsymbol{\delta}\mathbf{x}_0^\intercal\}$
System process update	$\hat{\boldsymbol{\omega}} = \tilde{\boldsymbol{\omega}} - \hat{\boldsymbol{\beta}}$ $\boldsymbol{\delta}\dot{\vec{\boldsymbol{q}}} = -\hat{\boldsymbol{\omega}} \times \boldsymbol{\delta}\vec{\boldsymbol{q}} - \frac{1}{2}(\boldsymbol{\delta}\vec{\boldsymbol{\beta}} + \boldsymbol{\eta}_v)$ $\delta\dot{q}_4 = 0$ $Q = \begin{bmatrix} \sigma_v^2 I & 0_{3\times3} \\ 0_{3\times3} & \sigma_u^2 I \end{bmatrix}$ $F(t) = \begin{bmatrix} -[\hat{\boldsymbol{\omega}}^\times] & -I \\ 0_{3\times3} & 0_{3\times3} \end{bmatrix}$ $G(t) = \begin{bmatrix} -I & 0_{3\times3} \\ 0_{3\times3} & I \end{bmatrix}$ $\dot{P}(t) = F(t)P(t) + P(t)F^\intercal(t) + G(t)Q(t)G^\intercal(t)$
Measurement update	$K_k = P_k^- H_k^\intercal(\hat{\mathbf{x}}_k^-)[H_k(\hat{\mathbf{x}}_k^-)P_k^- H_k^\intercal(\hat{\mathbf{x}}_k^-) + R]^{-1}$ $H_k(\hat{\mathbf{x}}_k^-) = \begin{bmatrix} [C_{BR}(\hat{\boldsymbol{q}}^-)\boldsymbol{r}_1^\times] & 0_{3\times3} \\ [C_{BR}(\hat{\boldsymbol{q}}^-)\boldsymbol{r}_2^\times] & 0_{3\times3} \\ \vdots & \vdots \\ [C_{BR}(\hat{\boldsymbol{q}}^-)\boldsymbol{r}_n^\times] & 0_{3\times3} \end{bmatrix}_{tk}$ $\boldsymbol{\delta}\hat{\mathbf{x}}_k^+ \equiv \begin{bmatrix} \boldsymbol{\delta}\hat{\boldsymbol{\alpha}}_k^+ \\ \boldsymbol{\delta}\hat{\boldsymbol{\beta}}_k^+ \end{bmatrix} = K_k[\mathbf{z}_k - \mathbf{h}_k(\hat{\mathbf{x}}_k^-)]$ where $\mathbf{h}_k(\hat{\mathbf{x}}_k^-) = \begin{bmatrix} C_{BR}(\hat{\boldsymbol{q}}^-)\boldsymbol{r}_1 \\ C_{BR}(\hat{\boldsymbol{q}}^-)\boldsymbol{r}_2 \\ \vdots \\ C_{BR}(\hat{\boldsymbol{q}}^-)\boldsymbol{r}_n \end{bmatrix}_{tk}$ $\hat{\boldsymbol{\beta}}_k^+ = \hat{\boldsymbol{\beta}}_k^- + \delta\hat{\boldsymbol{\beta}}_k^+$ $\hat{\mathbf{q}}_k^+ = \hat{\mathbf{q}}_k^- + \frac{1}{2}\Xi(\hat{\mathbf{q}}_k^-)\boldsymbol{\delta}\hat{\boldsymbol{\alpha}}_k^+$ $P_k^+ = [I - K_k H_k(\hat{\mathbf{x}}_k^-)]P_k^-$

Table 3.3: The discrete MEKF algorithm [23]

Initialization	$\hat{\mathbf{q}}_0 = \begin{bmatrix} q_1 & q_2 & q_3 & q_4 \end{bmatrix}^\intercal$ $\vec{\boldsymbol{\beta}}_{\mathbf{0}} = \begin{bmatrix} \beta_x & \beta_y & \beta_z \end{bmatrix}^\intercal$ $\hat{\boldsymbol{\omega}}_{\mathbf{0}} = \tilde{\boldsymbol{\omega}}_{\mathbf{0}} - \vec{\boldsymbol{\beta}}_{\mathbf{0}}$ $\boldsymbol{\delta}\bar{\mathbf{q}} \equiv \bar{\mathbf{q}} \otimes \hat{\mathbf{q}}^{-1}$ $\boldsymbol{\delta\alpha} = 2\boldsymbol{\delta}\vec{\mathbf{q}}$ $\boldsymbol{\delta}\mathbf{x}_0 = \begin{bmatrix} \boldsymbol{\delta\alpha} \\ \vec{\boldsymbol{\beta}}_{\mathbf{0}} \end{bmatrix}$ $P_0 = E\{\boldsymbol{\delta}\mathbf{x}_0 \boldsymbol{\delta}\mathbf{x}_0^\intercal\}$
System process update	$\hat{\boldsymbol{\omega}}_k^- = \tilde{\boldsymbol{\omega}} - \hat{\boldsymbol{\beta}}_{k-1}^+$ $\Delta\hat{\boldsymbol{\omega}}_k^- = \lVert\hat{\boldsymbol{\omega}}_k^-\rVert\Delta t$ $\hat{\mathbf{e}}_k^- = \begin{cases} \frac{\hat{\boldsymbol{\omega}}_k^-}{\lVert\hat{\boldsymbol{\omega}}_k^-\rVert} & \text{for} \quad \lVert\hat{\boldsymbol{\omega}}_k^-\rVert \neq 0 \\ 0 \quad \text{for} \quad \lVert\hat{\boldsymbol{\omega}}_k^-\rVert = 0 \end{cases}$ $\Phi = \begin{bmatrix} \phi_{11} & \phi_{12} \\ 0_{3\times3} & I_{3\times3} \end{bmatrix}$ $\phi_{11} = I_{3\times3} - \frac{[\hat{\boldsymbol{\omega}}_k^-\times]}{\lVert\hat{\boldsymbol{\omega}}_k^-\rVert}\sin(\lVert\hat{\boldsymbol{\omega}}_k^-\rVert\Delta t) + \frac{[\hat{\boldsymbol{\omega}}_k^-\times]^2}{\lVert\hat{\boldsymbol{\omega}}_k^-\rVert^2}(1-\cos(\lVert\hat{\boldsymbol{\omega}}_k^-\rVert\Delta t))$ $\phi_{12} = -I_{3\times3}\Delta t + \frac{[\hat{\boldsymbol{\omega}}_k^-\times]}{\lVert\hat{\boldsymbol{\omega}}_k^-\rVert^2}(1-\cos(\lVert\hat{\boldsymbol{\omega}}_k^-\rVert\Delta t)) - \frac{[\hat{\boldsymbol{\omega}}_k^-\times]^2}{\lVert\hat{\boldsymbol{\omega}}_k^-\rVert^3}(\lVert\hat{\boldsymbol{\omega}}_k^-\rVert\Delta t - \sin(\lVert\hat{\boldsymbol{\omega}}_k^-\rVert\Delta t))$ $G_k = \begin{bmatrix} (-I_{3\times3} & 0_{3\times3} \\ 0_{3\times3} & I_{3\times3} \end{bmatrix}$ $Q = \begin{bmatrix} (\sigma_v^2\Delta t + \frac{1}{3}\sigma_u^2\Delta t^3)I_{3\times3} & -(\frac{1}{2}\sigma_u^2\Delta t^2)I_{3\times3} \\ -(\frac{1}{2}\sigma_u^2\Delta t^2)I_{3\times3} & (\sigma_u^2\Delta t)I_{3\times3} \end{bmatrix}$ $\hat{\mathbf{q}}_k^- = \left\{ \cos(\frac{\Delta\hat{\boldsymbol{\omega}}_k^-}{2})I_{4\times4} + \sin(\frac{\Delta\hat{\boldsymbol{\omega}}_k^-}{2}) \begin{bmatrix} -[\hat{\mathbf{e}}_k^-\times] & \hat{\mathbf{e}}_k^- \\ -[\hat{\mathbf{e}}_k^-]^\intercal & 0 \end{bmatrix} \right\}\hat{\mathbf{q}}_{k-1}^+$ $\hat{\boldsymbol{\beta}}_k^- = \hat{\boldsymbol{\beta}}_{k-1}^+$ $P_k^- = Q_k P_{k-1}^+ Q_k^\intercal + G_k Q_k G_k^\intercal$
Measurement update	$K_k = P_k^- H_k^\intercal(\hat{\mathbf{x}}_k^-)[H_k(\hat{\mathbf{x}}_k^-)P_k^- H_k^\intercal(\hat{\mathbf{x}}_k^-) + R]^{-1}$ $H_k(\hat{\mathbf{x}}_k^-) = \begin{bmatrix} [C_{BR}(\hat{\boldsymbol{q}}^-)\boldsymbol{r}_1^\times] & 0_{3\times3} \\ [C_{BR}(\hat{\boldsymbol{q}}^-)\boldsymbol{r}_2^\times] & 0_{3\times3} \\ \vdots & \vdots \\ [C_{BR}(\hat{\boldsymbol{q}}^-)\boldsymbol{r}_n^\times] & 0_{3\times3} \end{bmatrix}_{tk}$ $\boldsymbol{\delta}\hat{\mathbf{x}}_k^+ \equiv \begin{bmatrix} \boldsymbol{\delta}\hat{\boldsymbol{\alpha}}_k^+ \\ \boldsymbol{\delta}\hat{\boldsymbol{\beta}}_k^+ \end{bmatrix} = K_k[\mathbf{z}_k - \mathbf{h}_k(\hat{\mathbf{x}}_k^-)] \quad \text{where}$ $\mathbf{h}_k(\hat{\mathbf{x}}_k^-) = \begin{bmatrix} C_{BR}(\hat{\boldsymbol{q}}^-)\boldsymbol{r}_1 \\ C_{BR}(\hat{\boldsymbol{q}}^-)\boldsymbol{r}_2 \\ \vdots \\ C_{BR}(\hat{\boldsymbol{q}}^-)\boldsymbol{r}_n \end{bmatrix}_{tk}$ $\hat{\boldsymbol{\beta}}_k^+ = \hat{\boldsymbol{\beta}}_k^- + \Delta\hat{\boldsymbol{\beta}}_k^+$ $\hat{\mathbf{q}}_k^+ = \hat{\mathbf{q}}_k^- + \frac{1}{2}\Xi(\hat{\mathbf{q}}_k^-)\boldsymbol{\delta}\hat{\boldsymbol{\alpha}}_k^+$ $P_k^+ = [I - K_k H_k(\hat{\mathbf{x}}_k^-)]P_k^-$

CHAPTER 4

INTEGRATED ATTITUDE ESTIMATION ALGORITHM

In this chapter, the integrated attitude estimation algorithm, which is designed based on a MEKF, is presented. As discussed in Section 3.3.3, MEKF consists of two recursive steps: System process update and measurement update. System process update is the step in which attitude quaternions are propagated by using angular velocity measurements that are coming from the gyroscopes in linearised kinematic equations of the satellite.

The proposed integrated attitude estimation algorithm combines coarse attitude information, that is estimated by QUEST method in which Sun sensor and magnetometer measurements are utilized, with the attitude determined by the help of Earth images taken by on board camera in measurement update step of the filter. The filter is designed regarding the assumption that the vision based attitude can be determined with lesser sampling rate and only few times per orbital period for most of the time. Therefore, vision based attitude information can not be determined at each measurement update of the filter.

The vision based attitude determination algorithm is introduced in Section 4.1. This algorithm consists of three steps; First, edge of the Earth needs to be detected from the image taken by the satellite's camera. Next, fitting an ellipse to the set of points obtained by edge detection is required. After fitting the ellipse, 3-axis attitude is obtained by using this ellipse, and ellipsoid shape of the Earth. The integration of the obtained attitude with the designed MEKF is discussed in Section 4.2.

4.1 Vision Based Attitude Determination

Vision based attitude determination method is summarised in four steps as shown in Figure 4.1:

1. Taking an image of the Earth with the satellite's on-board camera.
2. Detecting edges of the Earth image.
3. Fitting an ellipse to the detected points on the image.
4. Calculating 3-axis attitude by means of perspective geometry rules and the SVD method.

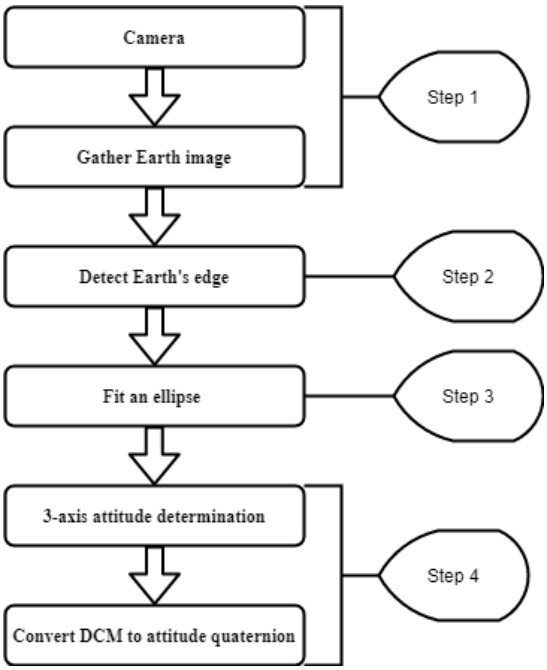

Figure 4.1: Vision based attitude determination algorithm

4.1.1 Earth Edge Detection

Shrivakshan and Chandrasekar [61] compare different edge detection techniques such as Canny, LoG, Sobel, Prewitt and Rober's edge detection methods and conclude that although Canny edge detection method's computational load is higher than the others,

it has the best performance on detecting edges at noisy images. Considering the space environment and distance of the satellite to the Earth, Canny edge detection technique is preferred because the accurate edge detection is vital for determining the attitude accurately.

Canny algorithm is a computational approach to edge detection that improves the consistency of the detected edge in three basic criteria; first criteria is good detection. This methods aims to prevent not only detecting false points as edge but also skipping real edge points. Second criteria is good localization that aims to position the edge as close as to the real edge's center and detect the edge with a one pixel width. Third criteria is finding one response to a single edge which avoids multiple responses for each point of the edge [62].

Canny edge detection method consists of four steps:

1. **Convert image to grayscale and apply Gaussian filter (blur):** Before starting the edge detection process image should be converted to a 8-bit grayscale image in which intensity of each pixel represents amount of light in the pixel. Pixel intensity of an 8-bit grayscale image can vary between 0 (black) to 255 (white).

   Gaussian filter basically blurs the image to decrease noise in the image. A 2-D Gaussian function is defined as follows:

$$G(x, y) = \frac{1}{2\pi\sigma^2} e^{-\frac{x^2+y^2}{2\sigma^2}} \tag{4.1}$$

   where σ is the standard deviation. Since the image consists of discrete pixels, this 2-D distribution function is required to be converted to a discrete approximation of the Gaussian function. An example to discrete approximate 3×3 Gaussian function with a standard deviation of 1 is given in Eq. (4.2).

$$G(x, y) \approx \frac{1}{16} \begin{array}{|c|c|c|} \hline 1 & 2 & 1 \\ \hline 2 & 4 & 2 \\ \hline 1 & 2 & 1 \\ \hline \end{array} \tag{4.2}$$

   Gaussian filtering is applied on a image by convolution operator which is illustrated in Figure 4.2. The array at the left hand side of the figure is considered to

be a grayscale image. The small array in the middle of the figure is a discrete approximate Gaussian function which is also called kernel for convolution operation. The right most array is the output image array which is produced by convolution operator. The convolution is applied by sliding the kernel over the input image array in both x and y directions. The corners and borders of the image may be ignored or calculated by accepting the elements of kernel outside the image as zero [63].

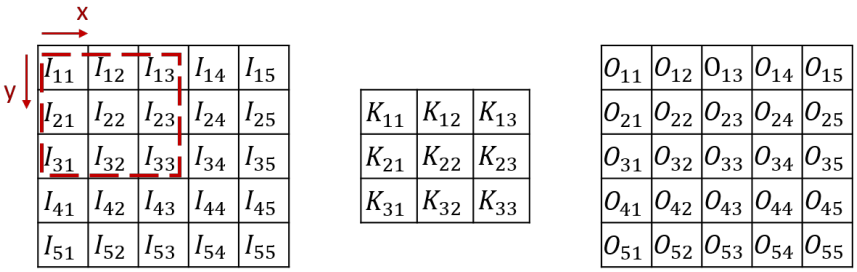

Figure 4.2: Illustration of convolution operator

The mathematical expression of the convolution is given in Eq. (4.3).

$$O(i,j) = \sum_{k=1}^{3}\sum_{l=1}^{3} I(i+k-2, j+l-2)K(k,l) \tag{4.3}$$

2. **Perform 2-D spatial gradient measurement on the image:** A 2-D first derivative operator similar to the one used in Sobel operator is performed on the image to highlight regions with high spatial frequency where edge generate ridges on the calculated gradients [64]. This operation may be carried out with the convolution kernels given below in Eq. (4.4a). While G_x is detecting edges on x direction, G_y detects edges on y direction. Calculated gradients are combined to calculate absolute magnitude of the gradient as in Eq. (4.4b). Also the orientation of the edge is found with help of Eq. (4.4c). The orientation of the edge is important to decrease the width of the edge in a one pixel wide at the next

step of the Canny edge detection method.

$$\underbrace{\begin{array}{|c|c|c|}\hline -1 & 0 & 1 \\ \hline -2 & 0 & 2 \\ \hline -1 & 0 & 1 \\ \hline \end{array}}_{G_x} \quad \underbrace{\begin{array}{|c|c|c|}\hline 1 & 2 & 1 \\ \hline 0 & 0 & 0 \\ \hline -1 & -2 & -1 \\ \hline \end{array}}_{G_y} \tag{4.4a}$$

$$|G| = \sqrt{G_x^2 + G_y^2} \tag{4.4b}$$

$$\theta = \arctan(\frac{G_y}{G_x}) \tag{4.4c}$$

3. **Non-maximal suppression:** At this step method tracks along the ridges calculated at previous step and assigns the pixels with the highest absolute magnitude of gradient as edge candidate. The neighbour pixels with lower gradient of the candidates are eliminated if they are not on the orientation of the edge found in previous step. Thus, the edge is aimed to be a thin edge that is one pixel wide.

4. **Hysteresis Threshold:** At the end, a two-level threshold is applied to inspect eliminated pixels and the final edge detection is formed. The Canny algorithm works with two thresholds: a lower one T_1 and a higher one T_2 as shown in Figure 4.3. A pixel with a greater absolute magnitude of gradient than the larger threshold T_2 is considered as an edge and shown with green color in Figure 4.3. But, a pixel with a smaller absolute magnitude of gradient than the lower threshold T_1 is eliminated and these pixels are represented with red color in Figure 4.3. For pixels whose absolute magnitude of gradient is between two thresholds (blue area in Figure 4.3), neighbour pixels are checked. In neighbour pixels, if there is a pixel with greater absolute magnitude of gradient than the large threshold T_2, also this pixel is considered as an edge, otherwise it is not an edge. According to Figure 4.3, pixels 7 and 16, which are in blue area, are neighbour pixels of 8 and 15, which are in green area. Therefore, these pixels are the only pixels, which are considered as edges, in blue area.

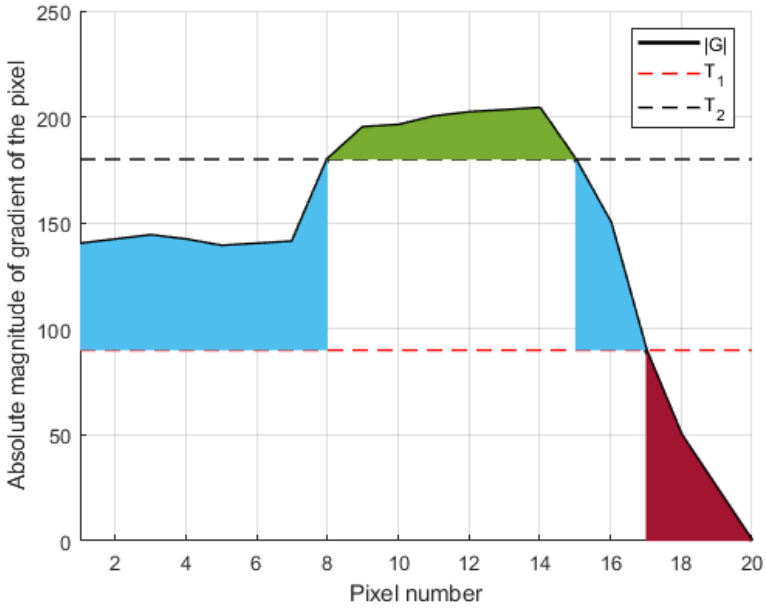

Figure 4.3: Implementation of two-level threshold

Figure 4.4 demonstrates a detected Earth limb using Canny edge detection method. On the left hand side of the figure there is a synthetically created Earth image. Besides, on the right hand side of the figure set of points detected using Canny method is shown. It is obvious that Canny method can provide a continuous and smooth Earth limb.

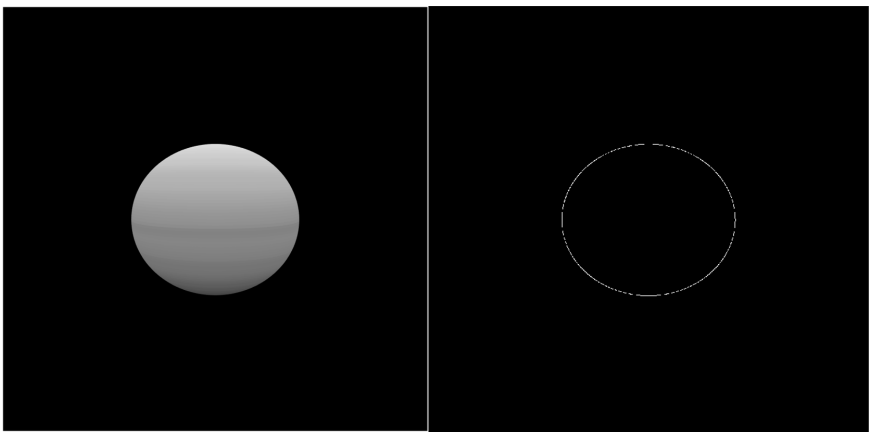

Figure 4.4: Edge detection for the Earth image

4.1.2 Ellipse Fitting

Conics and quadrics are introduced in Section 2.4.4. It is mentioned that when a quadric is photographed, a conic shape appears on the image frame. For a more specific case if a picture of ellipsoid is taken, an ellipse is the shape appears on the image frame as seen in Figure 4.4. Conics are defined with the quadric equation given in Eq. (2.34). In case the coefficients of this equation is written in vector form as $\boldsymbol{\theta} = [a, b, c, d, e, f]^\intercal$, Eq. (2.34) becomes:

$$F(\boldsymbol{\theta}, \mathbf{x}) = \boldsymbol{\theta}^\intercal \mathbf{x} = 0 \quad \text{where} \quad \mathbf{x} = [x^2, xy, y^2, x, y, 1]^\intercal \tag{4.5}$$

$F(\boldsymbol{\theta}, \mathbf{x}_i)$ represents distance between a point with coordinates (x,y) and a conic $F(\boldsymbol{\theta}, \mathbf{x}) = 0$. The conic fitting problem is based on minimizing the below cost function which is indeed summation of square of distances between n data points and conic [65]:

$$D_A(\boldsymbol{\theta}) = \sum_{i=1}^{n} F(\boldsymbol{\theta}, \mathbf{x})^2 \tag{4.6}$$

Fitzgibbon et al. [65] developed *Direct Ellipse Fitting method(DEFM)* which specifically focuses on fitting ellipses not conics. Besides, different than previous methods it is not solving the Eq. (4.6) numerically. Thus, this method is computationally more efficient and more robust compared to the previously developed methods. Fitted ellipse by the DEFM to the detected Earth edge is shown in Figure 4.5. It may be deduced from the figure that the DEFM can fit an ellipse to the data points detected by edge detection successfully.

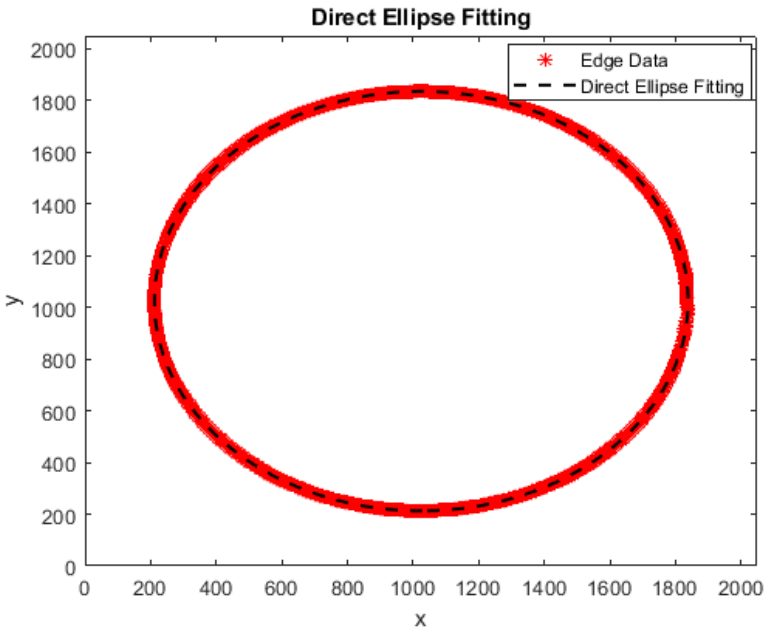

Figure 4.5: Fitted ellipse by the DEFM to the points detected by edge detection

Another ellipse fitting method is the *Guaranteed Ellipse Fitting method(GEFM)* developed in 2015 [66]. This method accepts the results of the DEFM as the initial guess and aims to make the results more consistent by using the approximate maximum likelihood method recursively with a small additional computational load. Furthermore, this method is tested with set of points detected by Canny method on Martian moon's images and fitted ellipse by this method is accurate enough to determine shape of the Martian moon. Thanks to its applicability on celestial objects, GEFM is selected as the ellipse fitting method for the proposed attitude determination algorithm. An example for the fitted ellipse to determine the Earth limb by the GEFM is given in Figure 4.6. From the figure, it is also obvious that the GEFM can fit an ellipse to the data points detected by edge detection successfully. The effect of the ellipse fitting method to resultant attitude is discussed in Chapter 6.

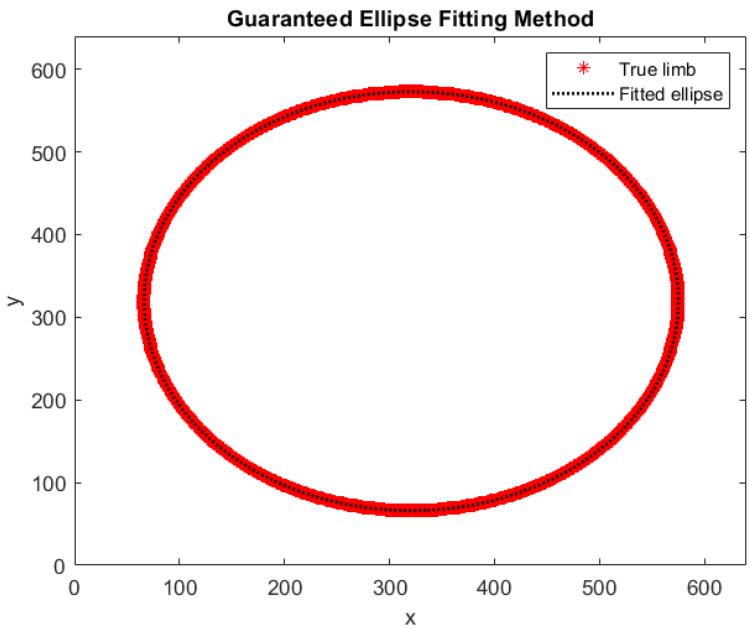

Figure 4.6: Fitted ellipse by the GEFM to the points detected by edge detection

4.1.3 Attitude Determination from Full Ellipsoid

A vision based attitude determination method, which is actually a modified orthogonal procrustes problem, is developed by Modenini in 2018 [67]. Method aims to determine nadir direction (pitch and roll angles) and obtain the rotation angle about nadir (yaw angle) when the shape of the target and position of the camera is known. As discussed before, reference sensors such as Sun sensor or magnetometer can provide attitude in 2-axis at an instant. Since Euler angles has three independent variables at least two different sensor measurements are required to obtain 3-axis attitude. But this method can determine 3-axis attitude by only limb fitting to the taken image since the vision-based attitude determination method provides the rotation angle about nadir as well. Nevertheless, estimated attitude might be coarse when the reference celestial object has a pretty low oblateness. It is not possible to detect the rotation angle about nadir in case the satellite is orbiting a planet which has a totally spherical shape.

This method is essentially derived from the equations of projecting an ellipsoid (quadric) to an ellipse (conic) under the perspective geometry rules. Projection of an ellipsoid

to an ellipse is discussed in Section 2.4.4 briefly. The projection may be achieved with formula given in Eq. (2.41). This equation is the projection of the quadric matrix Q defined in Eq. (2.42) to conic matrix E defined in Eq. (2.37). However Eq. (2.41) is only true when both ellipsoid and ellipse is expressed in same reference frame. But the semi axis of the Earth in Q is only constant when it is defined in ECI frame. Therefore, projection from ellipsoid to ellipse is need to be made by taking translation and rotation between two reference frames into account. Let's define this translational and rotational transform together in one parameter such as:

$$P = C_{BI} \begin{bmatrix} I_{3\times3} & \vec{\mathbf{R}}_I \end{bmatrix} \tag{4.7}$$

where P represents rotational and translational transform parameter, C_{BI} is the attitude matrix from ECI frame to body reference frame and R_I is the position vector of the satellite. Thus, camera is assumed to be at the same position with the satellite and camera frame is assumed to be aligned with the satellite's body reference frame. Substituting Eq. (4.7) into Eq. (2.41) yields:

$$E^* \approx K_{cam} P Q^* P^\intercal K_{cam}^\intercal \tag{4.8}$$

To reduce the complexity of the Eq. (4.8), a new matrix E_{new} is defined as:

$$E_{new} = K_{cam}^{-1} E^* K_{cam}^{-\intercal} \quad \text{where} \tag{4.9a}$$

$$K_{cam} = \begin{bmatrix} f & 0 & p_x \\ 0 & f & p_y \\ 0 & 0 & 1 \end{bmatrix} \tag{4.9b}$$

since all the parameters in the camera calibration matrix K_{cam} are constant, defining the new matrix E_{new} reduces parameters for the future calculations. Matrix E consists of the coefficients of the ellipse that appears on the image plane from projection of the reference ellipsoid as defined in Eq.(2.37). Since the ellipse equation given in Eq.(2.35) is a homogeneous equation, the ellipse would be the same ellipse even its all

parameters are multiplied with the same scale factor. Therefore, it is required to define a scale factor α since the projection is made with the homogeneous coordinates:

$$\alpha E_{new} = PQ^{*}P^{\intercal} \tag{4.10}$$

If the translational and rotational parts are separated in the defined parameter P, Eq. (4.10) becomes:

$$\alpha E_{new} = C_{BI}BC_{BI}^{\intercal} \tag{4.11}$$

where $B = Q_{(1:3,1:3)} - \vec{\mathbf{R}}_I\vec{\mathbf{R}}_I^{\intercal}$ is the translational transformation element between body reference frame and ECI frame. Scale factor α can be determined by taking trace of the both side of the equation:

$$\alpha = \frac{tr(B)}{tr(E_{new})} \tag{4.12}$$

It is obvious from the Eq. (4.11) that matrices B and αE_{new} are similar matrices. In order to determine attitude matrix C_{BI} spectral theorem for symmetric matrices may be helpful:

$$B = VD_BV^{\intercal} \tag{4.13a}$$

$$\alpha E_{new} = WD_{E_{new}}W^{\intercal} \tag{4.13b}$$

where V and W are 3×3 matrices consists of eigenvectors of matrices B and αE_{new} respectively. Finally, attitude matrix is computed using following equation:

$$C_{BI} = WTV^{\intercal} \tag{4.14}$$

where T represents an orthogonal matrix. There are eight different versions of matrix

T all are solution to Eq (4.14):

$$T = \begin{bmatrix} \pm 1 & 0 & 0 \\ 0 & \pm 1 & 0 \\ 0 & 0 & \pm 1 \end{bmatrix} \tag{4.15}$$

However, to generate a proper attitude matrix, determinant of the rotation matrix must be equal to 1. This constraint eliminates 4 possible T matrices. Also it is assumed that camera frame and satellite's body frame are aligned and z-axis of the camera frame points towards the Earth. This assumption means that the third diagonal element of the matrix T must be $+1$ and eliminates two of the remaining four matrices as well. The true T matrix is decided between last two matrices which are $T = diag[+1 \ +1 \ +1]$ and $T = diag[-1 \ -1 \ +1]$. Vision-based attitude determination method has two different attitude solutions for the same Earth image, since two Earth images which are taken by a camera with different orientations would be same as shown in Figure 4.7. These two different attitudes of camera are indistinguishable because of the symmetry of the ellipsoid with respect to its longitudes. The true attitude may be determined with the help of attitude history knowledge.

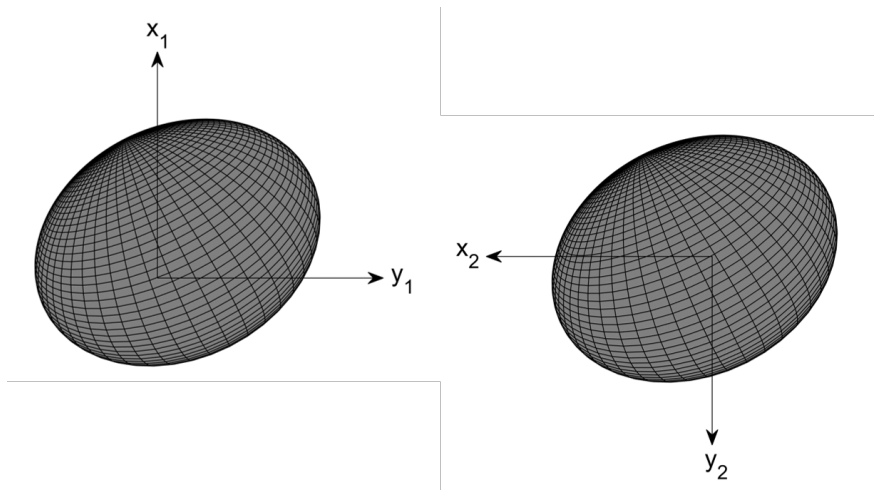

Figure 4.7: Two different Earth images which are taken by same camera with different attitudes

4.2 Integration of Vision Based Attitude Determination with Attitude Estimate Filter

The obtained attitude information is not considered as the final result and the attitude of the satellite is estimated by integrating vision-based method results with the measurements of the existing magnetometer, sun sensor and gyroscope within the algorithm proposed in Figure 4.8. This integration is necessary as it is foreseen that the vision-based attitude determination cannot provide continuous attitude information throughout the entire mission, given the calculation time and image inaccessibility. In space environment, it is always possible that image taken by satellite's camera is not proper to determine attitude. Besides, vision-based attitude determination method fails to determine accurate attitude about yaw angle when the latitude of the satellite is close to the poles.

The proposed algorithm given in Figure 4.8 integrates the camera block with the conventional attitude block to overcome continuous attitude problem of the vision-based attitude determination method. While conventional attitude block which consists of magnetometers, sun sensors and gyroscopes is ensuring the continuity of 3-axis attitude information, vision-based attitude that is coming from camera block aids the coarse attitude to increase its accuracy.

The system process update step is not different than the MEKF introduced in Section 3.3.3. Attitude is propagated using gyroscope measurement at each step of the filter. The only difference between the two filters is the measurement update step. Additional to the attitude quaternion determined by pre-processing of the magnetometer and Sun sensor measurements in QUEST method, vision-based attitude coming from camera block is fed to measurement updates of the MEKF whenever attitude measurements of the camera block is available to use. The filter is designed with the expectation that several attitude measurements will come from the camera block during one orbital period. Since both the conventional attitude determination block (QUEST method) and vision-based attitude determination method produce attitude in quaternions there is no need to change the structure of the filter. Same equations given for the measurement update step of the filter in Table 3.3 is used. But unlike that filtering algorithm, both reference sensor measurements pre-processed in QUEST method at

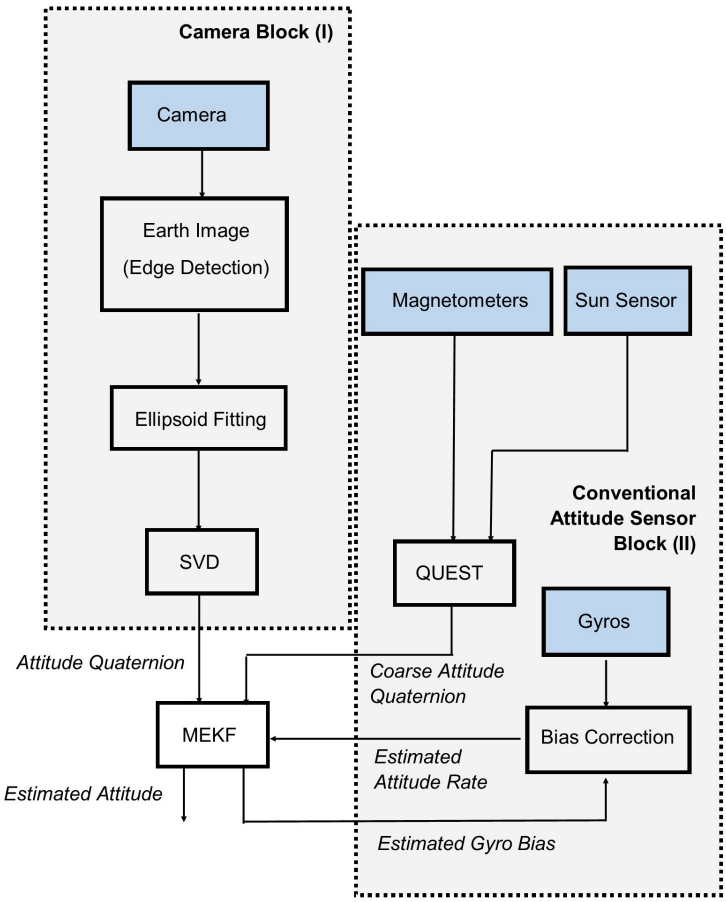

Figure 4.8: Integrated attitude estimation algorithm

the conventional attitude sensor block and attitude determined at camera block yields attitude in quaternions. So that the measurement update part of the filter becomes linear. The sensitivity matrix and calculation of Euler angle error states are changed to:

$$H_k(\bar{\mathbf{x}}_k^-) = \begin{bmatrix} 1 & 0 & 0 & 0 & 0 & 0 \\ 0 & 1 & 0 & 0 & 0 & 0 \\ 0 & 0 & 1 & 0 & 0 & 0 \end{bmatrix} \tag{4.16a}$$

$$\boldsymbol{\delta\hat{\alpha}}_k^+ = \frac{\mathbf{2}\boldsymbol{\delta\vec{q}}}{\delta q_4} \tag{4.16b}$$

CHAPTER 5

SIMULATION AND RESULTS

This chapter consists of three sections. In the first section how the synthetic Earth images are generated is explained. In Section 5.2, results of vision based attitude determination algorithm for different latitudes and longitudes are given and discussed. Results of vision based attitude determination algorithm for images with different pixel numbers, and in which different ellipse fitting methods are utilized, are tabulated and discussed. Also, vision based attitude determination algorithm is tested with blurred images to show how the effect of the Earth atmosphere may deteriorate the determined attitude. In Section 5.3, simulations depending on four different scenarios for the same hypothetical satellite are performed. These simulations are performed to test the proposed integrated attitude estimation algorithm in a Sun synchronous orbit, in an orbit with a higher altitude and in an orbit with lower inclination.

5.1 Creating Synthetic Earth Images

In order to test the integrated algorithm that calculates attitude in the camera block, an ellipsoid with the same dimensions of the Earth ($6378.1km$ semi-major axis and $6356.8km$ semi-minor axis) is generated. Afterwards, photographs of this Earth like ellipsoid are taken, assuming the camera is at a distance to see the entire limb of the Earth. Although FOV of a pinhole camera may not be enough to fit the entire Earth limb in the taken image, the proposed method in [21] allows one to set FOV of the camera up to 180° by using a panoramic annular lens. In this thesis images are assumed to be taken by a LEO small satellite with a field of view 140°.

The position in a reference frame, orientation and FOV of a hypothetical camera can

be adjusted in the Matlab scene control tool. Therefore, synthetic images may be created which are considered to be taken from the desired location and with the desired orientation by the camera of the hypothetical satellites. Examples of the photos created are given in Figure 5.1. While the left hand side images are assumed to be taken by a hypothetical satellite at $612km$ altitude, the right hand side images are assumed to be taken by a hypothetical satellite at $956.82km$ altitude. Attitude of the satellite in Euler angles are given in the each image.

As mentioned above; position, attitude and FOV of the camera can be adjusted in Matlab scene control tool. However, the vision-based attitude determination method works with projection of a quadric to a conic which may be done with the focal length. Focal length may be found using the size of the image and FOV of the camera. An image taken by a camera is demonstrated in Figure 5.2. It is obvious that that half of the size of the image S divided by the focal length f is equal to tangent of half of the field of view α. Using this relationship, focal length in pixels is calculated as:

$$\tan(\frac{\alpha}{2}) = \frac{\frac{S}{2}}{f} \tag{5.1a}$$

$$f = \frac{\frac{S}{2}}{\tan(\frac{\alpha}{2})} \tag{5.1b}$$

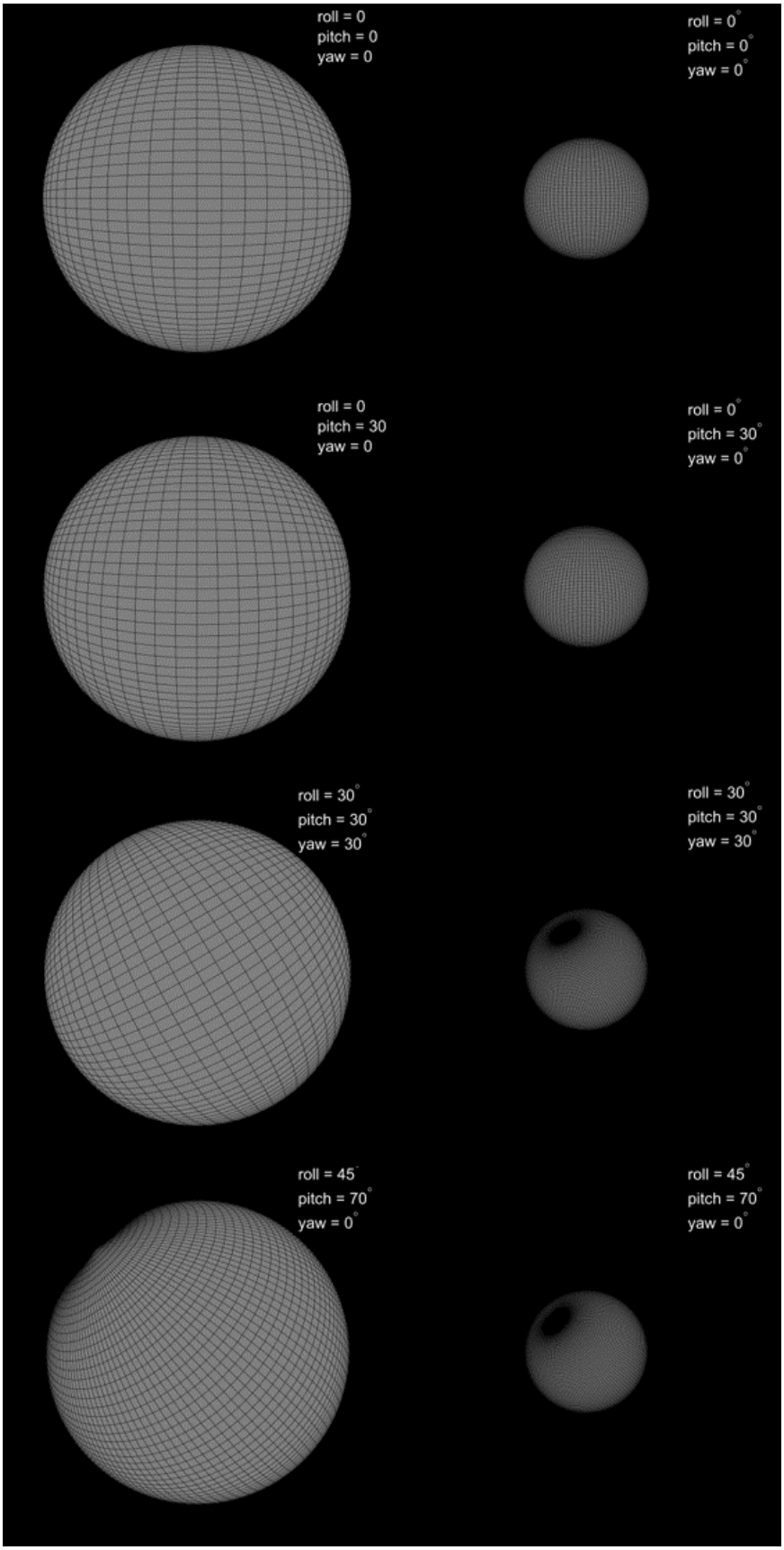

Figure 5.1: Synthetically created Earth images

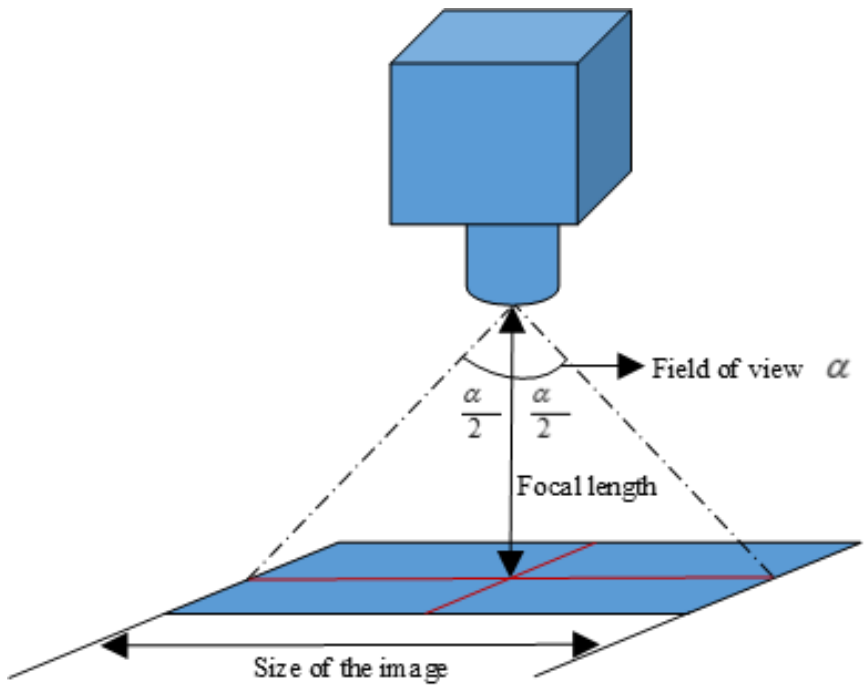

Figure 5.2: Relationship between focal length, FOV and image size (resolution)

5.2 Results of Vision Based Attitude Determination Algorithm

Vision-based attitude determination method is tested with synthetically created images using the MATLAB 3-D scenes control tool. Images are generated at different latitudes and longitudes. While latitude ranging from 0° to 80° with 20° angular steps, longitude is ranging from from 0° to 90° with 10° angle intervals. Errors of obtained Euler angles by vision based attitude determination algorithm are given in Table 5.1. The error corresponding to each latitude in the table is the average of the error of the angles extracted from 10 different images obtained by increasing the longitude from 0° to 90° by 10° at that latitude. On the other hand, a total Euler angle error is calculated with the formula given below and is tabulated in Table 5.1.

$$Error = 2\sin^{-1}\left(\frac{\|C_{BRtrue} - C_{BRobtained}\|_F}{\sqrt{8}}\right) \tag{5.2}$$

It may be deduced from Table 5.1 that due to the shape of the Earth, the error in the

yaw angle increases as the latitude increases towards the poles. The main reason for this is that the photograph taken converges to the circle rather than ellipse on the image plane and consequently the yaw angle cannot be determined from the photograph. A general interpretation can be made that the method gives the most sensitive result between 0° to 40° latitude.

Table 5.1: Errors of the Euler angles determined using vision-based attitude determination method

	Pitch [°]	**Roll [°]**	**Yaw [°]**	**Error [°]**
0°	0.003	0.71	0.75	1.03
20°	0.11	0.36	0.29	0.46
40°	0.17	0.18	0.35	0.40
60°	0.37	0.41	0.78	0.91
80°	0.05	0.22	1.18	1.14

5.2.1 Number of Pixel Effect

In order to test how image's number of pixel effects the attitude obtained by using the vision based attitude determination method, images are created with latitude ranging from 0° to 80° with 20° angular steps and longitude ranging from from 0° to 90° with 10° angle intervals. This process is repeated three times for images with pixel number of 512×512, 1024×1024 and 2048×2048. The average of the errors in terms of Euler angles of the attitude from the images that are generated at ten different longitudes for the relevant latitude is shown in the Table 5.2. The table involves the average Euler angle errors and total attitude error calculated using Eq. (5.2), for images generated with three different pixel numbers. Although images with 512×512 and 1024×1024 pixels may give better results in some latitudes for one of the Euler angles, when the total error in 3 axes is checked, the photos with 2048×2048 pixels provide more accurate attitude results compared to the others. Therefore, these images are used in the simulations of the integrated attitude determination algorithm for hypothetical satellites.

Table 5.2: Errors of the Euler angles obtained from images with different pixel sizes

	512×512				1024×1024				2048×2048			
	Pitch [°]	**Roll [°]**	**Yaw [°]**	**Error [°]**	**Pitch [°]**	**Roll [°]**	**Yaw [°]**	**Error [°]**	**Pitch [°]**	**Roll [°]**	**Yaw [°]**	**Error [°]**
0°	7.69	0.13	2.01	7.44	0.49	1.87	2.67	2.86	0.003	0.71	0.75	1.03
20°	0.70	0.64	0.50	1.03	0.55	0.25	0.17	0.57	0.11	0.36	0.29	0.46
40°	0.16	0.60	1.07	1.14	1,71	0.21	0.002	1.72	0.17	0.18	0.35	0.40
60°	3.09	3.70	9.26	10.31	2,83	0.57	6.63	6.87	0.37	0.41	0.78	0.91
80°	0.06	0.25	14.93	14.9	3.10	1.26	7.67	8.02	0.05	0.22	1.18	1.14

5.2.2 Ellipse Fitting Method Effect

The DEFM and GEFM are applied to the detected data points by Canny edge detection from Earth images with 2048×2048 pixels. Images are created with latitude ranging from 0° to 80° with 20° angular steps and longitude ranging from from 0° to 90° with 10° angular steps. Two ellipse fitting methods applied separately while determining attitude and the results are tabulated in Table 5.3. Results in the table indicate that using GEFM in vision based attitude determination method instead of DEFM allows one to determine more accurate 3-axis attitude.

Table 5.3: Errors of the Euler angles obtained by using different ellipse fitting methods

	DEFM				GEFM			
	Pitch [°]	**Roll [°]**	**Yaw [°]**	**Error [°]**	**Pitch [°]**	**Roll [°]**	**Yaw [°]**	**Error [°]**
0°	0.33	1.20	1.25	1.72	0.003	0.71	0.75	1.03
20°	0.67	0.60	0.52	1.03	0.11	0.36	0.29	0.46
40°	0.67	0.68	0.86	1.29	0.17	0.18	0.35	0.40
60°	0.64	1.02	1.65	2	0.37	0.41	0.78	0.91
80°	0.55	0.63	1.30	1.54	0.05	0.22	1.18	1.14

5.2.3 Blurred Image Effect

The Earth's atmosphere misleads the edge detection algorithms at the edges of the Earth in an image taken by the camera on the satellite. This misleading effect can be minimized by using infra-red cameras, especially for he horizon sensors. Blurred images with 2 standard deviations are created in order to observe the effect of the

atmosphere on the determined attitude if an infra-red camera is not used. Images are created with latitudes ranging from 0° to 80° with 20° angular steps and longitudes ranging from from 0° to 90° with 10° angular steps. Euler angle error and total attitude error for both blurred and non-blurred images are given in Table 5.4. It is obvious that blurring images decreases the accuracy of the determined attitude. However, determined attitude can still fulfil most of the attitude accuracy requirements for small satellite missions up to 40° latitude.

Table 5.4: Errors of the Euler angles determined from blurred images and non-blurred images

	Blurred Images				**Non-blurred Images**			
	Pitch [°]	**Roll [°]**	**Yaw [°]**	**Error [°]**	**Pitch [°]**	**Roll [°]**	**Yaw [°]**	**Error [°]**
0°	0.18	0.41	0.42	0.57	0.003	0.71	0.75	1.03
20°	0.10	0.69	0.79	1.03	0.11	0.36	0.29	0.46
40°	0.58	0.44	0.39	0.80	0.17	0.18	0.35	0.40
60°	2.03	0.28	0.3	2.06	0.37	0.41	0.78	0.91
80°	2.04	0.24	1.24	2.34	0.05	0.22	1.18	1.14

5.3 Integrated Attitude Estimations Filter Results

The proposed integrated attitude determination algorithm is simulated for four different scenarios in this section. In all scenarios, it is assumed that the vision-based attitude is available when the satellite is close to the equator crossings. Grey areas in the all simulation figures indicate that satellite is in eclipse where the Sun sensor cannot provide measurement. When the satellite is not in eclipse, the filter accepts the output of the QUEST method, which is produced by utilizing magnetometer and Sun sensor measurements, as a measurement update, while the system emits the attitude quaternion with gyroscope measurements in the process update. For all simulations, initial quaternions for MEKF are considered as $\bar{\mathbf{q}}_0 = \begin{bmatrix} 0 & 0 & 0 & 1 \end{bmatrix}^\intercal$ and initial gyroscope bias is assumed to be zero. The attitude estimation errors in Euler angles and corresponding $\mp 3\sigma$ covariance bounds are shown in all simulation figures with red line and blue dashed line respectively.

The gyroscope, magnetometer and Sun sensor are modelled with the following equations in all simulations:

$$\tilde{\boldsymbol{\omega}} = \vec{\boldsymbol{\omega}} + \vec{\boldsymbol{\beta}} + \vec{\boldsymbol{\eta}}_v \tag{5.3a}$$

$$\tilde{\mathbf{B}} = \vec{\mathbf{B}} + \vec{\mathbf{b}}_m + \vec{\boldsymbol{\nu}}_m \tag{5.3b}$$

$$\tilde{\mathbf{S}} = \vec{\mathbf{S}} + \vec{\mathbf{b}}_s + \vec{\boldsymbol{\nu}}_s \tag{5.3c}$$

where $\vec{\boldsymbol{\beta}}$ and $\boldsymbol{\eta}_v$ bias vector and the Gaussian zero-mean measurement noise for gyroscope. Besides, $\vec{\mathbf{b}}_m$, $\vec{\boldsymbol{\nu}}_m$ and $\vec{\mathbf{b}}_s$, $\vec{\boldsymbol{\nu}}_s$ are the bias vector and the Gaussian zero-mean measurement noise for magnetometer and Sun sensor respectively. Noise of the magnetometer $\vec{\boldsymbol{\nu}}_m$ and Sun sensor $\vec{\boldsymbol{\nu}}_s$ are considered as a zero mean Gaussian white noise. The noise of the gyroscope $\vec{\boldsymbol{\eta}}_v$ is also assumed as Gaussian white noise but it is modelled with two parameters; first one is the angular random walk which is equal to $\sigma_v = 2.47\frac{arcsec}{\sqrt{s}}$ and second is the rate random walk with $\sigma_u = 6.36 \times 10^{-4}\frac{arcsec}{\sqrt{s}}$.

5.3.1 Scenario - 1 and Results

The hypothetical small satellite is assumed to be orbiting around the Earth on an elliptical, Sun synchronous orbit. The elliptical orbit is assumed to have 6.4×10^{-5} eccentricity, $74°$ inclination and $612km$ approximate altitude. The magnetometer noise and Sun sensor noise are assumed to have standard deviation of $300nT$ and 0.002 for unit vector measurements, respectively.

The simulation is run for $10000s$. The frequencies of the Sun sensor and magnetometer are set to $1Hz$. Vision-based attitude determination is assumed to be available two times during the simulation both are in eclipse time. The first and second updates are done at $2800^{th}s$ and $8626^{th}s$ respectively. These two moments when vision-based updates are fed into measurement update step of the filter are chosen close to equatorial plane where vision-based measurements are more consistent.

It is obvious in the Figure 5.3 that attitude is estimated with an error less than $0.5°$ in each axis without the aid of the vision-based determined attitude. Since the Sun sen-

sor measurements are not available in eclipse, propagated attitude's error increases because of the gyroscope bias. Since MEKF is modelled to estimate gyroscope bias in addition to attitude quaternions, attitude error is kept below $0.5°$. When attitude error increases to an undesired level, two vision-based attitude measurement updates are done at $2800^{th}s$ and $8626^{th}s$. From the figure it may be deduced that attitude error is decreased below $0.5°$ when these updates are available. The corrective effect due to attitude measurement is higher at the estimated angle with greater error at each measurement moment. The decrease in the estimated covariance values shown by the blue dashed line also reveals the truth of this statement. Of course, the estimation response of the filter may differ depending on the values of the process noise covariance matrix and the measurement noise covariance matrix set in the filter.

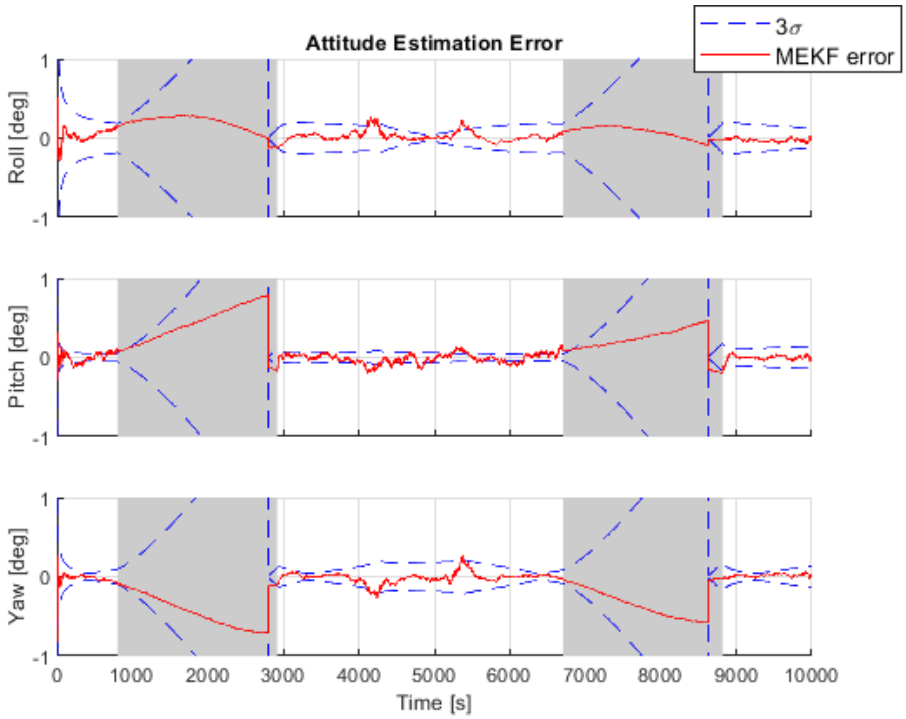

Figure 5.3: Attitude errors in Euler angles for the first scenario

5.3.2 Scenario - 2 and Results

Second scenario is generated to test vision-based attitude update performance out of the eclipse. The hypothetical small satellite is assumed to be orbiting at the same Sun synchronous orbit with the previous simulation. Unlike the first scenario, mag-

netometer measurements are corrupted with an additional noise of $\vec{\boldsymbol{\eta}}_v = 200nT$. All other parameters are kept same with the first scenario.

Different than the first scenario, it is assumed that one vision-based measurement update comes out of the eclipse at $4211^{st}s$, while the second vision-based update is done in eclipse at $8626^{th}s$. Again the two moments when vision-based updates are send to the measurement update step of the filter are chosen close to equatorial plane where vision-based measurements are more accurate.

Since the magnetometer error is increased, attitude error exceeds $1°$ during two eclipses in Figure 5.4. However, even this error is below the required error to succeed most of the small satellite tasks. In order to test the vision-based attitude update performance out of the eclipse, the first vision-based attitude measurement update is done at $4211^{st}s$ when satellite is out of the eclipse. The second vision-based measurement update is performed at $8626^{th}s$ during eclipse. It is clear that that attitude error is decreasing below $0.2°$ with these updates and brought back inside the covariance bounds. The corrective effect is higher at the estimated angle with greater error at each measurement moment. Although the decrease in the estimated covariance values which is performed by vision-based measurement update out of the eclipse shown by the blue dashed line is not high as the update done in eclipse, the first update squeezes the covariance bounds as well. Both decreasing attitude error and squeezing the covariance bounds proves that vision-based attitude updates helps to the conventional attitude determination block positively.

5.3.3 Scenario - 3 and Results

In this scenario, the hypothetical small satellite is assumed to be orbiting around the Earth on an elliptical orbit. The elliptical orbit is assumed to have 1.4×10^{-3} eccentricity, $20°$ inclination. Apogee of the orbit has an altitude of $868km$, while perigee of the orbit has an altitude of $853km$. The gyroscope, magnetometer and Sun sensor are modelled with the Eq. (5.3). The magnetometer is assumed to have a constant bias of $\vec{\mathbf{b}}_m = \begin{bmatrix} 100 & -150 & 100 \end{bmatrix}^{\mathsf{T}} nT$ and noise with a standard deviation of $200nT$. Sun sensor noise, gyroscope bias and gyroscope noise are same with the previous simulations.

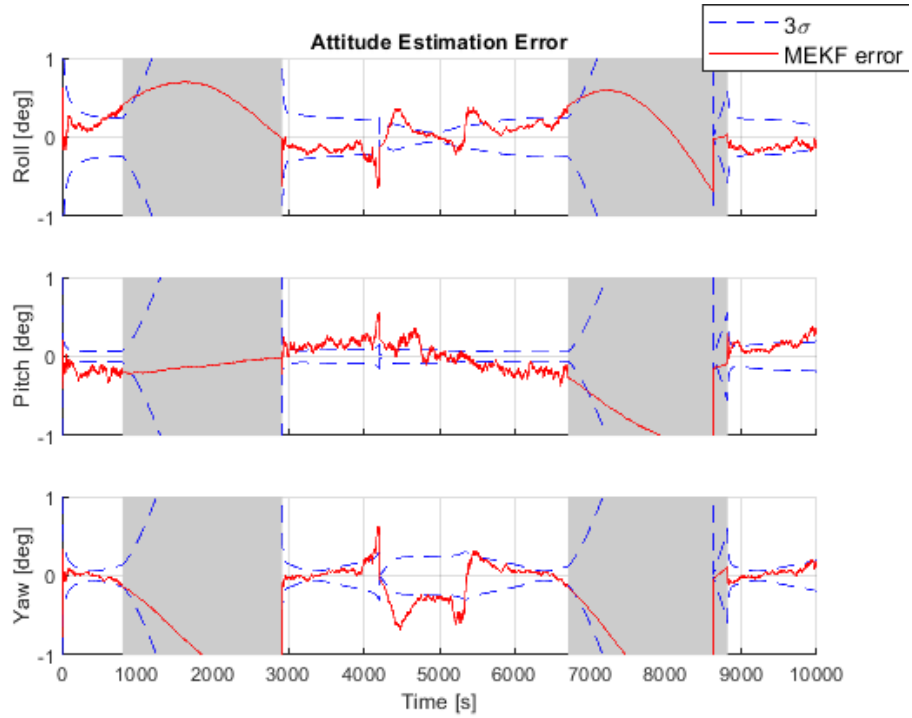

Figure 5.4: Attitude errors in Euler angles for the second scenario

The simulation is run for $12000s$. The frequencies of the Sun sensor and magnetometer are set to $1Hz$ like the previous simulations. It is assumed that two vision-based measurement updates come from camera block when the Euler angle error is high. The vision-based measurement updates are performed at $1855^{th}s$ and $4062^{nd}s$. Since the inclination of the satellite is $20°$, all vision-based attitude measurements are more consistent compared to two simulations in Section 5.3.1 and Section 5.3.2. The results of this simulation are given in Figure 5.5.

The difference between this simulation and previous ones are that hypothetical satellite's altitude is higher and a constant bias is added to the magnetometer measurements. It may be deduced from the Figure 5.5 that attitude is estimated with an error less than $0.5°$ in each axis without the aid of the vision-based determined attitude. Since MEKF is modelled to estimate gyroscope bias in addition to attitude quaternions, attitude error is kept below $0.3°$. Once vision-based attitude measurement update is performed, attitude error is decreasing below $0.2°$. The vision-based measurement update also decreases the estimated covariance values shown by the blue dashed line. Vision-based update can be repeated whenever the covariance bounds

checked for consistency tend to increase above some fixed limit.

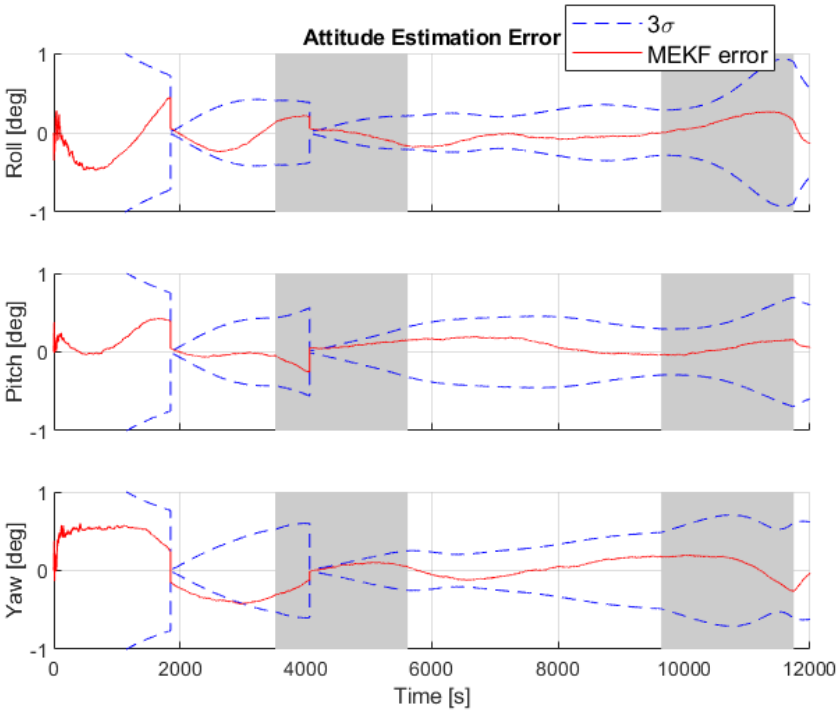

Figure 5.5: Attitude errors in Euler angles for the third scenario

5.3.4 Scenario - 4 and Results

In this scenario, another hypothetical small satellite is assumed to be orbiting around the Earth on an elliptical orbit. The elliptical orbit is assumed to have 1.21×10^{-3} eccentricity, $6°$ inclination. Apogee of the orbit has an altitude of $649km$,while perigee of the orbit has an altitude of $832km$. The sampling frequencies for the measurements, magnetometer constant bias, magnetometer noise, Sun sensor noise, gyroscope bias and gyroscope noise are kept same with the simulation in Section 5.3.3. The simulation is run for $12000s$ for five different cases.

In the first case it is assumed that four vision-based measurement updates are performed at $1475^{th}s$, $2974^{th}s$, $8644^{th}s$ and $11380^{th}s$. Results of the first case of the simulation five is shown in Figure 5.6. It may be deduced from the figure that most accurate vision-based attitude information is obtained in this scenario since the orbit of the hypothetical satellite has the lowest inclination compared to the previous

simulations. When attitude error increases to an undesired level, vision-based attitude measurement updates are done at $1475^{th}s$, $2974^{th}s$, $8644^{th}s$ and $11380^{th}s$ and attitude error is decreasing below $0.2°$. The vision-based measurement update also decreases the estimated covariance values shown by the blue dashed line.

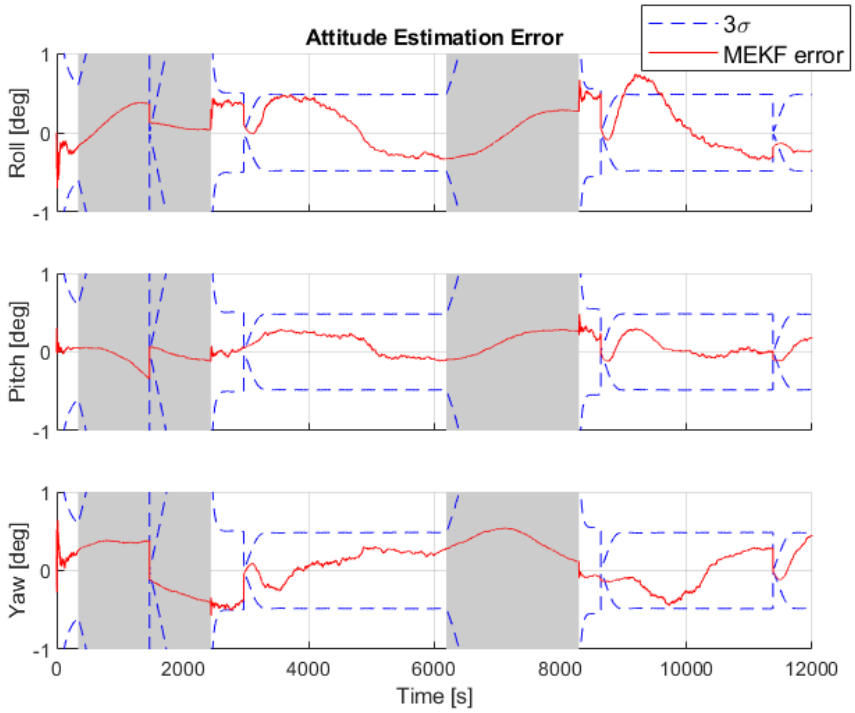

Figure 5.6: Attitude errors in Euler angles for the first case of fourth scenario

Due to the low inclination of hypothetical satellite's orbit, accurate vision-based attitude may be obtained through whole orbit. To show the effects of this, vision-based attitude measurements are obtained every $2000s$, $1000s$, $100s$ and $10s$ throughout the simulation and the results are shown in Figure 5.7, Figure 5.8, Figure 5.9 and Figure 5.10 respectively. It is obvious from the figures that in all cases attitude is estimated with an angle error less than $0.6°$ at all three axis. As stated before, because of the ellipsoid shape of the Earth, error is higher on yaw angle than pitch angle and roll angle.

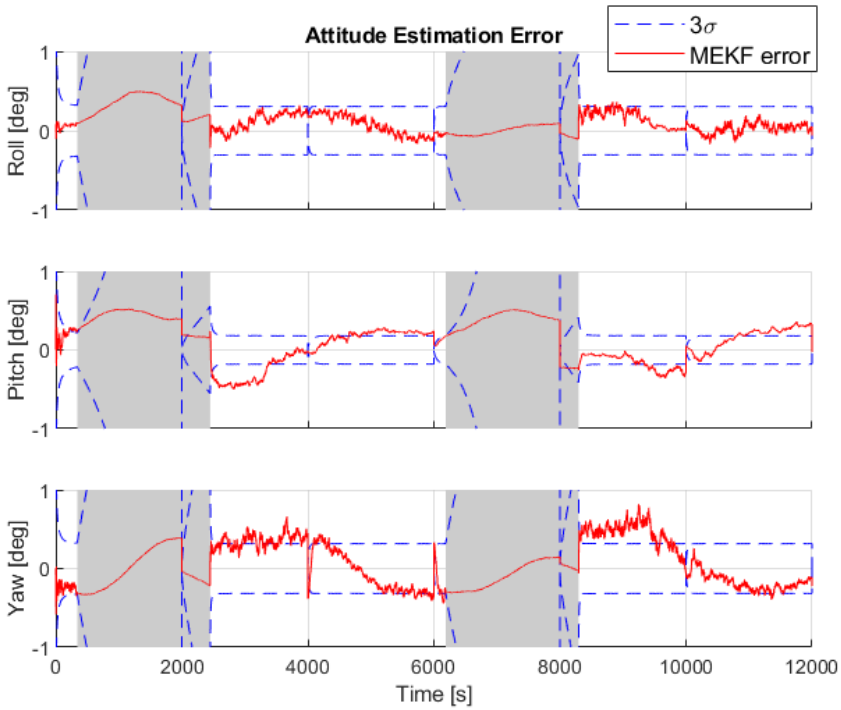

Figure 5.7: Vision-based attitude is determined with $2000s$ time intervals

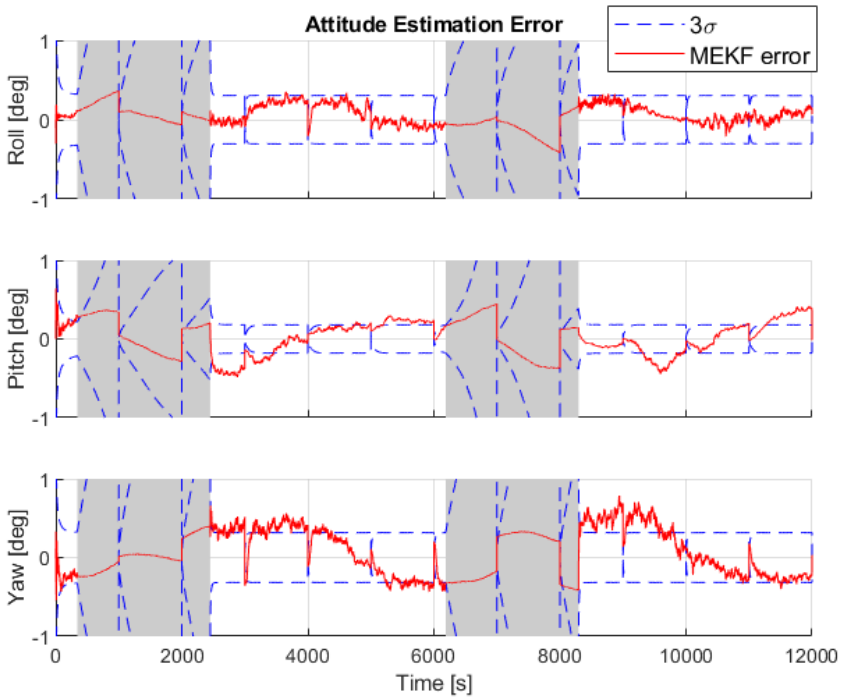

Figure 5.8: Vision-based attitude is determined with $1000s$ time intervals

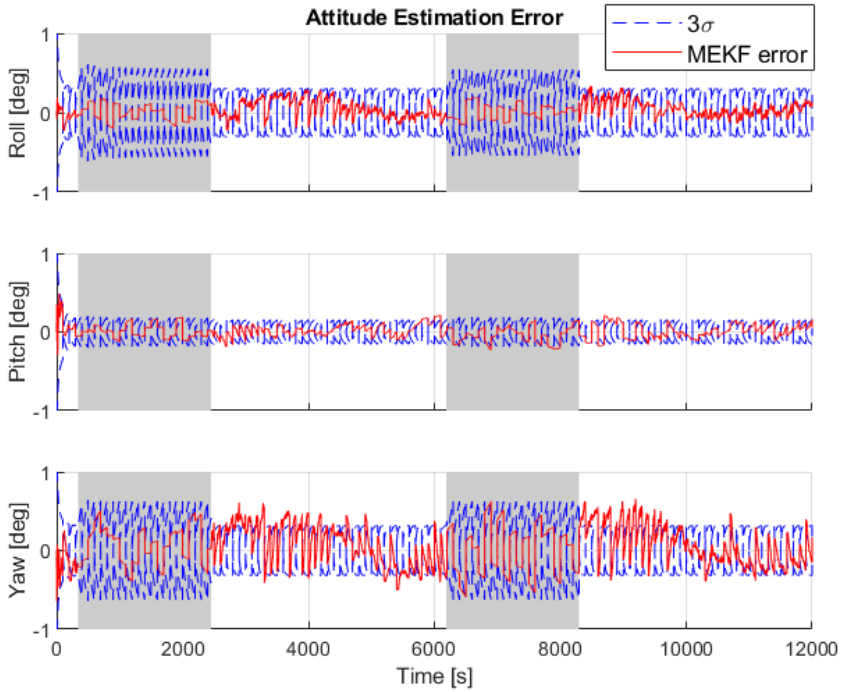

Figure 5.9: Vision-based attitude is determined with $100s$ time intervals

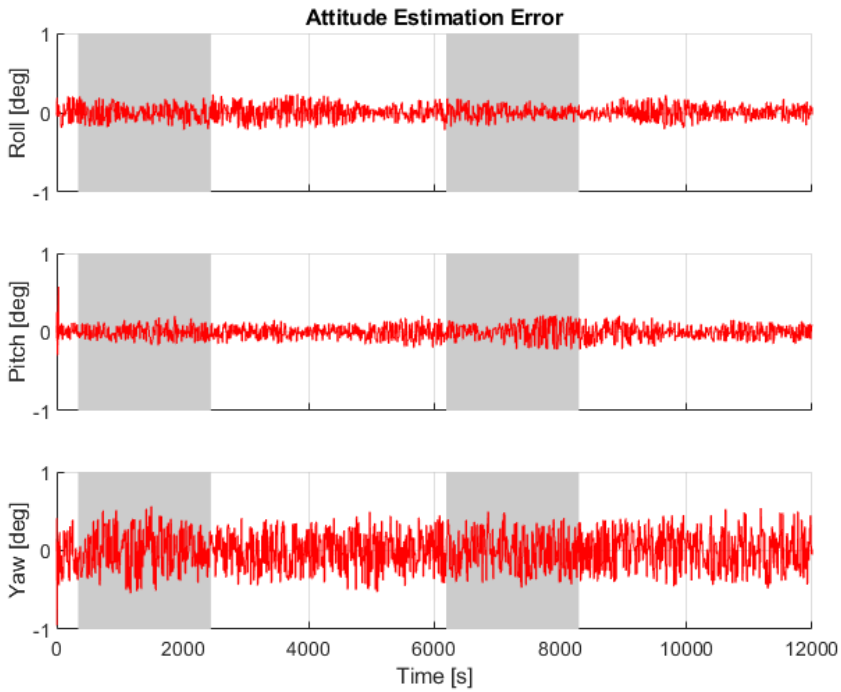

Figure 5.10: Vision-based attitude is determined with $10s$ time intervals

CHAPTER 6

CONCLUSION AND FUTURE WORK

6.1 Conclusion

In this thesis an integrated attitude estimation algorithm is proposed to obtain three-axis continuous attitude estimates for a small satellite. The algorithm combines coarse attitude estimation determined by using magnetometer and Sun sensor measurements in QUEST method with the vision-based attitude measurement coming from camera block. The camera block detects three-axis attitude from the Earth images taken by satellite's on-board camera. Since vision-based attitude measurements become more accurate at the equatorial passes, camera block measurements are utilized in the measurement update of the filter around equatorial plane. The magnetometer and Sun sensor measurements are pre-processed in QUEST method at the conventional attitude sensor block. This pre-process enables one to have attitude in quaternions for both measurements from the camera block and conventional attitude sensor block. Besides, the designed MEKF may use measurements coming from both camera block and conventional attitude sensor block without changing structure of the filter. This reduces the complexity and computational burden of the filter.

In addition to aiding coarse attitude with the vision-based attitude measurements in the MEKF, the vision-based attitude determination method is separately tested with synthetically generated Earth images for different latitudes. The results are tabulated in Table 5.1. Because of the ellipsoid shape of the Earth, three-axis attitude determination becomes impossible at the poles as the shape of the Earth at the gathered image converges to circle instead of an ellipse. It is clear from the Table 5.1 that attitude error increases especially on the yaw angle when satellite is closer to the poles.

It may also deduced from the table that the method gives the most accurate results between 0° to 40° latitude.

The number of pixels of the taken images effects the obtained attitude information. Euler angle errors of the determined attitude from images with different pixel numbers are given in Table 5.2. The detected edge by Canny method gets thinner with the increase of pixel number. Thus, the most accurate attitude is determined from images with 2048×2048 pixels.

Ellipse fitting method, used in vision-based attitude determination, effects accuracy of the attitude as well. Two methods; the DEFM and the GEFM are tested with the proposed vision-based attitude determination algorithm and results are shown in Table 5.3. The GEFM's performance is better than DEFM's performance, since GEFM takes DEFM's ellipse estimates as a initial estimate and tries to make it more accurate.

Detecting Earth limb would be harder in case a normal camera is used instead of a infra-red camera on the satellite because of the Earth atmosphere's misleading effect on the Earth limb. In order to test this misleading effect blurred images with standard deviation of 2 are generated and vision-based attitude determination method is applied on these images. Euler angle errors obtained from these images are tabulated in Table 5.4. Results indicates that errors of Euler angles becomes greater in blurred image compared to normal image, but determined attitude fulfils the requirements for most of the nano-satellite missions in terms of accuracy below 40° latitude.

The simulations of the integrated attitude estimation algorithm is done considering that vision based attitude determination method cannot provide continuous attitude measurements throughout the entire mission. Therefore, integrated attitude estimation algorithm is first tested in two scenarios with a hypothetical satellite which is on an elliptical, Sun synchronous orbit. In these simulations, vision-based attitude measurements are available only two times during the simulation duration. Results in Figure 5.3 show that proposed integrated attitude estimation algorithm estimates the attitude with an error less than $0.5°$ for the first scenario where the vision-based updates comes in eclipses. For the second scenario in Figure 5.4, where one vision-based measurement update comes in eclipse and one in out of the eclipse, integrated attitude estimation algorithm estimates the attitude with an error less than $1°$. For both

scenarios vision-based attitude measurements improve the attitude estimate accuracy despite only two measurements are provided through whole simulation duration.

The same hypothetical small satellite is simulated in an elliptical orbit with higher altitude and 20° inclination. It may be deduced from Figure 5.5 that vision-based determined attitude is more accurate in an orbit with lower inclination and higher altitude.

The final simulation is performed to test if continuous vision-based attitude measurements are available in whole orbit. An orbit with 6° inclination is chosen to test this scenario. It is obvious from the results in Section 5.3.4 that in an orbit with this inclination vision-based attitude determination method may be used continuously. However if the camera is used for continuous measurements, only one mission camera may not be enough to fulfil all duties expected from camera since satellite's on-board camera has other duties such as Earth observation.

In case the proposed integrated attitude estimation algorithm is decided to be used as attitude determination system of a small satellite, a large area and a significant budget may be saved compared to the ones with star trackers in attitude determination system.

6.2 Future Work

In the next stages of the study, instead of fitting an ellipse to the obtained image, using vertices and co-vertices may be tried to determine three axis attitude. This method allows one to reduce computational load of the algorithm. In addition, new scenarios can be added such that the camera is oriented towards other celestial objects. The applicability will be examined by testing the algorithm using the real images taken from different satellites. How the corrective effect is on the attitude with respect to the orbital reference frame may also be included in the results.

In case three-axis attitude cannot determined from the gathered Earth images, only two axis attitude may be obtained and used in QUEST method. This scenario may be combined with the one that is proposed in this thesis.

REFERENCES

[1] Martin Sweeting. Modern small satellites-changing the economics of space. *Proceedings of the IEEE*, 106(3):343–361, 2018.

[2] Gerhard Hermann Janse van Vuuren. *The design and simulation analysis of an attitude determination and control system for a small earth observation satellite*. PhD thesis, Stellenbosch: Stellenbosch University, 2015.

[3] John C Springmann and James W Cutler. Flight results of a low-cost attitude determination system. *Acta Astronautica*, 99:201–214, 2014.

[4] Andris Slavinskis, Hendrik Ehrpais, Henri Kuuste, Indrek Sünter, Jaan Viru, Johan Kütt, Erik Kulu, and Mart Noorma. Flight results of estcube-1 attitude determination system. *Journal of Aerospace Engineering*, 29(1):04015014, 2016.

[5] Stephan Busch, Philip Bangert, Slavi Dombrovski, and Klaus Schilling. Uwe-3, in-orbit performance and lessons learned of a modular and flexible satellite bus for future pico-satellite formations. *Acta Astronautica*, 117:73–89, 2015.

[6] Shinichi Nakasuka, Kikuko Miyata, Yoshihiro Tsuruda, Yoshihide Aoyanagi, and Takeshi Matsumoto. Discussions on attitude determination and control system for micro/nano/pico-satellites considering survivability based on hodoyoshi-3 and 4 experiences. *Acta Astronautica*, 145:515–527, 2018.

[7] Yohei Iwasaki, Yuhei Kikuya, Kenichi Sasaki, Toshiki Ozawa, Yusuke Shintani, Yuto Masuda, Kei Watanabe, Hideo Mamiya, Hiroki Ando, Tsuyoshi Nakashima, et al. Development and initial on-orbit performance of multi-functional attitude sensor using image recognition. In *33rd Annual AIAA/USU Conference on Samll Satellites, Utah, USA*, 2019.

[8] Sho Koizumi, Yuhei Kikuya, Kenichi Sasaki, Yuto Masuda, Yohei Iwasaki, Kei Watanabe, Yoichi Yatsu, and Saburo Matsunaga. Development of attitude sensor using deep learning. 2018.

[9] Amartuvshin Dagvasumberel and Kenichi Asami. A visual-inertial attitude propagation for resource constrained small satellites. *Journal of Aeronautics and Space Technologies*, 12(1):65–74, 2019.

[10] Yuhei Kikuya and Saburo Matunaga. On-board relative attitude determination and propagation using earth sensor. In *32nd International Symposium on Space Technology and Science, Fukui, Japan*, 2019.

[11] Gregor Klančar, Sašo Blažič, Drago Matko, and Gašper Mušič. Image-based attitude control of a remote sensing satellite. *Journal of intelligent & robotic systems*, 66(3):343–357, 2012.

[12] Toru Kouyama, Atsunori Kanemura, Soushi Kato, Nevrez Imamoglu, Tetsuya Fukuhara, and Ryosuke Nakamura. Satellite attitude determination and map projection based on robust image matching. *Remote Sensing*, 9(1):90, 2017.

[13] Jin Wu. Unified attitude determination problem from vector observations and hand–eye measurements. *IEEE Transactions on Aerospace and Electronic Systems*, 56(5):3941–3957, 2020.

[14] Samir Rawashdeh, James Lumpp Jr, James Barrington-Brown, and Massimiliano Pastena. A stellar gyroscope for small satellite attitude determination. 2012.

[15] Samir A Rawashdeh and James E Lumpp. Image-based attitude propagation for small satellites using ransac. *IEEE Transactions on Aerospace and Electronic Systems*, 50(3):1864–1875, 2014.

[16] N. Korn, F. Baumann, R. Wolf, and K. Brieß. Multifunctional optical attitude determination sensor for picosatellites. In *68th International Astronautical Congress, Adelaide, Australia*, 2017.

[17] Taeho Kim, Youngjoo Kim, and Hyochoong Bang. Improvement of the attitude determination accuracy for nanosatellites using a camera sensor. In *2017 European Navigation Conference (ENC)*, pages 341–347. IEEE, 2017.

[18] Dario Modenini and Marco Zannoni. A high accuracy horizon sensor for small satellites. In *2019 IEEE 5th International Workshop on Metrology for AeroSpace (MetroAeroSpace)*, pages 451–456. IEEE, 2019.

[19] Dario Modenini, Alfredo Locarini, and Marco Zannoni. Attitude sensor from ellipsoid observations: A numerical and experimental validation. *Sensors*, 20(2):433, 2020.

[20] R Shimmin. Using a smartphone camera for nanosatellite attitude determination. *amos*, page E104, 2014.

[21] Hao Wang, Zhi-yuan Wang, Ben-dong Wang, Zhong-he Jin, and John L Crassidis. Infrared earth sensor with a large field of view for low-earth-orbiting micro-satellites. *Frontiers of Information Technology & Electronic Engineering*, pages 1–10, 2020.

[22] James R Wertz. *Spacecraft Attitude Determination and Control*, volume 73. Springer Science & Business Media, 1978.

[23] F Landis Markley and John L Crassidis. *Fundamentals of spacecraft attitude determination and control*, volume 33. Springer, 2014.

[24] Bong Wie. *Space vehicle dynamics and control*. American Institute of Aeronautics and Astronautics, 2008.

[25] Malcolm D Shuster et al. A survey of attitude representations. *Navigation*, 8(9):439–517, 1993.

[26] Yaguang Yang. *Spacecraft Modeling, Attitude Determination, and Control: Quaternion-Based Approach*. CRC Press, 2019.

[27] Aboelmagd Noureldin, Tashfeen B Karamat, and Jacques Georgy. *Fundamentals of inertial navigation, satellite-based positioning and their integration*. Springer Science & Business Media, 2012.

[28] Howard D Curtis. *Orbital mechanics for engineering students*. Butterworth-Heinemann, 2013.

[29] Richard Hartley and Andrew Zisserman. *Multiple view geometry in computer vision*. Cambridge university press, 2003.

[30] Peter Fortescue, Graham Swinerd, and John Stark. *Spacecraft systems engineering*. John Wiley & Sons, 2011.

[31] Wiley J Larson and James Richard Wertz. Space mission analysis and design. Technical report, Torrance, CA (United States); Microcosm, Inc., 1992.

[32] Marcel J Sidi. *Spacecraft dynamics and control: a practical engineering approach*, volume 7. Cambridge university press, 1997.

[33] Halil Ersin Soken and Shin-ichiro Sakai. Attitude estimation and magnetometer calibration using reconfigurable triad+ filtering approach. *Aerospace Science and Technology*, 99:105754, 2020.

[34] P Alken, E Thebault, CD Beggan, H Amit, J Aubert, J Baerenzung, TN Bondar, W Brown, S Califf, A Chambout, et al. International geomagnetic reference field: the thirteenth generation. *Earth, Planets and Space*, 2020.

[35] Halil Ersin Soken. A survey of calibration algorithms for small satellite magnetometers. *Measurement*, 122:417–423, 2018.

[36] Edith A Müller and Arnost Jappel. *Transactions of the International Astronomical Union: Proceedings of the Sixteenth General Assembly Grenoble 1976*, volume 16. Springer Science & Business Media, 2012.

[37] Alan Hirshfeld, Roger W Sinnott, and Frangois Ochsenbein. *Sky Catalogue 2000.0: Volume 1*, volume 1. Cambridge University Press, 1991.

[38] P Salomon and W Goss. A microprocessor-controlled ccd star tracker. In *14th Aerospace Sciences Meeting*, page 116, 1976.

[39] John L Junkins, Chelsea C White, and James D Turner. Star pattern recognition for real time attitude determination. *Journal of the Astronautical Sciences*, 25(3):251–270, 1977.

[40] Benjamin B Spratling and Daniele Mortari. A survey on star identification algorithms. *Algorithms*, 2(1):93–107, 2009.

[41] Ring laser gyroscopes. `https://www.britannica.com/technology/ring-laser-gyroscope`, 2020. [Online; accessed 20.12.2020].

[42] Meixiang Quan, Songhao Piao, Minglang Tan, and Shi-Sheng Huang. Tightly-coupled monocular visual-odometric slam using wheels and a mems gyroscope. *IEEE Access*, 7:97374–97389, 2019.

[43] L Markley. Attitude determination using two vector measurements. In *NASA Conference Publication*, pages 39–52. NASA, 1999.

[44] Harold D Black. A passive system for determining the attitude of a satellite. *AIAA journal*, 2(7):1350–1351, 1964.

[45] Grace Wahba. A least squares estimate of satellite attitude. *SIAM review*, 7(3):409–409, 1965.

[46] F Landis Markley and Daniele Mortari. How to estimate attitude from vector observations. 1999.

[47] Paul B Davenport. *A vector approach to the algebra of rotations with applications*, volume 4696. National Aeronautics and Space Administration, 1968.

[48] Malcolm David Shuster and S D_ Oh. Three-axis attitude determination from vector observations. *Journal of guidance and Control*, 4(1):70–77, 1981.

[49] M Shuster. Approximate algorithms for fast optimal attitude computation. In *Guidance and Control Conference*, page 1249, 1978.

[50] F Landis Markley. Attitude determination using vector observations and the singular value decomposition. *Journal of the Astronautical Sciences*, 36(3):245–258, 1988.

[51] James Lawrence Farrell. Attitude determination by kalman filtering. *Automatica*, 6(3):419–430, 1970.

[52] EJ Leffens, F Landis Markley, and Malcolm D Shuster. Kalman filtering for spacecraft attitude estimation. *Journal of Guidance, Control, and Dynamics*, 5(5):417–429, 1982.

[53] Mark L Psiaki, Francois Martel, and Parimal K Pal. Three-axis attitude determination via kalman filtering of magnetometer data. *Journal of Guidance, Control, and Dynamics*, 13(3):506–514, 1990.

[54] F Landis Markley. Attitude error representations for kalman filtering. *Journal of guidance, control, and dynamics*, 26(2):311–317, 2003.

[55] F Landis Markley. Attitude estimation or quaternion estimation? *Journal of the Astronautical Sciences*, 52(1-2):221–238, 2004.

[56] John L Crassidis, F Landis Markley, and Yang Cheng. Survey of nonlinear attitude estimation methods. *Journal of guidance, control, and dynamics*, 30(1):12–28, 2007.

[57] Mohinder S Grewal and Angus P Andrews. Applications of kalman filtering in aerospace 1960 to the present [historical perspectives]. *IEEE Control Systems Magazine*, 30(3):69–78, 2010.

[58] Andrew J Auman. *Geometric attitude estimation & orbit modelling*. University of Surrey (United Kingdom), 2015.

[59] Malcolm D Shuster. Kalman filtering of spacecraft attitude and the quest model. *Journal of the Astronautical Sciences*, 38:377–393, 1990.

[60] John L Crassidis and John L Junkins. *Optimal estimation of dynamic systems*. CRC press, 2011.

[61] GT Shrivakshan and Chandramouli Chandrasekar. A comparison of various edge detection techniques used in image processing. *International Journal of Computer Science Issues (IJCSI)*, 9(5):269, 2012.

[62] John Canny. A computational approach to edge detection. *IEEE Transactions on pattern analysis and machine intelligence*, (6):679–698, 1986.

[63] E Roy Davies. *Computer and machine vision: theory, algorithms, practicalities*. Academic Press, 2012.

[64] Nick Kanopoulos, Nagesh Vasanthavada, and Robert L Baker. Design of an image edge detection filter using the sobel operator. *IEEE Journal of solid-state circuits*, 23(2):358–367, 1988.

[65] Andrew Fitzgibbon, Maurizio Pilu, and Robert B Fisher. Direct least square fitting of ellipses. *IEEE Transactions on pattern analysis and machine intelligence*, 21(5):476–480, 1999.

[66] Zygmunt L Szpak, Wojciech Chojnacki, and Anton van den Hengel. Guaranteed ellipse fitting with a confidence region and an uncertainty measure for centre, axes, and orientation. *Journal of Mathematical Imaging and Vision*, 52(2):173–199, 2015.

[67] D Modenini. Attitude determination from ellipsoid observations: A modified orthogonal procrustes problem. *Journal of Guidance, Control, and Dynamics*, 41(10):2324–2326, 2018.